



# Technische Universität München

Fakultät für Elektrotechnik und Informationstechnik

Lehrstuhl für Biologische Bildgebung

*Image Reconstruction in Optoacoustics*

Daniel Carlos Philipp Queirós

Vollständiger Abdruck der von der Fakultät für Elektrotechnik und Informationstechnik der Technischen Universität München zur Erlangung des akademischen Grades eines

Doktors der Naturwissenschaften

genehmigten Dissertation.

Vorsitzender: Univ.-Prof. Dr.-Ing. Eckehard Steinbach

Prüfer der Dissertation:

1. Univ.-Prof. Vasilis Ntziachristos, Ph.D.
2. Univ.-Prof. Dr.rer.nat. Franz Pfeiffer
3. Univ.-Prof. Dr.-Ing. Bernhard U. Seeber

Die Dissertation wurde am 14.08.2014 bei der Technischen Universität München eingereicht und durch die Fakultät für Elektrotechnik und Informationstechnik am 02.06.2015 angenommen.

---

*For my family and friends.*

---

# Abstract

Biomedical research is fundamentally driven by the ability to image biological processes and structures. Thereby, optoacoustic imaging techniques are capable of providing not only structural, but also functional and molecular information enabling researchers to investigate diseases on an unprecedented level. As a hybrid imaging technology, optoacoustics combines the advantages of pure optical techniques and ultrasound. In effect, optoacoustic imaging systems generate reconstructions providing optical contrast and ultrasonic resolution. Thereby, optoacoustic devices are capable of surpassing the limitations of optical techniques and image several centimeters into biological tissue.

Bearing the potential to provide complex information about biological processes, image reconstruction in optoacoustics becomes an important task in order to assure the image accuracy and quantifiability expected. Already the choice of the imaging model has a major impact on the complexity and performance of eventual reconstruction algorithms. Thereby, algebraic inversion algorithms offer superior modeling flexibility over analytic inversion algorithms, resulting in more accurate reconstructions. Including the geometry of ultrasonic transducers into the imaging model is proven to have significant influence on the image quality of optoacoustic reconstructions. This work implements, analyzes and evaluates approaches to incorporate geometric detector properties into model-based reconstruction algorithms. In this process, a theoretical background of optoacoustic signal generation and ultrasonic detection is given. Superior performance of the enhanced model-based algorithm is demonstrated in simulations and experiments with tissue-mimicking Agar phantoms containing micro-particles and biological tissue.

In order to handle the increasing size of a sophisticated imaging model, efficiency strategies based on symmetries in the detection geometry are implemented. Furthermore, this thesis presents a framework for model-based tomographic image reconstruction using wavelet packets. The framework decomposes a large imaging problem into a set of smaller problems, thereby, enabling the application of sophisticated inversion procedures for each of the small problems. In consequence, memory requirements and calculation time for model inversion decreased significantly.

Commonly optoacoustics is implemented in pulsed-mode, where nanosecond laser pulses are applied to generate optoacoustic pressure signals. Alternatively, optoacoustics can be performed employing inexpensive modulated light sources. This thesis presents the tomographic implementation of optoacoustic imaging using a linear frequency modulated laser source. Thereby, the theoretical background is provided, leading to the derivation of a dedicated reconstruction algorithm. The developed imaging system, applying a modulated laser source, showcased for the first time the capability to operate *in-vivo*.



# Acknowledgments

*'If I have seen further than others, it is by standing upon the shoulders of giants.'*

– Isaac Newton

There is a number of people, that contributed with supervision, guidance or the most varied kind of support to the completion of the research covered by this thesis. First and foremost I would like to thank Prof. Vasilis Ntziachristos for giving me the opportunity to work with him in such an exciting field of research during the last three and a half years. It was a good time to work in optoacoustics. I am truly thankful for his supervision, all his unconditional positivity, encouragement and support. It was an honor to experience his expertise in all fields of imaging. Concerning scientific work and motivation he was a shining example to me. Furthermore I would like to thank Prof. Markus Schwaiger for supervising my doctorate and providing unrestricted support and advice. It was an honor to work on a doctorate under such renowned and prestigious advisers.

I would like to express my deepest gratitude to Dr. Xosé Luís Déan-Ben for his support, patience and example throughout my doctorate. It was his persistency both in the laboratory and theoretical work that influenced me as a researcher. He was a main contributor to the project of incorporating geometric detector properties into image reconstruction. The discussions with him were both deepening my understanding and motivating new solutions. I am also greatly indebted to Dr. Amir Rosenthal for his brilliant ideas and pioneering approaches in image reconstruction. Working with him opened new perspectives and insight of reconstruction algorithms. I am a big admirer of his intuition and ability to translate theory to practice.

Furthermore, I am very much obliged to Dr. Stephan Kellnberger, Dr. Nikolaos Deliolanis and Prof. George Sergiadis for their fundamental contributions to the development of the cw-laser tomography system. Their profound insight and understanding lead the focus to the crucial challenges of the project. It was inspiring to participate in an imaging project that included all engineering aspects from basic hardware to theoretical background.

I would also like to thank Dr. Andreas Bühler for his contributions to the project of incorporating geometric detector properties into image reconstruction. His expertise both in code development and experimental work were of major significance. Moreover, I would like

to thank Prof. Daniel Razansky for his comprehensive advice and constructive suggestions.

I sincerely would like to thank Dr. Nicolas Bézière, Dr. Jérôme Gâteau and Dr. Antonio Nunes for all their patience, their support and discussions, in and out of the office. Their expertise and experience deepened my understanding and enabled me to stay focused on the objectives. For his major contributions in code development, fruitful discussions and perspectives I would like to thank Dr. Miguel Caballero.

Furthermore, I would like to thank Alex Dima for setting up the workstations of our institute, which enabled the execution of the complex algorithms developed herein. With Dr. Andreas Oancea, Juan Salichs and Yiyong Han I have had small discussions and collaborations on very specific subjects allowing us to profit of each others knowledge. Especially during the creation of this thesis I have had numerous discussions with my office neighbors Murad Omar and Dr. Stephan Kellnberger. I am truly indebted to them for sharing their knowledge and providing valuable comments.

During my three and a half years at the Institute of Biological and Medical Imaging (IBMI) I have had the opportunity to share my office with numerous people. All of them influenced me in one way or another and enriched me as a person. I would like to emphasize the incredibly loyal and cooperative working atmosphere within the IBMI allowing all scientists to develop their ideas and work productively. It was this spirit that lead our football team to win the Helmholtz center's tournament in 2012.

My deepest gratitude goes to our technical assistants, Sarah Glasl, Uwe Klemm and Florian Jurgeleit who facilitated immensely all experimental work with biological tissue. Moreover, I cannot thank enough our administrative personnel, especially Susanne Stern, Zuzsi Öszi, Dr. Julia Niefnecker and Silvia Weinzierl for their everlasting patience, support and organizing ability. You are the glue that hold the institute together.

I would like to express my gratefulness to the TUM Graduate School of Information Science in Health for their financial support and providing such an incredible framework for a doctorate. Especially to Dr. Ursula Mühle, Katharina Lang and Dr. Petra Dorfner I am indebted for their most varied support, advice and patience. The workshops and seminars at the University of Tokyo, Johns Hopkins University in Baltimore and Harvard University in greater Boston were a unique experience and opportunity.

Finally, I am eternally grateful to my much-loved family who has always supported and encouraged me. Without their unconditional backing during the last three years and before, I would have not been able to accomplish this work. Not less significant was the everlasting backup of my beloved girlfriend Johanna whose always impartial view on life allowed me to put my work into perspective.

# Contents

<b>Abstract</b>	<b>I</b>
<b>Acknowledgments</b>	<b>III</b>
<b>Contents</b>	<b>V</b>
<b>List of Figures</b>	<b>IX</b>
<b>List of Tables</b>	<b>XI</b>
<b>1 Introduction</b>	<b>1</b>
1.1 Biomedical Imaging in History . . . . .	1
1.2 Optoacoustics as a Hybrid Imaging Device . . . . .	3
1.3 Challenges of Image Reconstruction in Optoacoustics . . . . .	4
1.4 Outline of the Thesis . . . . .	5
<b>2 Theoretical Background</b>	<b>7</b>
2.1 Optoacoustic Effect . . . . .	7
2.1.1 Light Propagation . . . . .	7
2.1.2 Heat Conduction and Sound Propagation . . . . .	13
2.2 Modeling the Optoacoustic Effect . . . . .	15
2.2.1 Simplifying Assumptions . . . . .	16
2.2.2 Wave Equation Cauchy Problem . . . . .	17
2.2.3 Green's Function Solution . . . . .	18
2.2.4 Optoacoustics with a cw Laser . . . . .	20
<b>3 Instrumentation</b>	<b>23</b>
3.1 Laser Excitation . . . . .	23
3.1.1 Thermal and Stress Confinement . . . . .	23
3.1.2 Laser Technology and Safety . . . . .	24
3.2 Ultrasonic Detection . . . . .	25
3.2.1 Detection Technology . . . . .	25
3.2.2 Acoustic Focusing . . . . .	26
3.2.3 Transducer Characterization . . . . .	27

3.2.4	Impulse Responses . . . . .	29
3.3	Detection Geometries . . . . .	32
3.3.1	Microscopy . . . . .	33
3.3.2	Endoscopy . . . . .	33
3.3.3	Tomography . . . . .	34
3.4	Optoacoustic Systems . . . . .	37
3.4.1	Single Transducer System . . . . .	37
3.4.2	Transducer Array System . . . . .	38
3.4.3	cw-Laser System . . . . .	39
<b>4</b>	<b>Reconstruction Algorithms</b>	<b>43</b>
4.1	Analytic Inversion Algorithms . . . . .	43
4.1.1	Time Domain Algorithms . . . . .	44
4.1.2	Frequency Domain Algorithms . . . . .	46
4.2	Algebraic Inversion Algorithms . . . . .	51
4.2.1	IMMI Algorithm . . . . .	51
4.3	Signal Recovery and Image Reconstruction in cw-Optoacoustics . . . . .	56
<b>5</b>	<b>Incorporation of Geometric Detector Properties</b>	<b>61</b>
5.1	Discretization by Points . . . . .	61
5.2	Discretization by Lines . . . . .	62
5.3	Simulations in Two Dimensions . . . . .	63
5.3.1	Line Transducer . . . . .	64
5.3.2	Focused Transducer Scanning . . . . .	68
5.4	Simulations in Three Dimensions . . . . .	69
5.4.1	Cylindrically Focused Transducer . . . . .	70
5.5	Experiments in Two Dimensions . . . . .	76
5.6	Experiments in Three Dimensions . . . . .	79
5.6.1	Micro-Particles . . . . .	80
5.6.2	Mouse Spleen . . . . .	81
5.7	Concluding Remarks . . . . .	84
<b>6</b>	<b>Optoacoustic Tomography with a cw-Laser System</b>	<b>85</b>
6.1	Experimental Results with a cw-Laser System . . . . .	85
6.2	Concluding Remarks . . . . .	88
<b>7</b>	<b>Efficiency Techniques for Model-Based Image Reconstruction</b>	<b>91</b>
7.1	Detection Symmetries . . . . .	91
7.1.1	In-Plane Symmetries . . . . .	92
7.1.2	Out-of-Plane Symmetries . . . . .	93
7.2	Wavelet Packets . . . . .	94
7.2.1	Theoretical Rationale . . . . .	96
7.2.2	Results with Simulated and Experimental Data . . . . .	100

7.2.3	Wavelet Packets in Three Dimensions . . . . .	102
7.2.4	Concluding Remarks . . . . .	108
<b>8</b>	<b>Conclusion and Outlook</b>	<b>109</b>
8.1	Conclusive Summary . . . . .	109
8.2	Outlook and Future Directions . . . . .	111
<b>A</b>	<b>Analytical Pressure Formulas</b>	<b>113</b>
A.1	Analytical Pressure Formulas in 2D . . . . .	113
A.1.1	Parabolic Absorption . . . . .	113
A.1.2	Uniform Absorption . . . . .	117
A.2	Analytical Pressure Formulas in 3D . . . . .	118
A.2.1	Parabolic Absorption . . . . .	118
A.2.2	Uniform Absorption . . . . .	121
	<b>Bibliography</b>	<b>123</b>
	<b>Publication List</b>	<b>133</b>



# List of Figures

3.1	Ultrasound Transducers . . . . .	27
3.2	Near and Far Field of a Flat Transducer . . . . .	28
3.3	Rasterscanning Optoacoustic Microscopy . . . . .	33
3.4	Optoacoustic Endoscopy . . . . .	34
3.5	Line Scan Optoacoustic Tomography . . . . .	35
3.6	Circular Scan Optoacoustic Tomography . . . . .	36
3.7	Optoacoustic Tomography along a Cylindrical Detection Geometry . . . . .	36
3.8	Optoacoustic Tomography along a Spherical Detection Geometry . . . . .	37
3.9	Single Transducer Optoacoustic Imaging System . . . . .	38
3.10	Optoacoustic Transducer Array Imaging System . . . . .	39
3.11	Optoacoustic Imaging System with a cw-Laser . . . . .	41
4.1	Two-Dimensional Back-Projection . . . . .	45
4.2	Geometry for the Two-Dimensional IMMI Algorithm . . . . .	53
4.3	Bilinear Interpolation . . . . .	54
4.4	LFM Chirp in Time- and Frequency-Domain . . . . .	57
4.5	Rectangular and Triangular Function . . . . .	58
4.6	Cross-Correlation Function . . . . .	59
5.1	Optoacoustic Signals Emitted by a Two-Dimensional Absorption Pattern . . . . .	65
5.2	Tomographic Detection Geometry with a Line Transducer . . . . .	66
5.3	Two-Dimensional Reconstructions of Simulated Data Measured with a Line Detector . . . . .	67
5.4	Two-Dimensional Geometry of a Line Scan with a Focused Transducer . . . . .	68
5.5	Image Reconstructions of a Line Scan with a Focused Transducer . . . . .	69
5.6	Condition Number of the Model Matrix for Different Scan Lengths . . . . .	69
5.7	Approximation of a Cylindrically Focused Transducer by Points and Lines . . . . .	71
5.8	Comparison of Three-Dimensional Model Matrices Incorporating Detector Properties . . . . .	73
5.9	Three-Dimensional Tomographic Detection Geometry . . . . .	74
5.10	Three-Dimensional Reconstructions of Simulated Data Measured with a Cylindrically Focused Transducer . . . . .	75
5.11	Evaluation of Three-Dimensional Reconstructions of Simulated Data . . . . .	76

5.12	Two-Dimensional Detection Geometry . . . . .	77
5.13	Two-Dimensional Image Reconstructions of Four Micro-Spheres . . . . .	78
5.14	Evaluation of Image Reconstruction Algorithms in Two Dimensions . . . . .	79
5.15	Three-Dimensional Reconstructions of Experimental Data Obtained with a Cylindrically Focused Transducer . . . . .	82
5.16	Three-Dimensional Reconstructions of a Mouse Spleen Embedded in Agar . . . . .	83
6.1	Tomographic Reconstruction of Two Agar-Phantoms Measured with the cw- Laser System . . . . .	87
6.2	Tomographic Reconstructions of a Mouse Tail Measured <i>In-Vivo</i> with the cw-Laser System . . . . .	88
7.1	Symmetry Axes of a Quadratic ROI and a 360° Detection Circumference . . . . .	92
7.2	Translational Symmetry of a Three-Dimensional ROI . . . . .	94
7.3	Three-Dimensional ROI and its Corresponding Sub-ROI Within the En- larged ROI . . . . .	95
7.4	Full-Tree Wavelet Packet Decomposition of Depth $Z = 2$ . . . . .	98
7.5	Comparison of Model-Based Reconstructions of Simulated Data with Re- constructions Obtained in the Wavelet Domain . . . . .	101
7.6	Comparison of Model-Based Reconstructions of Experimental Data with Reconstructions Obtained in the Wavelet Domain . . . . .	102
7.7	Detection Geometry for Simulations with the Three-Dimensional Model- Based Reconstruction Algorithm in the Wavelet Domain . . . . .	105
7.8	Energy of the Pressure Signals Generated by 64 Wavelet Packets. . . . .	106
7.9	Comparison of Model-Based Reconstructions in Three Dimensions with Re- constructions Obtained in the Wavelet Domain . . . . .	107
A.1	Two-Dimensional Absorption Patterns and Their Analytical Signals . . . . .	114
A.2	Three-Dimensional Absorption Patterns and Their Analytical Signals . . . . .	119

# List of Tables

2.1	Optical Quantities . . . . .	9
2.2	Thermodynamic Quantities . . . . .	15
5.1	Memory Requirements for Two-Dimensional Model Matrices. . . . .	67



# Chapter 1

## Introduction

*'As to diseases, make a habit of two things – to help, or at least, to do no harm.'*  
– Hippocrates

### 1.1 Biomedical Imaging in History – From Structural over Functional to Molecular Information

For decades, the development of improved imaging technologies proved to be a driving factor of advancements in biological research and medicine. In the very sense of the word, by producing an image of a patient, scientists and physicians gained insight into structure and physiology of living tissue. Grasping a diseased body part with their eyes, enables better understanding of cause, constitution and behavior related to a disease.

For centuries, medical diagnostics was limited to the regions of the body the physicians could see with their proper eyes. In 1806, a medical doctor in Mainz, Philipp Bozzini, extended that range by developing a first stiff medical endoscope. He named his invention 'Lichtleiter' (light conductor) as it uses natural light 'for the examinations of the canals and cavities of the human body' [1]. In effect, physicians could extend their field of vision by inserting the endoscope into human orifices, enabling the examination of some hollow organs or body cavities. However, most interior parts of the body remained invisible to medical diagnostics. This barrier fell with the first major breakthrough in medical imaging. In 1895, the discovery of X-rays and its interaction with human tissue by German physicist Wilhelm Conrad Röntgen [2] paved the way to new insights of the human body. For the first time projection images through the entire body visualized internal structures of the human body. In 1901, Röntgen was awarded with the first Nobel Prize in physics for his discovery. Although X-rays refer to a part of the electromagnetic spectrum which has an ionizing effect on human tissue, they are still among the most widely used imaging techniques today.

The concept of sending energy in form of waves into the body, and measuring its response after interaction with human tissue, was also at the basis of the development of medical

ultrasound. Austrian neurologist Karl Dussik was the first to apply ultrasonic energy for the purpose of imaging the human body. In 1942, he performed a scan of the ventricular system in the brain with a procedure he then called 'Hyperfonographie'. The theory behind ultrasonic measurements had been developed before by Paul Langevin in France. The initial motivation came from military needs during World War I, where the aim was sound location of submarines. In contrast to X-ray imaging, ultrasonography is not based on ionizing radiation and is therefore harmless for the human body. Nowadays, its applications range from real-time three-dimensional imaging in prenatal diagnostics, over Doppler echocardiography to intravascular ultrasound (IVUS) [3].

It took until the early nineteen seventies, for fundamentally new medical imaging devices to come to the market. Both X-ray computed tomography (XCT) and magnetic resonance imaging (MRI) revolutionized medical diagnostics and intervention as for the first time cross-sectional images of the whole human body could be generated. In the early sixties, physicist Allan Cormack developed the theoretical basis of a computer tomograph that in 1971 Sir Godfrey Hounsfield put into practice by building the first XCT scanner [4],[5]. The mathematical fundament behind tomographic reconstructions dates back to 1917, when Austrian mathematician Johann Radon invented the famous transform that would be named after him. He was able to show mathematically that a function could be reconstructed from an infinite set of its projections [6]. Although, generating XCT images exposes the patient to ionizing radiation, the diagnostic quality of the high resolution three-dimensional images makes XCT a valuable device in imaging. In 1979, Cormack and Hounsfield received the Nobel Prize in medicine for their contributions in the development of XCT. However, if a high soft-tissue contrast is requested, MRI seems to be the imaging modality of choice. Similar to XCT, MRI provides the physician the ability to produce whole-body three-dimensional images. In 2003, the American chemist Paul Lauterbur together with British physicist Peter Mansfield were awarded with the Nobel Prize in medicine for their essential contributions to the development of MRI [7],[8]. The major advantage of MRI is the fact that a patient is not exposed to radiation, making MRI a viable imaging technology for people who may be vulnerable to the effects of radiation, such as pregnant women and babies. Furthermore, MRI has a superior soft-tissue contrast over other imaging methods. Today, MRI provides doctors and researchers with images of blood vessels, the heart, joints and tendons. Moreover, it possesses the ability to generate functional images (fMRI) of the brain and to represent its nerve fibers with a technique termed diffusion MRI (dMRI) [9]. Functional imaging summarizes modalities that provide images which enable the measurement of metabolic changes or blood flow in living tissue. Other functional imaging techniques, such as positron emission tomography (PET) and single-photon emission computed tomography (SPECT), rely on nuclear probes injected into the human body and are therefore potentially harmful [10]. Conceptually, after injection, a short-lived nuclear tracer isotope accumulates in cancerous tissue and starts decaying radioactively. By measuring the radioactive radiation products of the decay, even small tumors can be localized with unprecedented accuracy [11]. In combination with a XCT or MRI scanner, functional PET or SPECT images can be complemented with structural information provided by XCT or MRI.

Once externally administered molecules take part in the generation of an image, it is only a small step towards functionalizing them as biomarkers that interact chemically with their environment. Thereby, resulting changes on the molecular level can subsequently be captured with an imaging system. Performing so-called molecular imaging aims at enabling researchers to study, on a molecular level, physiological processes of diseases *in-vivo* and real-time. Thereby, small abnormalities on a molecular level allow a premature diagnosis of diseases, even before external symptoms arise.

Besides MRI, PET and SPECT there is an entire range of optical imaging devices being able to perform molecular imaging. Optical methods generally exploit fluorescence, bioluminescence, absorption or reflectance as their source of contrast [12],[13]. A main advantage of all optical techniques is their high contrast and the utilization of non-invasive light in the visible, ultraviolet, and infrared range. Furthermore, by selecting a variety of wavelengths for light excitation of tissue, optical imaging can potentially generate multispectral information. A drawback of optical techniques is their low penetration depth, as light becomes heavily diffused beyond 1 mm into biological tissue, thus, deteriorating image resolution.

## 1.2 Optoacoustics as a Hybrid Imaging Device

Hybrid imaging techniques aim at combining the strengths of two or more alternative imaging technologies. The contribution of each technology intends to make up for a drawback of the other imaging technique, therefore resulting in a superior overall performance. When Alexander Bell described in 1880 the generation of sound with a light source [14], he could not forebode the potential that this phenomenon had for biological and medical imaging. Today, Bell's discovery, termed the optoacoustic (photoacoustic) effect, enables to transfer the advantages of optical imaging techniques to deep tissue [15]. Thereby, optoacoustic imaging devices combine the advantages of both optical and ultrasonic imaging.

By exciting biological tissue with time-varying light energy, optically absorbing structures act as contrast sources of an optoacoustic image. After initial light excitation, optical absorbers undergo a temperature rise in the millikelvin range which is followed by thermoelastic expansion [16]. Thereby, each optical absorber emits a transient pressure wave which propagates through tissue and can be detected by ultrasonic transducers positioned around the sample [17]. The measured pressure data is subsequently processed by a reconstruction algorithm calculating the initial pressure distribution, which is proportional to the optical absorption pattern [18]. As a consequence, the reconstructed image will exhibit optical contrast and ultrasonic resolution.

In order to generate detectable optoacoustic pressure signals, a sufficient number of photons has to reach an optical absorber. Contrary to pure optical techniques, excitation photons in optoacoustics do not have to be exclusively ballistic in order to generate high resolution images. Once entering scattering media like biological tissue, light photons become diffusive after multiple scattering events. This limits the field of application for purely optical

techniques to several hundreds of micrometers. However, diffusive light, particularly in the near-infrared range, can penetrate up to several centimeters into biological tissue and deposit its energy there. Then, as acoustic attenuation is several orders of magnitude weaker than optical attenuation [19], once a sufficiently strong pressure wave is generated by an optical absorber, optoacoustic imaging allows to spatially reveal all structures emitting ultrasonic signals. Furthermore, by selecting several excitation wavelengths in combination with dedicated unmixing algorithms, multispectral optoacoustic tomography (MSOT) provides biomedical research with an efficient tool to image functional and molecular processes *in-vivo* [20]. The spectrum of applications ranges from imaging of pharmacokinetics [21], *in-vivo* physiology [22], and cardiovascular dynamics [23]. Thereby, optoacoustics extends the advantages of optical techniques from microscopic ranges to macroscopy, enabling small-animal whole-body imaging [24].

Depending on the implementation of the individual imaging systems, optoacoustics offers potentially three-dimensional, multispectral images acquired *in-vivo* and real-time [25]. Furthermore, as optoacoustically generated pressure signals are inherently wide-band, image resolution can be adjusted according to the application by applying ultrasonic transducers with sensitivity in the appropriate frequency band. All these degrees of freedom (DOF), turn optoacoustics into a sophisticated and powerful imaging technique. Yet, image reconstruction becomes a cumbersome task, prone to artifacts and inaccuracies. Meanwhile, molecular imaging applications require imaging devices that robustly generate images meeting a particularly high standard of accuracy and quantifiability.

### 1.3 Challenges of Image Reconstruction in Optoacoustics

Conceptually, once optoacoustically generated pressure signals are recorded, they serve as the input data of a reconstruction algorithm that calculates an image. The reconstruction algorithm intends to reverse the process, termed forward problem, that converts light energy deposited at optical absorbers to ultrasonic pressure waves. In the derivation of a reconstruction algorithm, physical processes involved in the conversion of optical energy to mechanical energy are described by physical models. In doing so, optoacoustic imaging is embedded into a framework of mathematical equations. Once a model characterizing the imaging system is defined, image reconstruction consists of inverting the model, either analytically or numerically. The definition of a model, incorporating the physical processes of the imaging system, is a crucial step within the reconstruction procedure. Generally, more complex models lead to more accurate image reconstructions. However, an overly detailed imaging model induces impracticably long reconstruction times which may turn an algorithm unfeasible.

Most reconstruction algorithms are merely based on the wave equation, modeling the propagation of optoacoustically induced pressure waves [26],[27],[28],[29],[30],[31],[32]. Particularly analytic inversion algorithms in time and frequency domain do not model any

additional physical effects, such as acoustic heterogeneities and attenuation, light propagation or geometric detector properties. Yet, algebraic inversion algorithms offer the possibility to include every linearizable physical effect into a complex imaging model [33],[34],[35],[36],[37].

Specifically, modeling the ultrasonic detection system has been proven to be a challenging step [36],[37],[38],[39]. The vast majority of imaging models assumes ultrasonic transducers to be localized at points in space. However, realistic detectors have a surface or even a focus, in order to assure a sufficient signal to noise ratio (SNR) or to measure signals from selective regions. The discrepancy between imaging model and actually employed detection hardware is the cause of severe artifacts and inaccuracies in the results of reconstruction algorithms.

The aim of this thesis is to investigate the effects of complex imaging models for optoacoustic imaging. A key aspect is the implementation, analysis and evaluation of model-based reconstruction algorithms incorporating geometric detector properties. In the process, the benefits in image accuracy and quantifiability are demonstrated for a three-dimensional tomographic setup capable of small-animal imaging. Moreover, strategies to minimize computational demands and to accelerate image reconstruction are presented. Furthermore, this work showcases the feasibility to reconstruct cross-sectional images from pressure data acquired by an optoacoustic tomography setup based on an inexpensive continuous wave (cw) laser.

## 1.4 Outline of the Thesis

Following the present introductory chapter, this thesis is structured as follows. Chapter 2 provides the reader with the theoretical background of optoacoustics. Thereby, all physical phenomena contributing to the optoacoustic effect, light propagation, heat conduction and sound propagation, are covered. Subsequently, the focus is directed to the transfer of essential contributions involved in the optoacoustic effect into a mathematical model, allowing to calculate analytical solutions. A final section is dedicated to the theory of optoacoustics employing cw laser excitation. In chapter 3 all relevant instrumentation for an optoacoustic imaging system is introduced. Particular emphasis is given to laser technology and ultrasonic detectors. Thereby, characterizing quantities and measures are presented and explained. The chapter closes with an overview over current optoacoustic detection geometries and the presentation of three optoacoustic imaging systems. All experimental results shown throughout this work were acquired with either of the three imaging systems. Chapter 4 summarizes the variety of optoacoustic image reconstruction algorithms, trying to classify them by their theoretic approach. The chapter focuses thereby on algorithms related to this work, as a truly comprehensive review is beyond the scope of this thesis. Then, chapter 5 introduces two imaging models incorporating geometric detector properties in the context of a model-based reconstruction algorithm presented in chapter 4. The superior performance of these models over commonly used reconstruction methods is

showcased in simulations and experiments (including biological samples) performed in two and three dimensions. Thereafter, first reconstructions of experimental data obtained by a tomographic optoacoustic imaging system using a cw laser are shown in chapter 6. The developed imaging system in combination with the dedicated reconstruction algorithm prove their ability to operate with *in-vivo* biological tissue. In chapter 7 techniques to reduce memory requirements for model-based reconstruction algorithms are presented. Furthermore, a framework of model-based reconstruction in the wavelet domain is demonstrated, promising a significant reduction in reconstruction time. The thesis ends with chapter 8 reviewing the results of this thesis in a conclusive summary and providing an outlook over remaining open questions and next steps within the research of optoacoustic image reconstruction.

# Chapter 2

## Theoretical Background

The present chapter provides an introduction to the physical background of optoacoustics. Furthermore, practical considerations arising when modeling the optoacoustic effect are presented, leading to the formulation of optoacoustic image reconstruction within a mathematical framework. Therein, mathematical arguments lead to the derivation of a solution to the equations describing optoacoustic wave propagation.

### 2.1 Optoacoustic Effect

The physical effect at the basis of optoacoustic imaging was first discovered in 1880 by Alexander Graham Bell [14]. It describes how a light pulse is converted into a temperature rise, which in effect emits an ultrasound wave. In this section, the theoretical foundation of the different physical phenomena that constitute the optoacoustic effect are given. Thereby governing equations of each physical process are provided. The theory developed in this chapter is mainly adapted from [16] and [18].

#### 2.1.1 Light Propagation

The initial energy for the optoacoustic effect is deposited via photons emitting from a light source. Upon entering biological tissue, photons are subject to a number of physical interactions such as scattering and absorption. Commonly, photon transport in biological tissue is modeled by the radiative transport equation (RTE). The RTE is a partial differential equation describing the behavior of the radiance  $L$  in tissue, which is a function with six degrees of freedom. As the RTE is difficult to solve, it is often approximated by the diffusion equation, whose solution is computationally less demanding. In the following subsection, first, an overview over relevant physical quantities is given. Then the RTE is derived via the conservation of energy principle. The subsection concludes, by presenting the diffusion approximation, which leads to the deduction of the diffusion equation.

The central physical quantity of the RTE is radiance  $L$  which describes energy flow per

unit normal area per unit solid angle per unit time. Radiance

$$L = L(\vec{r}, \hat{s}, t) \quad (2.1)$$

is a function of spacial position  $\vec{r} = (x, y, z)^T$ , (normalized) direction  $\hat{s} = \hat{s}(\phi, \theta)$  and time  $t$ . Its unit is  $[\frac{\text{W}}{\text{m}^2\text{sr}}]$ .

Based on radiance  $L$ , one can derive the following other physical quantities. Fluence rate  $\Phi$  is defined as the energy flow per unit area per unit time regardless of the flow direction and is measured in units of  $[\frac{\text{W}}{\text{m}^2}]$ . By integrating the radiance over the entire  $4\pi$  solid angle, one obtains the fluence rate

$$\Phi(\vec{r}, t) := \int_{4\pi} L(\vec{r}, \hat{s}, t) d\Omega. \quad (2.2)$$

Using this, one can define the specific power deposition  $A_p$  as the optical energy absorbed by the medium per unit volume per unit time. It can be calculated by multiplying the absorption coefficient  $\mu_a$  with the fluence rate  $\Phi$ ,

$$A_p(\vec{r}, t) := \mu_a \Phi(\vec{r}, t) \quad (2.3)$$

and is measured in  $[\frac{\text{W}}{\text{m}^3}]$ . Furthermore, specific energy deposition  $A_e$  is defined as the time integral over the specific power deposition  $A_p$ ,

$$A_e(\vec{r}) := \int_{-\infty}^{\infty} A_p(\vec{r}, t) dt. \quad (2.4)$$

Current density  $\vec{J}$  is a vector that defines the net energy flow per unit area. It can be obtained by multiplying the radiance  $L$  with the normalized directional vector  $\hat{s}$  and integrating over the entire  $4\pi$  solid angle,

$$\vec{J}(\vec{r}, t) := \int_{4\pi} L(\vec{r}, \hat{s}, t) \hat{s} d\Omega. \quad (2.5)$$

Current density  $\vec{J}$  is measured in  $[\frac{\text{J}}{\text{m}^3}]$ .

In the following, the RTE is derived from the principle of conservation of energy. Thereby, coherence and polarization of the optical radiation as well as any nonlinear effects are neglected. Optical quantities listed in table 2.1 are assumed to be time-invariant, yet space-variant.

In order to define the contributing sources, consider a stationary differential cylinder element of differential length  $ds$ . Its differential cross-section  $dA$  is perpendicular to the photon propagation direction vector  $\hat{s}$ .  $d\Omega$  denotes the differential solid angle element. Below, contributions to energy change of this differential volume element within  $d\Omega$  along  $\hat{s}$  are considered.

Symbol	Optical Property	Unit
$n$	Refractive Index	–
$\mu_a$	Absorption Coefficient	$[\frac{1}{\text{m}}]$
$\mu_s$	Scattering Coefficient	$[\frac{1}{\text{m}}]$
$\mu_t = \mu_a + \mu_s$	Extinction Coefficient	$[\frac{1}{\text{m}}]$
$g$	Scattering Anisotropy	–
$\mu'_s = \mu_s(1 - g)$	Transport/Reduced Scattering Coefficient	$[\frac{1}{\text{m}}]$
$\mu'_t = \mu_a + \mu'_s$	Transport/Reduced Extinction Coefficient	$[\frac{1}{\text{m}}]$
$l_t = \frac{1}{\mu'_t}$	Transport Mean Free Path	[m]

Table 2.1: Optical properties and their units.

## 1. Divergence

As no photon beam is (locally) perfectly collimated, there will be photons diverging out of the differential volume or solid angle element, hence, reducing the differential energy within the cylinder element. The (differential) energy per unit time due to divergence can be calculated by

$$dP_{div} = \frac{\partial L(\vec{r}, \hat{s}, t)}{\partial \hat{s}} dV d\Omega = \hat{s} \cdot \nabla L(\vec{r}, \hat{s}, t) = \nabla \cdot [L(\vec{r}, \hat{s}, t) \hat{s}] \quad (2.6)$$

where  $dV = dsdA$ . This contribution is negative for beam divergence, yet can be positive for beam convergence.

## 2. Extinction

The energy of each photon can be extinct due to absorption or scattering. Therefore, the energy loss in the volume element within the solid angle element per unit time due to extinction is given by

$$dP_{ext} = (\mu_t ds) [L(\vec{r}, \hat{s}, t) dAd\Omega]. \quad (2.7)$$

Here,  $\mu_t = \mu_a + \mu_s$  defines the total extinction coefficient, photon energy loss by either absorption or scattering.  $(\mu_t ds)$  is the probability of a photon being extinct within  $ds$ .

## 3. Scattering

A photon from an arbitrary direction  $\hat{s}'$  can be scattered into  $d\Omega$  around direction  $\hat{s}$

and therefore contribute to the energy per unit time within the differential volume element. This can be expressed by

$$dP_{sca} = (N_s dV) \left[ \int_{4\pi} L(\vec{r}, \hat{s}, t) P(\hat{s}', \hat{s}) \sigma_s d\Omega' \right] d\Omega. \quad (2.8)$$

Here  $\sigma_s$  is the scattering cross section of a scatterer and  $N_s$  is the number density of the scatterers. Their product defines the scattering coefficient  $\mu_s := N_s \sigma_s$ . The first part of the equation 2.8,  $N_s dV$ , represents the number of scatterers in the differential volume element. The second part,  $L(\vec{r}, \hat{s}, t) \sigma_s$ , denotes the energy collected by a single scatterer within the solid angle  $d\Omega'$ , multiplied by the probability of light propagating in direction  $\hat{s}'$  being scattered into  $d\Omega$  around direction  $\hat{s}$ . Thereby,  $P(\hat{s}', \hat{s})$  represents a probability density function which generally only depends on the angle between the two directions  $\hat{s}$  and  $\hat{s}'$ , yielding

$$\int_{4\pi} P(\hat{s}, \hat{s}') d\Omega = \int_{4\pi} P(\hat{s} \cdot \hat{s}') d\Omega = 1. \quad (2.9)$$

#### 4. Source

Light energy can be generated by an internal source in the volume element. Its energy within the solid angle element per unit time is given by

$$dP_{src} = \mathbf{S}(\vec{r}, \hat{s}, t) dV d\Omega. \quad (2.10)$$

Now, all the above contributions can be combined into the conservation of energy principle. Expressing the change in energy in the volume element within the solid angle element per unit time, one obtains

$$dP = \frac{1}{c} \frac{\partial L(\vec{r}, \hat{s}, t)}{\partial t} dV d\Omega, \quad (2.11)$$

with  $c$  denoting the speed of light in the respective medium. Then, the sum of all contributions to the energy change in the volume element per unit time is equalized with expression 2.11. Thereby, according to the respective contribution, a '+' or '-' sign precedes each term

$$dP = -dP_{div} - dP_{ext} + dP_{sca} + dP_{src}. \quad (2.12)$$

By substituting 2.6, 2.7, 2.8, 2.10 and 2.11 into 2.12 one obtains

$$\frac{1}{c} \frac{\partial L(\vec{r}, \hat{s}, t)}{\partial t} = -\hat{s} \cdot \nabla L(\vec{r}, \hat{s}, t) - \mu_t L(\vec{r}, \hat{s}, t) + \mu_s \int_{4\pi} L(\vec{r}, \hat{s}, t) P(\hat{s}' \cdot \hat{s}) d\Omega' + \mathbf{S}(\vec{r}, \hat{s}, t), \quad (2.13)$$

which is known as the RTE.

The RTE is a partial differential equation (PDE) modeling photon transport in biological tissue. As introduced in equation 2.1, the sought function, radiance  $L$ , is a function with six DOF,

$$L(\vec{r}, \hat{s}, t) = L(x, y, z, \phi, \theta, t). \quad (2.14)$$

Therefore, the RTE is complicated to solve and is usually approximated by the simpler Diffusion Equation. The Diffusion Equation is a partial differential equation modeling the behavior of the fluence rate  $\Phi(\vec{r}, t)$ , which is a function of only four DOF. In order to approximate the RTE it is assumed that photons travel through a high-albedo ( $\mu_s \gg \mu_a$ ) medium where  $L$  is approximately isotropic after sufficient scattering events (diffusion approximation).

Radiance  $L$  can be expanded into a series of spherical harmonics  $Y_{n,m}$  as a set of orthonormal basis functions [40],

$$L(\vec{r}, \hat{s}, t) = \sum_{n=0}^N \sum_{m=-n}^n L_{n,m}(\vec{r}, t) Y_{n,m}(\hat{s}). \quad (2.15)$$

Here,  $L_{n,m}$  are the expansion coefficients and the spherical harmonics  $Y_{n,m}$  are defined as

$$Y_{n,m}(\hat{s}) = Y_{n,m}(\phi, \theta) = (-1)^m \sqrt{\frac{(2n+1)(n-m)!}{4\pi(n+m)!}} P_{n,m}(\cos(\theta)) \exp(im\phi) \quad (2.16)$$

with associated Legendre polynomials

$$P_{n,m}(x) = \frac{(1-x^2)^{\frac{m}{2}}}{2^n n!} \frac{d^{m+n}}{dx^{m+n}} (x^2-1)^n. \quad (2.17)$$

The diffusion approximation of the RTE now consists of considering the expansion 2.15 of  $L$  only until first order,  $0 \leq n \leq 1$  (diffusion expansion). Therefore, the series only consists of four expansion functions

- $Y_{0,0}(\phi, \theta) = \frac{1}{\sqrt{4\pi}}$
- $Y_{1,-1}(\phi, \theta) = \sqrt{\frac{3}{8\pi}} \sin \theta e^{-i\phi}$
- $Y_{1,0}(\phi, \theta) = \sqrt{\frac{3}{4\pi}} \cos \theta$
- $Y_{1,1}(\phi, \theta) = -\sqrt{\frac{3}{8\pi}} \sin \theta e^{i\phi}$ .

Inserting equation 2.15 until the first order into equation 2.2 one obtains

$$\Phi(\vec{r}, t) = 4\pi L_{0,0}(\vec{r}, t) Y_{0,0}(\hat{s}). \quad (2.18)$$

Furthermore, multiplying equation 2.15 until  $N = 1$  with  $\hat{s}$  and inserting it into equation 2.5 yields

$$\vec{J}(\vec{r}, t) \cdot \hat{s} = \frac{4\pi}{3} \sum_{m=-1}^1 L_{1,m}(\vec{r}, t) Y_{1,m}(\hat{s}). \quad (2.19)$$

Combining 2.18 and 2.19 gives an expression of radiance  $L$  in terms of fluence rate  $\Phi$  and current density  $\vec{J}$ ,

$$L(\vec{r}, \hat{s}, t) = \frac{1}{4\pi}\Phi(\vec{r}, t) + \frac{3}{4\pi}\vec{J}(\vec{r}, t) \cdot \hat{s}. \quad (2.20)$$

Based on the RTE given in 2.13 one can derive two partial differential equations. First, by substituting 2.20 into 2.13 and integrating over the full  $4\pi$  solid angle one obtains the scalar PDE

$$\frac{1}{c}\frac{\partial\Phi(\vec{r}, t)}{\partial t} + \mu_a\Phi(\vec{r}, t) + \nabla \cdot \vec{J}(\vec{r}, t) = \int_{4\pi} \mathbf{S}(\vec{r}, \hat{s}, t)d\Omega. \quad (2.21)$$

Second, substituting 2.20 into 2.13, multiplying it by  $\hat{s}$  and integrating over the full  $4\pi$  solid angle one obtains the vector PDE

$$\frac{1}{c}\frac{\partial\vec{J}(\vec{r}, t)}{\partial t} + (\mu_a + \mu'_s)\vec{J}(\vec{r}, t) + \frac{1}{3}\nabla\Phi(\vec{r}, t) = 0. \quad (2.22)$$

In order to derive the Diffusion Equation from 2.21 and 2.22, one has to consider the assumption, that fractional changes in the current density  $\vec{J}$  are small within the transport mean free path  $l'_t$ . In mathematical terms this means that

$$\left(\frac{l'_t}{c}\right) \left( \frac{1}{|\vec{J}(\vec{r}, t)|} \left| \frac{\partial\vec{J}(\vec{r}, t)}{\partial t} \right| \right) \ll 1. \quad (2.23)$$

Therein,  $\frac{l'_t}{c}$  can be interpreted as the transport mean free time. Assumption 2.23 implies that  $\frac{1}{c}\frac{\partial\vec{J}(\vec{r}, t)}{\partial t} \approx 0$  thus 2.22 reduces to

$$\vec{J}(\vec{r}, t) = \frac{-1}{3(\mu_a + \mu'_s)}\nabla\Phi(\vec{r}, t), \quad (2.24)$$

which is termed Fick's law with diffusion coefficient

$$D = \frac{1}{3(\mu_a + \mu'_s)}. \quad (2.25)$$

Substituting 2.24 into 2.21 finally yields the diffusion equation

$$\frac{1}{c}\frac{\partial\Phi(\vec{r}, t)}{\partial t} + \mu_a\Phi(\vec{r}, t) - \nabla \cdot [D\nabla\Phi(\vec{r}, t)] = \int_{4\pi} \mathbf{S}(\vec{r}, \hat{s}, t)d\Omega. \quad (2.26)$$

The diffusion equation has been derived from the RTE by considering two simplifying assumptions:

1. Radiance  $L(\vec{r}, \hat{s}, t)$  is only expanded until the first order spherical harmonics.
2. Fractional changes of current density  $\vec{J}(\vec{r}, t)$  within transport mean free path  $l'_t$  are  $\ll 1$ .

Both of the above assumptions can be summarized in the requirement that the reduced scattering coefficient  $\mu'_s$  is the dominant part in photon extinction, namely  $\mu'_s \gg \mu_a$ .

In optoacoustics, it is often assumed that the source  $\mathbf{S}$  is approximately isotropic within the region of interest, meaning that it has almost no directionality,

$$\mathbf{S}(\vec{r}, \hat{s}, t) = \frac{1}{4\pi} \mathbf{S}(\vec{r}, t). \quad (2.27)$$

Furthermore, considering a space-invariant diffusion coefficient  $D$ , equation 2.26 reduces to

$$\frac{1}{c} \frac{\partial \Phi(\vec{r}, t)}{\partial t} + \mu_a \Phi(\vec{r}, t) - D \nabla^2 \Phi(\vec{r}, t) = \mathbf{S}(\vec{r}, t), \quad (2.28)$$

which for  $\mu_a = 0$  becomes the well-known heat diffusion equation

$$\frac{1}{c} \frac{\partial \Phi(\vec{r}, t)}{\partial t} - D \nabla^2 \Phi(\vec{r}, t) = \mathbf{S}(\vec{r}, t). \quad (2.29)$$

In many cases, optoacoustic signals are generated by a focused short-time laser pulse. These pulses are commonly modeled by a Dirac-delta source function,  $\mathbf{S}(\vec{r}, t) = \delta(\vec{r} - \vec{r}') \delta(t - t')$ , at time  $t'$  and spacial position  $\vec{r}'$ . For this source function, there exists a solution to diffusion equation 2.28. The solution reads as

$$\Phi(\vec{r}, t; \vec{r}', t') = \frac{c}{[4\pi D c(t - t')]^{\frac{3}{2}}} \exp \left[ -\frac{|\vec{r} - \vec{r}'|^2}{4Dc(t - t')} - \mu_a c(t - t') \right] \quad (2.30)$$

and is known as Green's function. The argument in the exponential function consists of one part describing the broadening of the photon beam due to scattering,  $\exp \left[ -\frac{|\vec{r} - \vec{r}'|^2}{4Dc(t - t')} \right]$ .

The second part models the exponential decay of the fluence rate due to absorption,  $\exp[-\mu_a c(t - t')]$ , known as Beer's law. Solutions to a general source term  $\mathbf{S}(\vec{r}, t)$  can then be calculated by convolving the Green's function with the source term

$$\Phi(\vec{r}, t) = \int_0^t \int_0^\infty \Phi(\vec{r}, t; \vec{r}', t') \mathbf{S}(\vec{r}', t') d\vec{r}' dt'. \quad (2.31)$$

### 2.1.2 Heat Conduction and Sound Propagation

In the previous subsection the diffusion equation, describing photon transport in a biological tissue has been derived. Its solution, the fluence rate  $\Phi(\vec{r}, t)$ , multiplied by the absorption coefficient  $\mu_a$  and the heat conversion efficiency  $\eta_{th}$  acts as the optoacoustic source term (also denoted as heating function)

$$H(\vec{r}, t) = \eta_{th} \mu_a(\vec{r}) \Phi(\vec{r}, t). \quad (2.32)$$

In order to model the physical processes following tissue excitation by a light source, one can consider the conservation laws of fluid dynamics [41]. The linearized mass, momentum

and energy conservation laws are

$$\frac{\partial \rho(\vec{r}, t)}{\partial t} = -\rho_0(\vec{r}) \nabla \cdot \vec{v}(\vec{r}, t), \quad (2.33)$$

$$\rho_0(\vec{r}) \frac{\partial \vec{v}(\vec{r}, t)}{\partial t} = -\nabla p(\vec{r}, t), \quad (2.34)$$

$$\rho_0(\vec{r}) T_0(\vec{r}) \frac{\partial E(\vec{r}, t)}{\partial t} = \nabla \cdot [\kappa \nabla T(\vec{r}, t)] + H(\vec{r}, t). \quad (2.35)$$

Thereby  $\rho$ ,  $p$ , and  $T$  stand for changes in density, pressure and temperature, respectively.  $\vec{v}$  denotes the particle velocity vector,  $E$  the entropy and  $\kappa$  the thermal conductivity. The subscript 0 defines an ambient quantity. The deposited energy  $H$  causes a rise in temperature  $T$  which simultaneously causes a local change in density  $\rho$  and pressure  $p$ . This process obeys the thermodynamic equation

$$\rho(\vec{r}, t) = \gamma K_T \rho_0(\vec{r}) p(\vec{r}, t) - \rho_0(\vec{r}) \beta T(\vec{r}, t), \quad (2.36)$$

where  $\gamma$  denotes the heat capacity ratio,  $K_T$  the isothermal compressibility and  $\beta$  the volumetric pressure expansion coefficient. Consequently, equations 2.33 and 2.34 can be simplified, by eliminating particle velocity  $\vec{v}$ . To that end, 2.33 is multiplied by  $\frac{\partial}{\partial t}$  and 2.34 by  $-\nabla$ , resulting in

$$\frac{\partial^2 \rho(\vec{r}, t)}{\partial t^2} \frac{1}{\rho_0(\vec{r})} = -\frac{\partial}{\partial t} \nabla \vec{v}(\vec{r}, t), \quad (2.37)$$

$$-\frac{\partial}{\partial t} \nabla \vec{v}(\vec{r}, t) = \nabla \cdot \left( \frac{\nabla p(\vec{r}, t)}{\rho_0(\vec{r})} \right). \quad (2.38)$$

Adding equations 2.37 and 2.38 and inserting relation 2.36 yields, instead of the coupled equations 2.33 and 2.34, a single PDE

$$\frac{\partial^2}{\partial t^2} [\gamma K_T p(\vec{r}, t) - \beta T(\vec{r}, t)] = \nabla \cdot \left( \frac{\nabla p(\vec{r}, t)}{\rho_0(\vec{r})} \right). \quad (2.39)$$

By furthermore inserting the thermodynamic relation

$$\rho_0(\vec{r}) T_0(\vec{r}) E(\vec{r}, t) = \rho_0(\vec{r}) c_p T(\vec{r}, t) - \gamma \beta T_0(\vec{r}) p(\vec{r}, t) \quad (2.40)$$

into equation 2.35 one obtains a coupled system of two partial differential equations without entropy  $E$ ,

$$\frac{\partial^2}{\partial t^2} [\gamma K_T p(\vec{r}, t) - \beta T(\vec{r}, t)] = \nabla \cdot \left( \frac{\nabla p(\vec{r}, t)}{\rho_0(\vec{r})} \right), \quad (2.41)$$

$$\frac{\partial}{\partial t} [\rho_0(\vec{r}) c_p T(\vec{r}, t) - \gamma \beta T_0(\vec{r}) p(\vec{r}, t)] = \nabla \cdot [\kappa \nabla T(\vec{r}, t)] + H(\vec{r}, t). \quad (2.42)$$

A summary including units of all parameters can be found in table 2.2.

Symbol	Thermodynamic Property	Unit
$\rho_0$	Ambient Density	$\left[\frac{\text{kg}}{\text{m}^3}\right]$
$T_0$	Ambient Temperature	[K]
$\kappa$	Thermal Conductivity	$\left[\frac{\text{W}}{\text{Km}}\right]$
$K_T$	Isothermal Compressibility	$\left[\frac{1}{\text{Pa}}\right]$
$\beta$	Thermal Volumetric Expansion Coefficient	$\left[\frac{1}{\text{K}}\right]$
$c_p$	Specific Heat Capacity at Constant Pressure	$\left[\frac{\text{J}}{\text{Kkg}}\right]$
$c_V$	Specific Heat Capacity at Constant Volume	$\left[\frac{\text{J}}{\text{Kkg}}\right]$
$\gamma := \frac{c_p}{c_V}$	Specific Heat Ratio	–
$\eta_{th}$	Heat Conversion Efficiency	–
$\alpha_{th}$	Thermal Diffusivity	$\left[\frac{\text{m}^2}{\text{s}}\right]$
$\Gamma$	Grüneisen Parameter	–

Table 2.2: Thermodynamic properties and their units.

The system of partial differential equations 2.41 and 2.42 has to be solved together in cases where heat conduction cannot be neglected. In a lot of imaging scenarios, exploiting the optoacoustic effect, a series of further simplifying assumptions can be applied. Thereby, the complexity of the governing equations of all three physical phenomena, light propagation, heat conduction and wave propagation, can be reduced. From an image reconstruction standpoint, less complicated model equations lead to less complex and less computationally demanding reconstruction algorithms. Thereby, a trade-off between modeling accuracy on the one hand, and reconstruction speed and image quality on the other hand, has to be made.

## 2.2 Modeling the Optoacoustic Effect

In the previous section all three physical phenomena constituting the optoacoustic effect have been introduced. The most general systems of partial differential equations describing

photon transport, heat conduction and wave propagation have been derived. This section aims at applying the previously developed theories on the practical setting of generating an optoacoustic signal suitable for image reconstruction. Thereby, practical considerations of the hardware used in experiments as well as simplifying assumptions are introduced. The resulting model will be the starting point of reconstruction algorithms presented in this work.

### 2.2.1 Simplifying Assumptions

Generation of optoacoustic signals starts with the delivery of light energy to tissue. In order to describe this process, the following two timescales are introduced.

- The thermal relaxation time,  $\tau_{th}$ , defines the time needed for thermal diffusion of a heated absorber to affect neighboring absorbers. It is estimated by

$$\tau_{th} = \frac{d_c^2}{\alpha_{th}}. \quad (2.43)$$

- The stress relaxation time,  $\tau_{st}$ , characterizes the time needed for pressure to propagate throughout the excited structures. It is defined as

$$\tau_{st} = \frac{d_c}{c_s}. \quad (2.44)$$

Therein,  $\alpha_{th}$  denotes the thermal diffusivity,  $c_s$  the speed of sound and  $d_c$  the characteristic dimension of the excited structures inside the region of interest (ROI). Throughout this thesis, ROI denotes the area containing all to be imaged optoacoustic targets.

In the most general setting, the coupled system of partial differential equations 2.41 and 2.42 has to be solved together. However, if thermal conduction can be neglected, the two equations can be decoupled and simplified into one single PDE. To that end, the thermal conductivity in 2.42 is set to zero,  $\kappa = 0$ . Then, by taking the temporal derivative, 2.42 can be converted to

$$\frac{\partial^2}{\partial t^2} T(\vec{r}, t) = \gamma \frac{\beta T_0(\vec{r})}{\rho_0(\vec{r}) c_p} \frac{\partial^2}{\partial t^2} p(\vec{r}, t) + \frac{1}{\rho_0(\vec{r}) c_p} \frac{\partial}{\partial t} H(\vec{r}, t). \quad (2.45)$$

Inserting this expression into 2.41 yields

$$\left( \gamma \rho_0(\vec{r}) K_T - \gamma \beta \rho_0(\vec{r}) \frac{\beta T_0(\vec{r})}{\rho_0(\vec{r}) c_p} \right) \frac{\partial^2}{\partial t^2} p(\vec{r}, t) - \rho_0(\vec{r}) \nabla \cdot \left( \frac{\nabla p(\vec{r}, t)}{\rho_0(\vec{r})} \right) = \frac{\beta}{c_p} \frac{\partial}{\partial t} H(\vec{r}, t). \quad (2.46)$$

By using the two relations

$$\frac{1}{c_s^2} = \rho_0(\vec{r}) K_T, \quad (2.47)$$

$$c_p - c_v = \frac{\beta^2 T_0(\vec{r})}{\rho_0(\vec{r}) K_T}, \quad (2.48)$$

equation 2.46 can be reduced to

$$\frac{1}{c_s^2} \frac{\partial^2}{\partial t^2} p(\vec{r}, t) - \rho_0(\vec{r}) \nabla \cdot \left( \frac{\nabla p(\vec{r}, t)}{\rho_0(\vec{r})} \right) = \frac{\beta}{c_p} \frac{\partial}{\partial t} H(\vec{r}, t), \quad (2.49)$$

which is the optoacoustic wave equation for heterogeneous media. If the laser pulse length is much shorter than the thermal relaxation time,  $\tau_p \ll \tau_{th}$ , excitation is said to be in thermal confinement and heat conduction can be neglected. As energy in pulsed-mode optoacoustics is delivered by a laser pulse whose duration  $\tau_p$  is typically in the order of less than 10 ns, disregarding heat conduction is justified. Equation 2.49 can be further simplified by assuming a spatially uniform media and therefore setting  $\rho_0(\vec{r}) = \rho_0$ ,

$$\frac{\partial^2}{\partial t^2} p(\vec{r}, t) - c_s^2 \nabla^2 p(\vec{r}, t) = \Gamma \frac{\partial}{\partial t} H(\vec{r}, t). \quad (2.50)$$

Here,  $\Gamma = \frac{c_s^2 \beta}{c_p}$  is a dimensionless constant called the Grüneisen parameter.

### 2.2.2 Wave Equation Cauchy Problem

In order to simplify the description of the heating function 2.32 one assumes that the fluence rate  $\Phi$  is constant in space. This can be interpreted as the number of photons throughout the excited tissue being the same at all spatial positions. Thereby the fluence rate  $\Phi(\vec{r}, t)$  can be separated into a spacial part and a temporal part,

$$\Phi(\vec{r}, t) = \Phi_r(\vec{r}) \Phi_t(t). \quad (2.51)$$

Accordingly, the spatial part is assumed to be constant,  $\Phi_r(\vec{r}) = \Phi_r$ . Assuming that the length of the laser pulses is much shorter than the stress relaxation time,  $\tau_p \ll \tau_{st}$ , one can approximate the temporal part  $\Phi_t(t)$  by a delta impulse function,  $\Phi_t(t) = \delta(t)$ . In this case the excitation is called to be in stress confinement, as all electromagnetic energy has been deposited before any pressure wave travels throughout the ROI. Overall, the function considered as the source of the optoacoustic effect can be written as

$$H(\vec{r}, t) = H_r(\vec{r}) H_t(t) = \eta_{th} \Phi_r \mu_a(\vec{r}) \delta(t). \quad (2.52)$$

Thereby,  $H_r(\vec{r}) = \eta_{th} \Phi_r \mu_a(\vec{r})$  can be considered the spatial part and  $H_t(t) = \delta(t)$  is the temporal part. In summary, the entire optoacoustic effect can be modeled by PDE 2.50 where the source function serves as an initial condition,

$$\frac{\partial^2}{\partial t^2} p(\vec{r}, t) - c_s^2 \nabla^2 p(\vec{r}, t) = 0 \quad (2.53)$$

$$p(\vec{r}, 0) = \Gamma H_r(\vec{r}), \quad (2.54)$$

$$\frac{\partial}{\partial t} p(\vec{r}, 0) = 0. \quad (2.55)$$

This is the optoacoustic wave equation Cauchy problem, which will serve as a starting point for the reconstruction algorithms presented herein. The above formulation of the wave equation is well studied and guarantees existence and uniqueness of a solution [42]. In optoacoustic image reconstruction one aims at recovering the initial condition  $\Gamma H_r(\vec{r})$  by measuring the pressure  $p(\vec{r}, t)$  at several points outside the ROI. Thereby the spatial component of the source function  $H_r(\vec{r}) = \eta_{th} \Phi_r \mu_a(\vec{r})$  defines an energy absorption map, which is the image one finally tries to reconstruct.

### 2.2.3 Green's Function Solution

In the following subsection a Green's function to the wave equation Cauchy problem is presented. The derivation is mainly based on the concepts of [42] and [43]. By finding a Green's function, the solution to the inhomogeneous wave equation with any source term can be calculated by convolution. The problem considered for finding a Green's function is the inhomogeneous wave equation with an impulsive source term at the origin,

$$\frac{\partial^2}{\partial t^2} g(\vec{r}, t) - c_s^2 \nabla^2 g(\vec{r}, t) = \mathbf{S} \delta(\vec{r}) \delta(t) \quad (2.56)$$

$$g(\vec{r}, 0) = 0, \quad (2.57)$$

$$\frac{\partial}{\partial t} g(\vec{r}, 0) = 0, \quad (2.58)$$

where  $\mathbf{S}$  is a scalar defining the magnitude of the source term. In a first step, the Fourier-transform in all three spatial variables  $\vec{r} = (x, y, z)^T$  is defined,

$$\tilde{G}_x(\xi, y, z; t) = \int_{-\infty}^{+\infty} g(x, y, z; t) \exp(-i\xi x) dx, \quad (2.59)$$

$$\tilde{G}_y(x, \eta, z; t) = \int_{-\infty}^{+\infty} g(x, y, z; t) \exp(-i\eta y) dy, \quad (2.60)$$

$$\tilde{G}_z(x, y, \nu; t) = \int_{-\infty}^{+\infty} g(x, y, z; t) \exp(-i\nu z) dz. \quad (2.61)$$

Here, the sub-scripted  $\tilde{G}_x, \tilde{G}_y, \tilde{G}_z$  correspond to the Fourier-transform in the  $x$ -,  $y$ - and  $z$ -dimension, respectively. The respective inverse Fourier transform is defined as

$$g(x, y, z; t) = \frac{1}{2\pi} \int_{-\infty}^{+\infty} \tilde{G}_x(\xi, y, z; t) \exp(i\xi x) d\xi, \quad (2.62)$$

$$g(x, y, z; t) = \frac{1}{2\pi} \int_{-\infty}^{+\infty} \tilde{G}_y(x, \eta, z; t) \exp(i\eta y) d\eta, \quad (2.63)$$

$$g(x, y, z; t) = \frac{1}{2\pi} \int_{-\infty}^{+\infty} \tilde{G}_z(x, y, \nu; t) \exp(i\nu z) d\nu. \quad (2.64)$$

Furthermore, in the temporal dimension, the Laplace-transform is defined as follows

$$G^*(x, y, z; \tau) = \int_0^{+\infty} g(x, y, z; t) \exp(-\tau t) dt. \quad (2.65)$$

Applying the three spatial Fourier-transforms and the temporal Laplace-transform to equation 2.56 one can simplify the PDE into a simple algebraic equation

$$[\tau^2 + c_s^2 (\xi^2 + \eta^2 + \nu^2)] \tilde{G}_{xyz}^*(\xi, \eta, \nu; \tau) = \mathbf{S}. \quad (2.66)$$

Here,  $\tilde{G}_{xyz}^*$  denotes the unknown function, obtained from the Fourier-transform of function  $g(x, y, z; t)$  with respect to all spatial dimensions and taking the Laplace-transform in the temporal dimension. This expression can be written as

$$\tilde{G}_{xyz}^*(\xi, \eta, \nu; \tau) = \frac{\mathbf{S}}{\tau^2 + c_s^2 (\xi^2 + \eta^2 + \nu^2)} \quad (2.67)$$

and be back-transformed with the help of the previously defined inversion formulas and integration formulas taken from [44]. Thereby, one obtains the Green's function  $g$  for the three-dimensional wave equation,

$$g(x, y, z; t) = g(\vec{r}, t) = \frac{\mathbf{S}}{4\pi|\vec{r}|} \delta\left(t - \frac{|\vec{r}|}{c_s}\right), \quad (2.68)$$

where  $|\vec{r}|$  is the euclidean distance to the source,

$$|\vec{r}| = \sqrt{x^2 + y^2 + z^2}. \quad (2.69)$$

The solution to a general source function can now be calculated by convolving the Green's function with the source term (for  $\mathbf{S} = 1$ ), [42]. Considering the optoacoustic source term  $H(\vec{r}, t)$  in equation 2.50, one obtains

$$p(\vec{r}, t) = \Gamma \frac{\partial}{\partial t} H(\vec{r}, t) * g(\vec{r}, t) \quad (2.70)$$

$$= \frac{\Gamma}{4\pi} \int_0^t \iiint_{\mathbb{R}^3} \frac{\partial}{\partial t'} H(\vec{r}', t') \frac{\delta(t - t' - \frac{|\vec{r} - \vec{r}'|}{c_s})}{|\vec{r} - \vec{r}'|} d\vec{r}' dt'. \quad (2.71)$$

This is the solution for the optoacoustic pressure wave excited by a general source function. Now, inserting the delta-pulse excitation term 2.52 into 2.70, one gets

$$p(\vec{r}, t) = \frac{\Gamma}{4\pi} \frac{\partial}{\partial t} \iiint_{|\vec{r} - \vec{r}'| = c_s t} \frac{H_r(\vec{r}')}{|\vec{r} - \vec{r}'|} d\vec{r}', \quad (2.72)$$

where  $H_r(\vec{r}') = \eta_{th} \Phi_r \mu_a(\vec{r}')$ . The integral in equation 2.72 is now a surface integral over the sphere with radius  $c_s t$  centered at position  $\vec{r}$  in space.

### 2.2.4 Optoacoustics with a cw Laser

Commonly, optoacoustic signal generation is performed in a pulsed-mode setting, where light energy is delivered within a time period approximating a delta-like pulse. Beyond that, however, imaging systems generating optoacoustic signals with a continuous wave excitation laser have been suggested in [45], [46], [47]. Thereby, light energy is not delivered by a Dirac-delta like laser pulse. Instead, an amplitude-modulated (chirped) waveform is applied to excite the ROI. Specifically, throughout this thesis, the cw-laser is controlled by a function generator inducing linear frequency-modulated (LFM) chirps resulting in a laser output of

$$l(t) = \mathcal{A} \operatorname{rect} \left( \frac{t}{\mathcal{T}} \right) \cos (\omega_0 t + \pi k t^2). \quad (2.73)$$

Here,  $\mathcal{A}$  denotes the peak laser intensity and  $k$  the sweep rate. The initial angular frequency  $\omega_0$  of the chirp is connected to the initial frequency  $f_0$  as

$$\omega_0 = 2\pi f_0. \quad (2.74)$$

Since the rect function is specified as

$$\operatorname{rect}(x) = \begin{cases} 1, & |x| \leq \frac{1}{2}, \\ 0, & |x| > \frac{1}{2}, \end{cases} \quad (2.75)$$

$\mathcal{T}$  defines the duration of the chirp in 2.73. The sweep rate  $k$  is connected to the bandwidth  $\mathcal{B}$  of covered frequencies as

$$k = \pm \frac{\mathcal{B}}{\mathcal{T}}. \quad (2.76)$$

The linearity of the frequency change can be seen by considering the argument in equation 2.73 which is termed instantaneous phase,

$$\Phi(t) = \omega_0 t + \pi k t^2. \quad (2.77)$$

Then, by using 2.74, the instantaneous frequency results in a linear expression,

$$f(t) = \frac{1}{2\pi} \frac{d\Phi(t)}{dt} = f_0 + kt, \quad (2.78)$$

for  $-\frac{\mathcal{T}}{2} \leq t \leq \frac{\mathcal{T}}{2}$ . As the laser excitation term is an oscillating function in time, it is convenient to consider the modeling wave equation (see 2.50)

$$\frac{\partial^2}{\partial t^2} p(\vec{r}, t) - c_s^2 \nabla^2 p(\vec{r}, t) = \Gamma \frac{\partial}{\partial t} H(\vec{r}, t), \quad (2.79)$$

in the frequency domain. The complex notation of the time-dependent source term is assumed to be  $H(\vec{r}, t) = \tilde{H}(\vec{r}, \omega) \exp(i\omega t)$ . Then, after taking the Fourier-transform of the temporal variable of equation 2.79 one obtains

$$-\omega^2 \tilde{P}(\vec{r}, \omega) - c_s^2 \nabla^2 \tilde{P}(\vec{r}, \omega) = -i\omega \Gamma \tilde{H}(\vec{r}, \omega), \quad (2.80)$$

where  $\tilde{P}(\vec{r}, \omega)$  denotes the temporal Fourier transform of the pressure function  $p(\vec{r}, t)$ . Reformulating the equation 2.80 results in

$$\nabla^2 \tilde{P}(\vec{r}, \omega) + k_\omega^2 \tilde{P}(\vec{r}, \omega) = -\frac{i\omega\beta}{c_p} \tilde{H}(\vec{r}, \omega), \quad (2.81)$$

which is known as the Helmholtz equation with  $k_\omega = \frac{\omega}{c_s}$ . In three dimensions, assuming free space, the Green's function solution to equation 2.81 is given by [48]

$$\tilde{P}(\vec{r}, \omega) = -\frac{i\omega\beta}{c_p} \iiint_{\mathbb{R}^3} \frac{\exp(ik_\omega |\vec{r} - \vec{r}'|)}{4\pi |\vec{r} - \vec{r}'|} \tilde{H}(\vec{r}', \omega) d\vec{r}'. \quad (2.82)$$

Then, the pressure emitted by a point source positioned at  $\vec{r}_s$  is measured by a point transducer as

$$p(\vec{r}, t) = \frac{|\tilde{P}(\vec{r}_s, \omega)|}{4\pi |\vec{r} - \vec{r}_s|} \exp\left(i \left[ \omega \left( t - \frac{|\vec{r} - \vec{r}_s|}{c_s} \right) + \Phi_{th} \right]\right). \quad (2.83)$$

$|\tilde{P}(\vec{r}_s, \omega)|$  denotes the amplitude of the pressure and  $\Phi_{th}$  represents a phase constant due to thermo-elastic expansion [49]. Now, one can consider the complex notation of the chirp defined in 2.73,

$$l(t) = \mathcal{A} \operatorname{rect}\left(\frac{t}{\mathcal{T}}\right) \exp(i\omega(t)t), \quad (2.84)$$

where  $\omega = \omega(t) = \omega_0 + \pi kt$ . With this, equation 2.83 signifies, that the pressure received upon laser excitation with a LFM chirp is also a chirp, delayed by the time  $\frac{|\vec{r} - \vec{r}_s|}{c_s}$  and with a constant phase shift  $\Phi_{th}$

$$p(\vec{r}, t) = \frac{|\tilde{P}(\vec{r}_s, \omega)|}{4\pi |\vec{r} - \vec{r}_s|} \exp\left(i \left[ (\omega_0 + \pi kt) \left( t - \frac{|\vec{r} - \vec{r}_s|}{c_s} \right) + \Phi_{th} \right]\right). \quad (2.85)$$

Again, the above rationale, assumes that the heating function  $H(\vec{r}, t)$  can be divided into a temporal and spatial part

$$H(\vec{r}, t) = H_r(\vec{r})H_t(t) = H_r(\vec{r})l(t). \quad (2.86)$$



# Chapter 3

## Instrumentation

In the following chapter a brief overview over the hardware needed in optoacoustics is given. Both, the optical excitation with lasers, as well as the ultrasonic detection is covered. Furthermore, a summary of current detection geometries is presented and the special requirements of each geometry towards ultrasonic detectors is explained. The chapter concludes with the presentation of three optoacoustic imaging systems.

### 3.1 Laser Excitation

Optoacoustic imaging starts with excitation of tissue by a laser. Thereby, light energy is deposited inside the tissue, triggering a pressure wave due to thermo-elastic expansion. As presented in section 2.2, the optoacoustic effect can be readily modeled by the wave equation Cauchy problem. The mathematical modeling assumes, that the temporal profile of the laser pulse excitation is a delta-function. Actual lasers, however, generate pulses with finite duration. Regardless, the model can still be considered an accurate approximation of the optoacoustic effect if some conditions hold.

#### 3.1.1 Thermal and Stress Confinement

In the derivation that led to the wave equation Cauchy problem 2.53 - 2.55, the excitation was assumed to be in stress (2.44) and thermal confinement (2.43). These two assumptions imply, that the laser pulse duration  $\tau_p$  is short enough, so that stress relaxation and heat conduction are on a longer time scale and can be neglected. In general, the stress relaxation time  $\tau_{st}$  poses a stricter requirement than the thermal relaxation time  $\tau_{th}$ . This can be seen by considering the following numerical example. The characteristic dimension of an absorber is set to be  $d_c = 15 \mu\text{m}$  and the speed of sound in water  $c_s = 1500 \frac{\text{m}}{\text{s}}$ . Thermal diffusivity in human tissue can be approximated by  $\alpha_{th} = 0.13 \cdot 10^{-6} \frac{\text{m}^2}{\text{s}}$  [50]. Then, the thermal relaxation time can be calculated as  $\tau_{th} = 1.73 \text{ ms}$  and the stress relaxation time as  $\tau_{st} = 10 \text{ ns}$ , being five orders of magnitude shorter.

### 3.1.2 Laser Technology and Safety

As shown in the previous subsection, the wave equation Cauchy problem is only a valid model for optoacoustic signal generation, if laser sources deliver pulses with a duration of less than 10 ns. Current laser technology can easily generate laser pulses well below 10 ns with peak powers in the gigawatt range. Thereby, pulsed lasers are commonly operated in the Q-switching mode where an optical attenuator is included within the laser's optical resonator. The Q-switch enables the gain medium to be pumped for a longer time resulting in more energy stored. Once the gain medium is saturated, the Q-switch instantaneously triggers the optical amplification by stimulated emission process. Thereby, the stored energy is promptly released resulting in ultra-short laser-pulses with high peak powers.

In order to generate optoacoustic signals well below the surface of biological tissue, it is crucial that light penetrates as deeply as possible. As light absorption inside tissue is wavelength dependent, typically light in the visible to near-infrared range (650 nm - 950 nm) is used in optoacoustics [51]. Due to the favorable penetration characteristics, the near-infrared part of the electromagnetic spectrum is referred to as 'optical window'. In practice, solid state lasers with a neodymium-doped yttrium aluminium garnet (Nd:YAG) crystal are frequently used. Coupled with a Q-switch, they emit light pulses with a wavelength of 1064 nm. These high peak-power pulses can be frequency doubled to generate laser light of 532 nm, which can be fed to an optical parametric oscillator (OPO) to vary the wavelength in the near-infrared. In order to generate light in the visible range, frequency tripled Nd:YAG pulses, which emit light with a wavelength of 355 nm, are coupled to an OPO.

Besides pulsed-mode excitation, also cw-lasers can be applied to optoacoustically generate pressure signals. Thereby, the population inversion of the gain medium has to be constantly maintained by a steady pump source. Then, the cw-lasers are able to continuously emit almost monochromatic light. In order to optoacoustically induce pressure waves, the amplitude of the laser output has to be modulated, as constant light energy flux triggers no pressure waves. Commonly cw-lasers are significantly more economic and technically simpler than pulsed lasers.

Optical absorbers within biological tissue have distinct spectral absorption behavior. Therefore, the application of various optical wavelengths in optoacoustic signal generation in combination with dedicated spectral processing algorithms enables unprecedented insight into biological mechanisms [20]. Volumetric MSOT systems have proven to be able to visualize deep-seated biomarkers in real-time [52].

Optoacoustic signal strength scales with the peak power of the applied laser. Although strong optoacoustic signals are desirable, uninhibited laser power can damage and destroy biological tissue. Therefore, the optical excitation process has to comply with laser safety standards for skin exposure, such as the American National Standard for safe use of lasers [53], where values for the maximum permissible exposure (MPE), varying according to their wavelength, are given. All experiments in this work, adhere to the limits given therein.

## 3.2 Ultrasonic Detection

In tissue, optoacoustically induced mechanical energy propagates in form of a traveling pressure wave. Thereby, the size of characteristic absorbers in optoacoustic imaging, defines the frequency band of the emitted pressure wave to be in the ultrasound range. The present section aims at introducing ultrasonic detectors used in optoacoustic imaging systems and gives a short summary over detection techniques and sensor design. Subsequently, basic concepts to characterize commercially available ultrasound transducers are presented. The section is rounded off by an illustration of currently applied optoacoustic detection geometries.

### 3.2.1 Detection Technology

Over the past decades, a variety of technologies to detect ultrasound have been developed. In medical imaging, the vast majority of these technologies rely on piezoelectricity. The piezoelectric effect was first discovered by the brothers Jacques and Pierre Curie in 1880 [54], the same year in which the optoacoustic effect was found. It describes how mechanical deformation of a piezo-material creates molecular dipole moments. All the small electric dipole moments in each piezoelectric cell add up to a change of the electric field, which gives rise to a voltage that can be measured. The piezoelectric effect is reversible, meaning that applying a voltage to a piezo-element causes a mechanical deformation which generates an ultrasonic pressure wave.

Piezoelectricity was first observed in naturally occurring crystals such as tourmaline, quartz, cane sugar and Rochelle salt. Today, synthetic polycrystalline ceramics are used as piezo-elements. The most common one, lead zirconate titanate (PZT), combines robustness and high sensitivity with a reasonable price. PZT has a sound velocity of about  $c_s^{PZT} = 4400 \frac{\text{m}}{\text{s}}$  and density of  $\rho^{PZT} = 7800 \frac{\text{kg}}{\text{m}^3}$ . This makes it a very stiff material exhibiting a narrow frequency response. Furthermore, speed of sound and density differ substantially from the ones of water ( $c_s^{water} \approx 1500 \frac{\text{m}}{\text{s}}$ ,  $\rho^{water} \approx 1000 \frac{\text{kg}}{\text{m}^3}$ ). The behavior in comparison to water is crucial, as water serves as a coupling medium in optoacoustics and is also predominant in biological soft tissue. Therefore, the acoustic impedances  $Z$ , defined as

$$Z = \rho c_s, \quad (3.1)$$

are highly mismatched between PZT and water, causing reflections and therefore loss of signal amplitude. The application of acoustically matching layers can mitigate these effects, however, comes at the price of further reducing the transducer bandwidth. Commercially, PZT is usually doped to increase its piezoelectric response.

Apart from piezoelectric ceramics, however, other optoacoustic applications use ultrasonic detection techniques based on piezoelectric polymer films, such as polyvinylidene fluoride (PVDF)[55]. Here, rather than the crystal structure, the intertwined polymer-chain molecules create the dipole moments. PVDF exhibits acoustical properties closer to the ones of water, having a sound velocity of about  $c_s^{PVDF} = 2200 \frac{\text{m}}{\text{s}}$  and density of  $\rho^{PVDF} =$

1800  $\frac{\text{kg}}{\text{m}^3}$ . Therefore, no coupling medium is needed and the frequency range is broader than in crystals. However, PVDF-transducers possess a significantly lower permittivity  $\epsilon$  and acoustic coupling coefficient  $k_{ac}$  decreasing the energy transfer through the piezo-element. In order to take advantage of both the benefits of piezoelectric crystals and polymers, most ultrasonic transducers in medical imaging are manufactured as piezo-composite materials. The predominant geometrical arrangement is the so-called 1-3 piezo-composite, where a piezo-crystal (e.g. PZT) is cut on one side into small rods. The interstitial volume is then filled with a polymer matrix (usually epoxy) giving the piezo-composite more flexibility than the relatively stiff crystals. By cutting the lower crystal layer one obtains a three-dimensional composite-material block with one-dimensional crystal rods enclosed. The 1-3 piezo-composite combines the high sensitivity of the piezo-crystals with the beneficial acoustic properties of the polymer. The overall acoustic properties can be varied by changing the crystal to matrix ratio. Effective sound speed velocities can be expected to be about  $c_s^{COMP} \approx 3500 \frac{\text{m}}{\text{s}}$  and effective densities range around  $\rho^{COMP} \approx 4000 \frac{\text{kg}}{\text{m}^3}$ . Thereby, large bandwidths, a high acoustic coupling rate and low acoustic impedances can be achieved, resulting in a superior ultrasound transducer. Moreover, due to the elasticity of the piezo-composite material, transducer surfaces can be easily curved to a focus making the use of acoustic lenses dispensable.

Furthermore, ultrasound detection techniques based on optical phenomena, are an active field of research with optoacoustic applications arising. They exploit the interaction of sound and light, captured by Fabry-Pérot interferometers [56] or Fiber-Bragg gratings [57], to detect pressure waves. However, all experimental results presented in this work were acquired using piezo-composite-based ultrasound transducers. Further characterization of ultrasonic transducers, refers to detectors based on piezo-electricity.

### 3.2.2 Acoustic Focusing

Ultrasonic transducers based on the piezoelectric effect have a sensing surface that responds to the impinging pressure waves with a voltage change. The active part of the detector consists of the piezo-element, which in general is manufactured as a flat surface. However, as it is of interest to control the transducer's regions of high sensitivity, a focus can be added to the detector. Thereby, apart from a flat surface, ultrasonic transducers are commonly available with a cylindrical or spherical focus. In general, there are two ways to apply focusing capabilities to a transducer. A simple approach is to equip a flat detector surface with an acoustic lens which imposes either a cylindrical or a spherical focus. Acoustic lenses, however, are often made of glass or acrylic plastics (PMMA) and introduce an additional layer in the transducer. As their basic material is a solid, which has different acoustic properties from water, lenses are the source of additional losses and artifacts in the received signal. Another, way to create a focus, is to simply shape the flat piezo-element. Previously described piezo-composites incorporate material characteristics of both crystals and polymers. Taking advantage of the flexibility of polymers, they can be bended to part of a cylinder or a sphere in order to mechanically generate a cylindrical or spherical focus. In this way, no additional layer has been introduced and the pressure wave can directly hit

the piezo-element. Ultrasonic transducers with different focuses are depicted in figure 3.1.

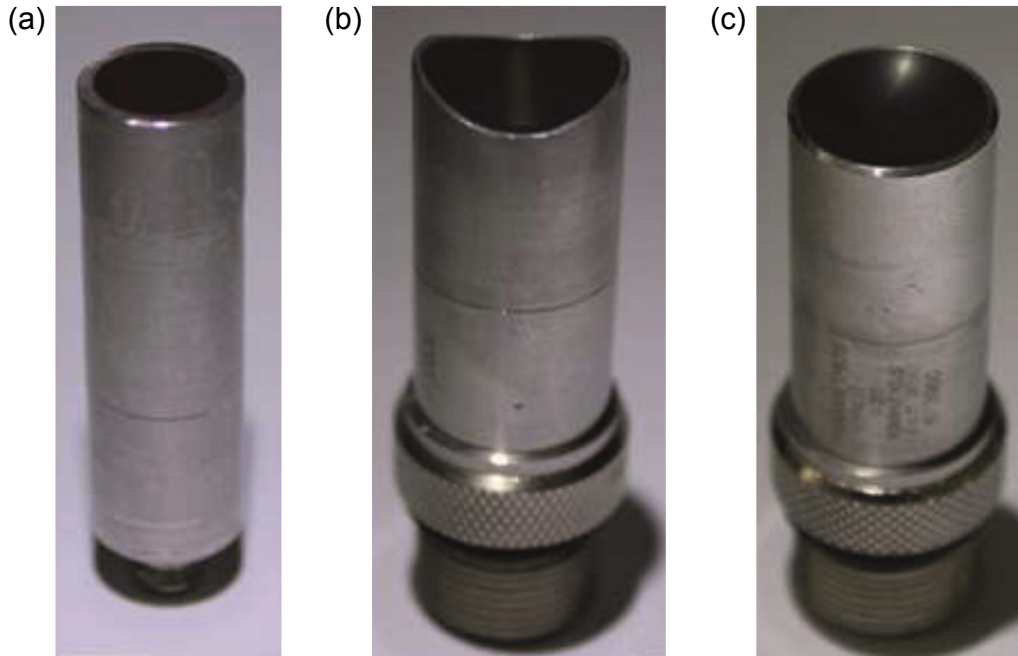


Figure 3.1: Different geometries of piezoelectric ultrasound transducers. (a) shows a flat transducer. (b) depicts a cylindrically focused and (c) a spherically focused detection surface.

### 3.2.3 Transducer Characterization

The frequency response of ultrasonic transducers is often characterized by their central frequency  $f_c$  (MHz) and their fractional bandwidth  $BW$  (%) at -6dB. Assuming a Gaussian distribution of the detector's frequency response,  $f_c$  denotes the frequency with maximum detection capability.  $f_c(1 - \frac{BW}{2})$  and  $f_c(1 + \frac{BW}{2})$  define the lower and upper boundary frequencies, respectively, where the detector's sensitivity drops to 50% of the peak performance. Consider, as an example, a transducer with central frequency of  $f_c = 10$  MHz and fractional bandwidth  $BW = 60\%$ . Then, the transducer would detect with 50% or more of its peak sensitivity between 7 MHz and 13 MHz.

In front of the active element of the transducer, space can be separated into two zones, the near field and the far field. In the near field, which is situated directly in front of the transducer, the sensitivity of the transducer traverses a series of maxima and minima. The near field region is limited by the last sensitivity maximum, denoted the near field distance  $N$ . This distance  $N$  is referred to as the natural focus of a flat detector and can

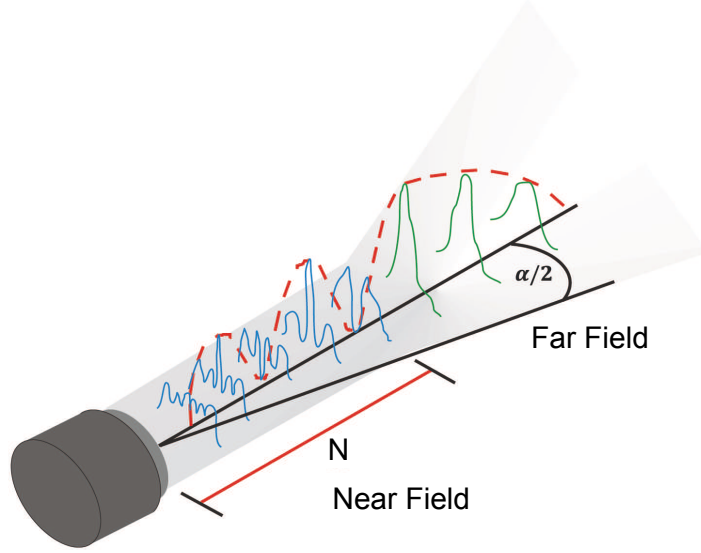


Figure 3.2: Near and far field of a flat transducer.  $\alpha/2$  defines half of the beam spread angle.

be calculated for a round piezo-element by

$$N = \frac{D^2 f}{4c_s} = \frac{D^2}{4\lambda}. \quad (3.2)$$

Here,  $D$  denotes the piezo-element's diameter,  $f$  denotes frequency,  $\lambda$  is the wavelength and  $c_s$  stands for the speed of sound in the respective medium. Wavelength and frequency are related via

$$f = \frac{c_s}{\lambda}. \quad (3.3)$$

From the near field distance on, the far field starts with the detectors sensitivity gradually decreasing to zero, which can be seen in figure 3.2. By propagating through the far field, the ultrasonic sensitivity range diverges. Although the peak of its energy stays on the central axis, the beam becomes consistently weaker remote from the axis. The -6dB beam spread angle  $\alpha$  is given by the formula

$$\sin(\alpha/2) = 0.514 \frac{c_s}{f_c D}. \quad (3.4)$$

Focused transducers have a third region, called the focal zone, which lies between the near and the far field. When considering cylindrically focused transducers, the -6dB length of the focal zone  $F_Z$  can be calculated as

$$F_Z = \frac{1.1c_s}{f_c (1 - \cos(\theta/2))}, \quad (3.5)$$

where  $\theta$  denotes the aperture angle [58],[59]. The -6 dB height  $F_H$  of the focal zone is then given by

$$F_H = \frac{c_s}{2f_c \sin(\theta/2)}. \quad (3.6)$$

For spherically focused transducers, Hunt et al. [60] derived the extent of the focal zone  $F_Z$  as

$$F_Z = 9.7 \frac{c_s}{f_c} \left( \frac{F}{D} \right)^2, \quad (3.7)$$

with  $F$  defining the focal length of the detector. Then, up to a constant, the -6 dB height  $F_H$  of the focal zone is given by 3.6, the formula for cylindrically focused transducers

$$F_H = 1.41 \frac{c_s}{2f_c \sin(\theta/2)}. \quad (3.8)$$

### 3.2.4 Impulse Responses

In optoacoustics, light absorbing structures generate transient pressure waves via thermoelastic expansion. These pressure signals are subsequently detected and recorded by an ultrasonic transducer and a data acquisition system (DAQ). Taking advantage of the piezoelectric effect, the impinging pressure waves are thereby converted to a voltage signal, which is picked up by electrodes and forwarded to a data storage unit. An ultrasound transducer, performing the transformation of a pressure wave to a voltage signal recorded by a DAQ, can be modeled as a linear, time-invariant system [61] [62]. Consequently, the detector is entirely described by its response to a delta excitation. This response, termed total impulse response (TIR)  $h_{TIR}(\vec{r}_c, \vec{r}', t)$ , is a characteristic function defining the detector. The TIR is dependent on the detector position  $\vec{r}_c$ , the position of the delta-source  $\vec{r}'$  and time  $t$ . A general propagating pressure wave reaching position  $\vec{r}_c$  will therefore be detected as

$$p_{det}(\vec{r}_c, t) = h_{TIR}(\vec{r}_c, \vec{r}', t) *_t p(\vec{r}_c, t), \quad (3.9)$$

where  $*_t$  stands for the temporal convolution operator. The total impulse response (TIR) incorporates all effects on the signal  $p$  due to the transducer. It can be differentiated into a spatially dependent part describing the detector's geometry and a spatially independent part modeling the material components and the entire electric transduction of the detector. The first part is termed spatial impulse response (SIR) whereas the latter is denoted as the electrical impulse response (EIR). Overall the detected signal  $p_{det}$  can be expressed as

$$p_{det}(\vec{r}_c, t) = h_{EIR}(t) *_t h_{SIR}(\vec{r}_c, \vec{r}', t) *_t p(\vec{r}_c, t). \quad (3.10)$$

The acoustic pressure  $p$  is consecutively convolved with the SIR and EIR.

#### Spatial Impulse Response

Optoacoustically induced pressure waves are mathematically modeled with the wave equation Cauchy problem 2.53 - 2.55. Thereby, the ultrasonic detector is assumed to be an

infinitesimal small point in space. In order to determine the pressure wave emitted by an arbitrary absorber, one can use the Green's function of the wave equation. The Green's function of a PDE is the solution of the inhomogeneous PDE with a delta source term. In case of the optoacoustic wave equation this means considering an infinitesimal short laser-pulse at an infinitesimal small position  $\vec{r}'$  in space. The Green's function for the three-dimensional wave equation has already been calculated as 2.68. Then, dropping the constant and assuming a delta source positioned at  $\vec{r}'$ , the Green's function becomes

$$g(\vec{r}, \vec{r}', t) = \frac{\delta\left(t - \frac{|\vec{r} - \vec{r}'|}{c_s}\right)}{4\pi|\vec{r} - \vec{r}'|}. \quad (3.11)$$

An arbitrary source function  $H_r$  can then be considered as consisting of spatial delta-like source terms. As in 2.72, the wave equation solution  $p$  with an arbitrary source function  $H_r$  is calculated as the superposition of Green's functions, weighted with the source  $H_r$

$$p(\vec{r}, t) = \frac{\Gamma}{4\pi} \frac{\partial}{\partial t} \iiint_{\mathbb{R}^3} H_r(\vec{r}') \frac{\delta\left(t - \frac{|\vec{r} - \vec{r}'|}{c_s}\right)}{|\vec{r} - \vec{r}'|} d\vec{r}'. \quad (3.12)$$

Note, that the source term is only arbitrary in its spatial dimension as the temporal profile is kept as a delta-impulse. The underlying assumption of the above rationale is that the detector is confined to a point in space. This deviates from realistic piezo-electric transducers where the active element has an extended surface, which may be even curved to a focus. The actual pressure signal exciting the transducer surface,  $p_S$ , is therefore expressed as

$$p_S(\vec{r}_c, t) = \iiint_{\mathcal{S}} p(\vec{r}, t) d\vec{r} = \iint_{\mathcal{S}} p(\vec{r}_d, t) dS(\vec{r}_d), \quad (3.13)$$

the integral over the pressure reaching the active surface  $\mathcal{S}$  of the transducer. Thereby,  $\vec{r}_d$  denotes the positions on the detector surface  $\mathcal{S}$ . The position of the detector itself is defined by the center  $\vec{r}_c$  of its surface  $\mathcal{S}$ . Accordingly, the emanating pressure wave hits different parts of the detector surface at different time instants. As a consequence, the detected signal is stretched and appears to be longer than the actually emitted pressure wave. This effect is modeled by the SIR of the transducer. The SIR is spatially dependent, as it is determined by the geometry of the transducer surface and the position of the source of the pressure wave.

In order to calculate the spatial impulse response  $h_{SIR}$ , one has to integrate the point-source solution 3.11 over the detector surface  $\mathcal{S}$ ,

$$h_{SIR}(\vec{r}_c, \vec{r}', t) = \iint_{\mathcal{S}} \frac{\delta\left(t - \frac{|\vec{r}_d - \vec{r}'|}{c_s}\right)}{4\pi|\vec{r}_d - \vec{r}'|} dS(\vec{r}_d). \quad (3.14)$$

Inserting 3.14 into 3.12 yields

$$p_S(\vec{r}_c, t) = \frac{\Gamma}{4\pi} \frac{\partial}{\partial t} \iiint_{\mathbb{R}^3} H_r(\vec{r}') h_{SIR}(\vec{r}_c, \vec{r}', t) d\vec{r}' \quad (3.15)$$

$$= \frac{\Gamma}{4\pi} \frac{\partial}{\partial t} \iiint_{\mathbb{R}^3} H_r(\vec{r}') \left[ \oint_{\mathcal{S}} \frac{\delta\left(t - \frac{|\vec{r}_d - \vec{r}'|}{c_s}\right)}{|\vec{r}_d - \vec{r}'|} dS(\vec{r}_d) \right] d\vec{r}', \quad (3.16)$$

the expression for the pressure emitted by an arbitrary source  $H_r$ , detected on a realistic transducer's surface  $\mathcal{S}$ . The expression in 3.15 can be rewritten as

$$p_S(\vec{r}_c, t) = \frac{\Gamma}{4\pi} \frac{\partial}{\partial t} \iiint_{\mathbb{R}^3} H_r(\vec{r}') h_{SIR}(\vec{r}_c, \vec{r}', t) d\vec{r}' \quad (3.17)$$

$$= \frac{\Gamma}{4\pi} \iiint_{\mathbb{R}^3} H_r(\vec{r}') \left[ h_{SIR}(\vec{r}_c, \vec{r}', t) *_t \frac{\partial}{\partial t} \delta(t) \right] d\vec{r}' \quad (3.18)$$

$$= \frac{\Gamma}{4\pi} \iiint_{\mathbb{R}^3} |\vec{r}_c - \vec{r}'| h_{SIR}(\vec{r}_c, \vec{r}', t + \frac{|\vec{r}_c - \vec{r}'|}{c_s}) *_t \frac{\partial}{\partial t} \frac{\delta(t - \frac{|\vec{r}_c - \vec{r}'|}{c_s})}{|\vec{r}_c - \vec{r}'|} H_r(\vec{r}') d\vec{r}', \quad (3.19)$$

where  $*_t$  again denotes the temporal convolution operator. Comparing equation 3.19 with equation 3.12, one observes that the signal detected by a finite-size transducer can be expressed as one received by a point-detector convolved with the function  $|\vec{r}_c - \vec{r}'| h_{SIR}(\vec{r}_c, \vec{r}', t + \frac{|\vec{r}_c - \vec{r}'|}{c_s})$ .

Integral 3.14 can be solved analytically for several detector shapes in two and three dimensions [36],[63]. Geometric detector properties can severely deteriorate the accuracy of medical imaging devices and are therefore widely-studied [38],[64],[39]. Chapter 5 of this work is dedicated to the analysis of image artifacts arising from the geometrical shape of the transducer surface [37]. Techniques to account for geometrical detector properties are presented and their positive effects are showcased in simulations and experiments.

### Electrical Impulse Response

Upon impinging on the detector surface, the ultrasonic wave compresses the transducer's piezo-element, which gives rise to a voltage. The incoming pressure signal thereby excites oscillations of the piezo-surface. The frequencies of these oscillations are defined by the material characteristics that specify the resonance frequency and bandwidth of the piezo-element. Each vibration of the sensing element provokes a voltage change being measured with electrodes connected on each side of the piezo-element. Subsequently, the electric signal is picked up by the transducer's wiring before it can be visualized with an oscilloscope. The entire conversion of the pressure signal to an electric signal is described by the EIR. Parameters influencing the EIR are the material characteristics of the piezo-element, possible acoustical matching layers and the transducer backing as well as the entire electric transmission behind the sensing element. Since all the influencing parameters of the EIR are only related to the material, it can be expressed as a spatially independent function

$h_{EIR}(t)$ .

Commonly, as the EIR is detector-specific, it is measured experimentally in order to calibrate each detector. Therefore, a delta-like source in time and space is employed to generate ultra-wide band pressure signals. In order to decouple the SIR from the EIR, the emanating pressure wave should impact on the entire detector surface at the same time instant. This means, that focused transducers should be impinged by spherical waves generated at the focus. For flat transducers, spherical waves generated in the far field can be considered as approximate plane waves exciting the detector surface.

Rosenthal et al. [65] presented two techniques to measure the TIR of piezo-electric transducers by means of optoacoustically excited absorbers. It avoids techniques where pre-calibrated hydrophones or pulse-echo measurements are required [66] [67]. Caballero et al. [68] built upon Rosenthal's work to develop a robust measurement procedure that determines the EIR of an ultrasound transducer. Thereby, a hybrid approach was adopted where experimental measurements as well as theoretical results were used. Depending on the actual geometry of the detector surface, the corresponding SIR was first calculated either analytically or numerically [69]. After that, a point source, positioned arbitrarily in front of the transducer was excited. In order to ensure the best SNR, the point source was placed at the focal point of the transducer. Up to constants, the source term can be approximated by a delta function in space and time,  $H(\vec{r}, t) = \delta(\vec{r})\delta(t)$ . Then by taking 2.72 and 3.10 into account, the measured signal reduces to

$$p_{det}(\vec{r}_c, t) = \frac{\partial}{\partial t} h_{EIR}(t) *_t h_{SIR}(\vec{r}_c, \vec{r}', t). \quad (3.20)$$

Finally, to ensure that the EIR is truly independent of the source position, the effect of the SIR at source position  $\vec{r}'$  has to be taken out by deconvolution. This can be easily done in the frequency domain where a deconvolution reduces to a division. Then, the EIR is given as a simple integration

$$h_{EIR}(t) = \int_0^t p_{det}(\vec{r}_c, t') dt'. \quad (3.21)$$

Overall, the EIR acts as a bandpass-filter on the pressure signals, around its central frequency defined by the material parameters. Once measured, its effect can be corrected by simply deconvolving the detected signals with the EIR.

### 3.3 Detection Geometries

Currently, there exists a huge variety of optoacoustic imaging systems. In preclinical research, they cover the range from microscopy of single cells to volumetric small-animal tomography systems. In clinical applications, hand-held systems for breast imaging, as well as intra-vascular plaque imaging have been reported. Depending on the imaging target, optoacoustic setups differ in acquisition geometry and transducers applied. The present section aims at providing an overview of conventional imaging setups.

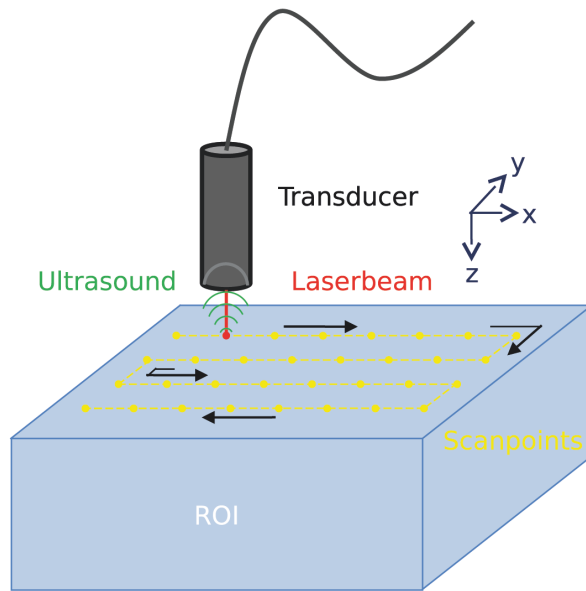


Figure 3.3: Rasterscanning a spherically focused transducer in optoacoustic microscopy.

### 3.3.1 Microscopy

In optoacoustic microscopy (OAM) systems a single transducer is positioned perpendicularly on top of the ROI. In order to obtain the best resolution possible, optical excitation as well as ultrasonic detection are focused and aligned. Thereby, the beam diameter is tightened with lenses and positioned on the same axis as the transducer. This can be achieved by either illuminating through the detector [70] or by generating a ring shaped illumination pattern enclosing the transducer [71]. The ultrasound detector is spherically focused with a central frequency of several tens to 100 MHz. As excitation and detection are aligned co-axially and con-focally, signals generated laterally to that axis are effectively rejected. In this configuration, at each detector position, a 1D signal is recorded corresponding to an amplitude-mode (A-mode) measurement. Thereby, depth information about the ROI is recovered by multiplying the detected time signal by the speed of sound  $c_s$  of tissue. Then, by scanning the transducer along a line, 2D images can be generated by stacking a series of A-mode measurements. 3D volumes can readily be obtained by raster-scanning the transducer in the xy-plane, see figure 3.3.

### 3.3.2 Endoscopy

Optoacoustic endoscopy (OAE) aims at imaging internal organs such as the colon or arteries [72], [73]. Thereby, both laser excitation and ultrasound detection are miniaturized to fit into an endoscope. Laser light is delivered by a multimode optical fiber directly into the lumen. There, it is deflected by a mirror positioned at an angle, in order to excite tissue

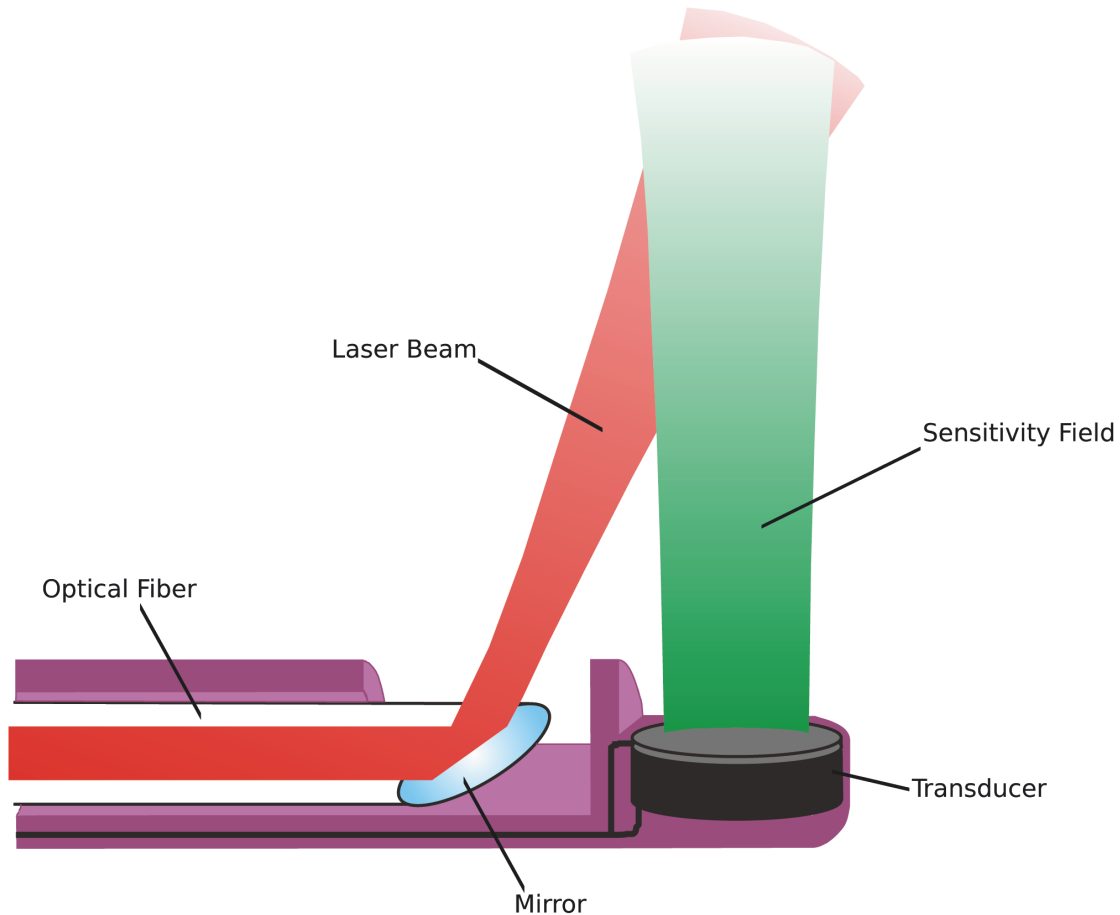


Figure 3.4: Schematic representation of an optoacoustic endoscope. The laser light source is guided by an optical fiber within the endoscope. Deflected by a mirror, the light source excites tissue surrounding the endoscope. The sensitivity field of the ultrasonic transducer overlaps with the laser beam.

parallel to the catheter axis. A single ultrasound detector is positioned at the end of the catheter. Oriented perpendicularly to the catheter axis it captures the ultrasound generated in the adjoining tissue. Thereby, the field of view of the detector overlaps with the tissue region excited by the light source (figure 3.4). Both laser light and transducer are rotated to obtain a full-view dataset. Entire volumes can be imaged by simply pulling back the entire catheter.

### 3.3.3 Tomography

Optoacoustic tomography (OAT) systems generate cross-sectional images of the ROI. Thereby, the entire ROI is excited by an expanded optical beam. A set of measurements is acquired at multiple positions surrounding the ROI, serving as the input of a

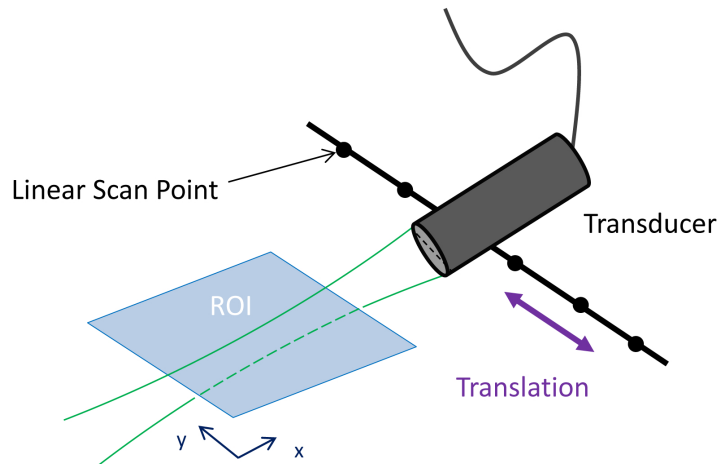


Figure 3.5: Linear scan in a two-dimensional OAT.

dedicated reconstruction algorithm. OAT systems can be divided into two-dimensional and three-dimensional systems.

### Two-dimensional OAT

As light can not be focused beyond the ballistic regime of photons, optoacoustic pressure signals are inherently generated in three dimensions. Furthermore, pressure waves emitted by small absorbers will also propagate in all spatial directions. However, by focusing the sensitivity region of the ultrasonic detection to a plane, pressure waves can be considered to emanate from two dimensions only. Thereby, cylindrically focused transducers aim at rejecting all signals generated outside the focal plane. A set of measurements is then taken by scanning the transducer either along a line (figure 3.5) [74] or along a circle (figure 3.6) enclosing the plane with the ROI [22] [75]. In order to enable real-time imaging, transducer arrays with parallel data acquisition are commonly applied.

### Three-dimensional OAT

Three-dimensional OAT aims at reconstructing a volumetric ROI. For that, similarly as in the 2D case, optoacoustically generated pressure waves have to be measured on a surface enclosing the volume to be reconstructed. Commonly, there are two preferred geometries to position detectors in 3D.

First, extending the approach from 2D OAT, a detector ring is additionally scanned in elevational direction to form a cylindrical detection surface (figure 3.7) enclosing the ROI [22] [76]. Thereby, either a set of 2D images is reconstructed and stacked together to form a 3D volume, or a three-dimensional reconstruction algorithm recovers the volumetric ROI taking into account all data acquired. The cylindrical detection approach is widely-used as it allows to combine both a 2D and a 3D detection scheme in one system.

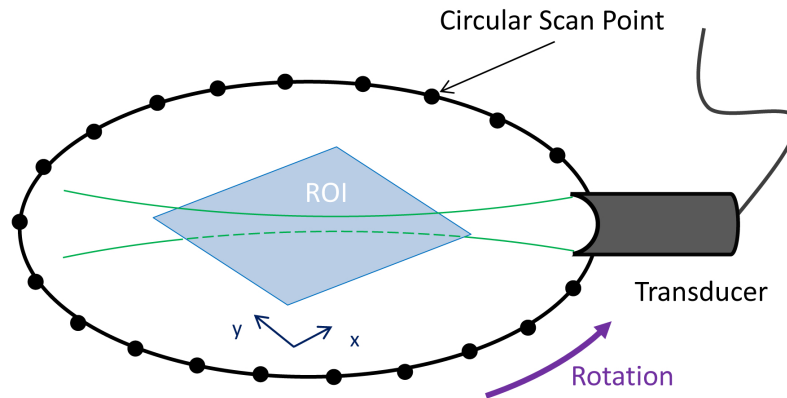


Figure 3.6: Circular scan in a two-dimensional OAT system.

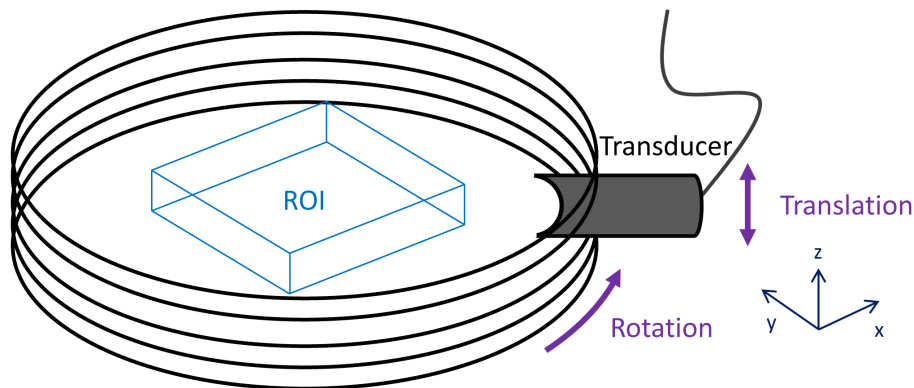


Figure 3.7: Three-dimensional OAT with a cylindrical detection geometry obtained by translating and rotating a single transducer.

Second, ultrasonic detectors are positioned to cover a sphere enclosing the ROI. This geometry has been implemented by either rotating an arc-shaped detector array [77], as can be seen in figure 3.8, or by actually positioning the transducers on a spherical surface [78],[79],[80].

Both, cylindrical geometry and spherical geometry, consider the optoacoustic effect in three dimensions. In order to assure consistent excitation conditions, wide-beam illumination is necessary. Furthermore, in the spherical case, ultrasound transducers should be as point-like and omnidirectional as possible. However, imaging systems including extended or focused transducers require reconstruction algorithms taking the detection surface into account.

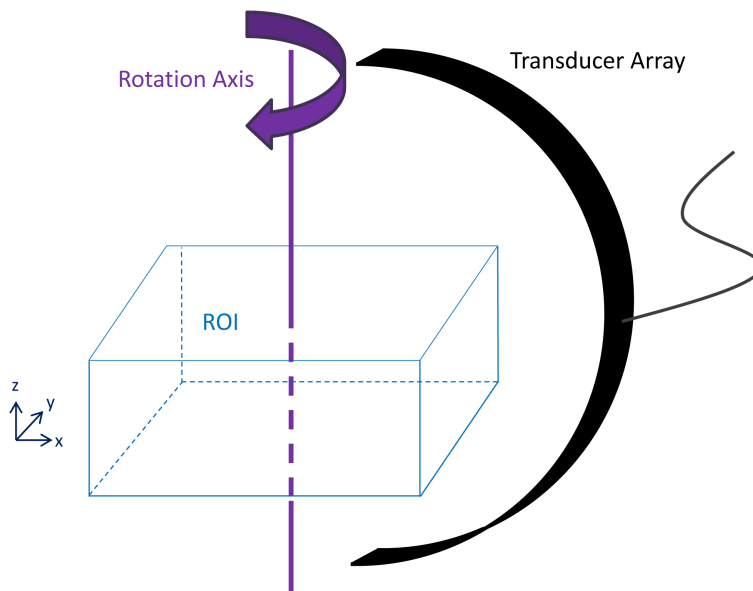


Figure 3.8: Three-dimensional OAT with detectors positioned to cover a sphere.

## 3.4 Optoacoustic Systems

In this section three optoacoustic systems are presented. They are all tomographic systems, acquiring pressure signals on a circumference surrounding the ROI. The first two have the ability to scan in elevational direction in order to acquire data from a cylindrical detection surface. All experimental results presented in this work were acquired with the systems introduced in this section.

### 3.4.1 Single Transducer System

The layout of the first tomographic optoacoustic system can be seen in figure 3.9. Optoacoustic signals are measured by a standard cylindrically focused piezoelectric immersion transducer (Panametrics V320-SU, Olympus NDT Inc., Waltham, MA, USA) with a diameter of 1.3 cm and a focal length of 2.54 cm (see figure 3.1). The central frequency of the transducer is  $f_c = 7.5$  MHz with a fractional bandwidth BW of 70%. Optoacoustic pressure waves are excited with a tunable optical parametric oscillator (OPO) laser (Phocus, Oportek Inc., Carlsbad, California, USA), delivering  $\approx 5$  ns duration pulses with a repetition frequency of 10 Hz. The wavelength of the excitation laser can be tuned from 680 to 950 nm. As a pump laser within the OPO serves a frequency doubled Nd:YAG solid state laser with an output wavelength of 532 nm. The OPO laser output is set at a wavelength of 760 nm, corresponding to the maximum power of the laser in the near-infrared spectrum. Acquired signals at each projection are averaged 10 times for better SNR. Subsequently, the signals are deconvolved with the EIR and bandpass filtered from 0.5 to 12 MHz. The laser beam is guided with a fiber bundle into the water tank and, due to spatial limitations,

deflected with a mirror in order to uniformly illuminate the sample from the bottom. The transducer is kept at a fixed position while the sample is rotated and moved in elevational direction by means of rotation and translation stages (PRM1/M-Z7 and NRT150, Thorlabs GmbH, Dachau, Germany). The Q-switch output of the laser is used to trigger the data acquisition card (Spectrum, M3i.4121, Spectrum Systementwicklung Microelectronic GmbH, Grosshansdorf, Germany) embedded in the personal computer controlling the stages.

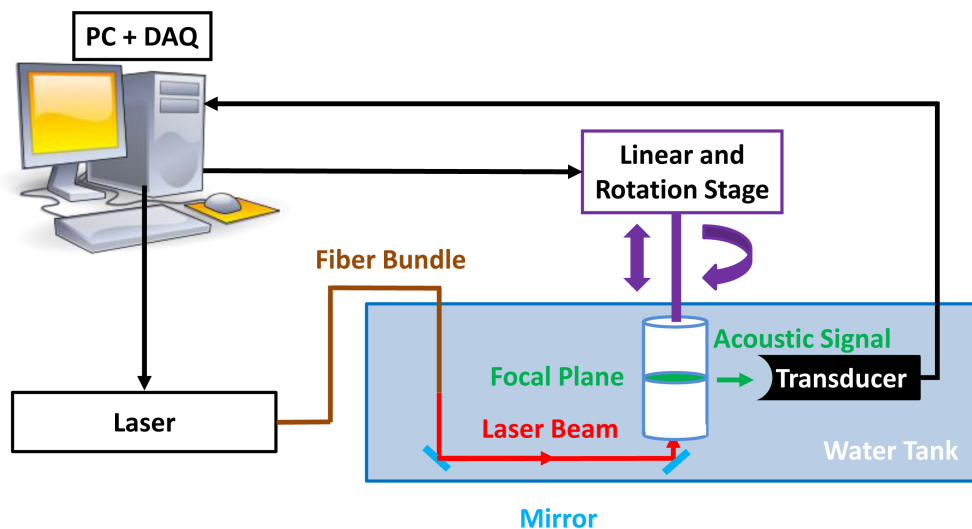


Figure 3.9: Schematic of an optoacoustic imaging system scanning a single focused transducer along a cylindrical detection geometry.

### 3.4.2 Transducer Array System

The second tomographic system is the first version of a commercially available small animal optoacoustic imaging system. It is based on a custom-made 64-element curved transducer array (Imasonic SaS, Voray, France) covering a solid angle of  $172^\circ$  around the imaged object, as shown in figure 3.10. The individual elements are manufactured using piezo-composite technology with a central frequency of  $f_c = 5$  MHz and a fractional bandwidth BW of more than 50%. The sensitivity of each element is  $\approx 18 \mu\text{V}/\text{Pa}$ . The entire transducer array is shaped to create a cylindrical focus at 40 mm. According to the ultrasonic diffraction limit and focal width at the central frequency, the effective spatial resolution of the array is estimated at  $150 \mu\text{m}$  in plane [38] and  $800 \mu\text{m}$  in elevational direction, see equation 3.6. Again, excitation light originates from the tunable OPO laser (Phocus, Opotek Inc., Carlsbad, CA, USA), delivering  $\approx 5$  ns duration pulses with a repetition frequency of 10 Hz. The tuning range enables a laser wavelength from 680 to 950 nm. The beam is guided into a silica-fused-end fiber bundle (PowerLightGuide, CeramOptec GmbH, Bonn, Germany) consisting of 630 fibers partitioned into 10 arms. The arms are positioned 3 cm from the ROI and create a ring-shaped illumination pattern of  $\approx 7$  mm width upon

the surface of the ROI, coinciding with the ultrasound detection plane. The beam is sufficiently broadened to keep the laser pulse fluence on the surface of the imaged objects under  $20 \text{ mJ/cm}^2$ . The detected signals are digitized at a frequency of 60 megasamples/s by eight multichannel analog-to-digital converters (PXI5105, National Instruments, Austin, Texas, USA) having a noise floor of  $\approx 3.8 \text{ nV}/\sqrt{\text{Hz}}$ . Before used for image reconstruction, the optoacoustic signals are bandpass filtered from 0.1 to 7 MHz. To facilitate *in-vivo* measurements, the system contains an imaging chamber that holds animals inside a water-impenetrable membrane that avoids animal contact with water while providing a wide tomographic view of  $\approx 180^\circ$ . Recent versions of the system offer a detection arc with 256 individual transducers covering an angle of  $270^\circ$ . A linear stage (NRT150, Thorlabs GmbH, Dachau, Germany) allows linear translation of the animal holder in the elevational z-direction over a 150 mm range with a minimal step size of  $2 \mu\text{m}$  for acquisition of 3D data sets. The data acquisition is synchronized so that the signals are acquired only when the stage comes to a complete rest.

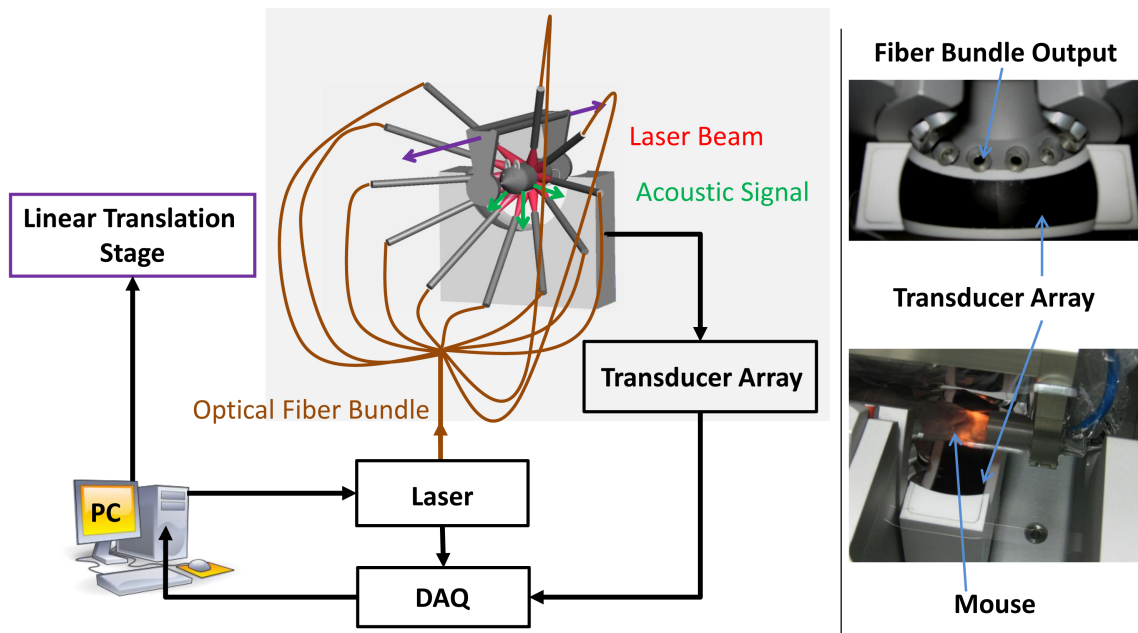


Figure 3.10: Schematic of an optoacoustic transducer array imaging system.

### 3.4.3 cw-Laser System

Optoacoustic imaging with a cw-laser is performed by a system (figure 3.11) employing a temperature-stabilized diode laser (Omicron A350, Omicron-Laserage Laserprodukte GmbH, Dudenhofen, Germany), [47]. The laser emits a collimated cw beam at 808 nm with a peak power of 500 mW achieving an illumination spot of  $\approx 5 \text{ mm}$  diameter. LFM laser chirps are generated using a function generator (33210A, Agilent Technologies, Santa

Clara, California, USA) with the capability to analog modulate the laser intensity at a frequency range of 0 – 350 MHz. However, all experimental data shown herein was acquired applying a frequency sweep from 1 to 5 MHz within a duration of 1 ms. Ultrasonic pressure waves are detected by a cylindrically focused transducer (Panametrics V382, Olympus-NDT Inc., Waltham, Massachusetts, USA) with a central frequency of 3.5 MHz, a focal distance of 38.1 mm and a fractional bandwidth of 76%. Simultaneous rotation of the optical excitation system and detector is realized with a rotation stage (PR50PP, Newport Corporation, Irvine, California, USA). Then, optoacoustic signals are acquired every 2°, resulting in 180 projections and  $\approx 10$  min acquisition time per full rotation. For better SNR the signals are averaged 50 times at every detector position. In comparison to pulsed optoacoustic systems, which use high energy pulses of typically more than 10 mJ per pulse, cw-laser systems provide lower energies, yet operate at significantly higher duty cycles, partially compensating for SNR losses. A portion of the emitted modulated light is concurrently captured by a photo-diode for reference. Both, the optoacoustic and laser reference signals, are digitized by a digital phosphor oscilloscope (DPO 7254, Tektronix Inc., Beaverton, Oregon, USA) after amplification with a low-noise 65 dB amplifier (AU-1291, Miteq, Hauppauge, New York, USA) at 50 megasamples/s. In order to assure the synchronization of the data acquisition system and the function generator driving the diode laser, a trigger generator (MXG5181, Agilent Technologies, Santa Clara, California, USA) is interconnected. Data acquisition, positioning, and post-processing is enabled by a custom-made code developed within MATLAB (Mathworks, Natick, Massachusetts, USA).

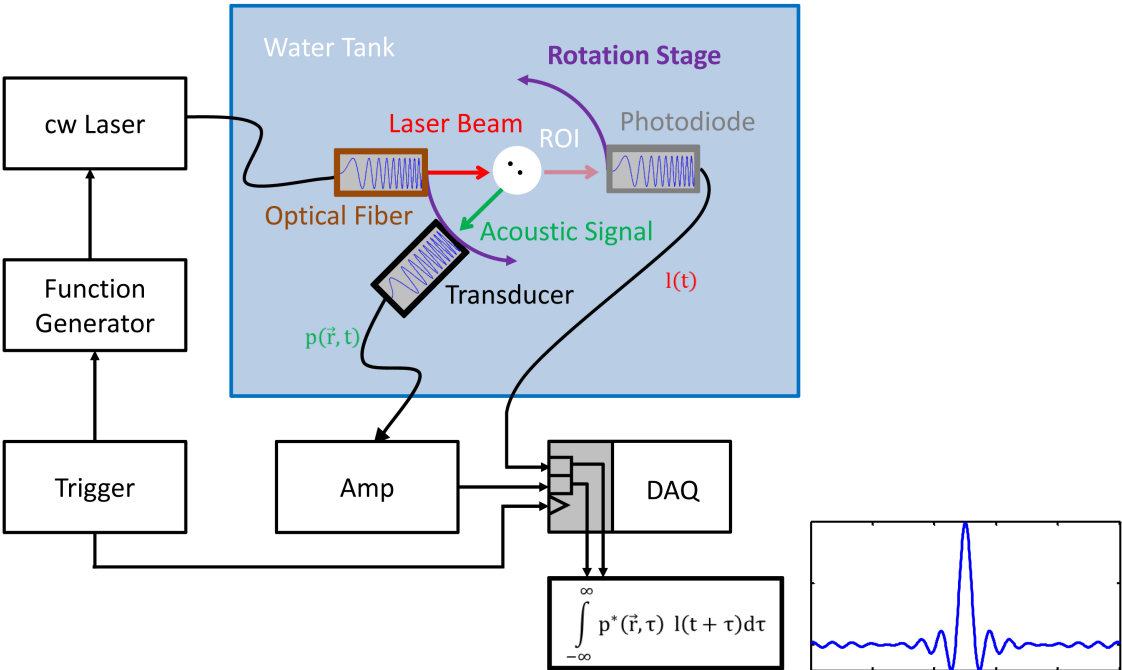


Figure 3.11: Schematic representation of the optoacoustic imaging system employing chirped excitation by a cw-laser.



# Chapter 4

## Reconstruction Algorithms

In this chapter, an overview of optoacoustic reconstruction algorithms is given, which contains concepts adapted from [81]. Thereby, a distinction between analytic inversion formulas in time- and frequency-domain and algebraic inversion procedures is made. Underlying assumptions of each algorithm are explained and its advantages and shortcomings are presented. Starting point of all reconstruction algorithms presented herein, is the forward solution of the wave equation Cauchy problem 2.53 – 2.55 without constants (see 2.72)

$$p(\vec{r}, t) = \frac{\partial}{\partial t} \iiint_{|\vec{r}-\vec{r}'|=c_s t} \frac{H_r(\vec{r}')}{|\vec{r}-\vec{r}'|} d\vec{r}'. \quad (4.1)$$

Furthermore, all simplifying assumptions from section 2.2.1 apply.

The aim of every reconstruction algorithm is to recover the spatial distribution  $H_r(\vec{r})$  from pressure measurements  $p(\vec{r}, t)$  obtained on a boundary  $B$  enclosing the ROI. Thereby, the boundary  $B$  is defined by the dimension of the optoacoustic system. In two dimensions,  $B$  will be a theoretically infinite line or a circle, whereas three-dimensional systems consider commonly infinite planes, cylinders or spheres.

The image one tries to recover is defined by the spatial distribution of the heating function  $H(\vec{r}) = \eta_{th} \Phi_r \mu_a(\vec{r})$ . Thereby, it is assumed that heat conversion efficiency  $\eta_{th}$  and optical fluence rate  $\Phi_r$  are constant in space. Therefore, reconstructed images will only depend on the spatially varying optical absorption coefficient  $\mu_a(\vec{r})$ .

### 4.1 Analytic Inversion Algorithms

Analytic reconstruction techniques are characterized by inverting the mathematical model of the optoacoustic pressure propagation by means of analytical inversion of the mathematical equations. Inexactness arises only in the discrete numerical implementation of the algorithms.

### 4.1.1 Time Domain Algorithms

First analytic inversion formulas for optoacoustic imaging devices have been suggested in the time domain by Kruger et al.[26]. In general, time-domain algorithms are designed in a way that can be separated into three parts.

#### 1. Preprocessing

The input data of any optoacoustic reconstruction algorithm consists of a set of pressure measurements  $p(\vec{r}_i, t)$  obtained at  $M$  positions  $\vec{r}_1 \dots \vec{r}_M$  on the measurement boundary  $B$ . This set of one-dimensional time-domain signals is, depending on the algorithm, mathematically altered to define a new function  $b(\vec{r}_i, t)$ .

#### 2. Back-Projection

The set of functions  $b(\vec{r}_i, t)$  is propagated back into the ROI. Thereby, based on the time of flight principle, each position in space at a distance of  $c_s t$  from detector position  $\vec{r}_i$  gets assigned with the value  $b(\vec{r}_i, t)$ . Accordingly, in three dimensions, a radial function

$$b_r^i(\vec{r}) = b(\vec{r}_i, \frac{\|\vec{r} - \vec{r}_i\|}{c_s}) \quad (4.2)$$

gets defined, specifying values on concentric spheres centered at detector position  $\vec{r}_i$ . In two dimensions, these spherical shells reduce to circles. Depending on the algorithm, additional spatial operations like weighting may be performed.

#### 3. Integration

The final step of the algorithm combines all the data back-projected into the ROI from the previous step. Thereby, an integration over all detector positions  $\vec{r}_i$  lying on boundary  $B$  reduces to a summation of all functions  $b_r^i$ .

The most elementary realization of an above described inversion algorithm is the so-called 'delay-and-sum' algorithm [27]. Thereby, the set of functions  $b$  being defined in the preprocessing step are simply the pressure measurements itself,

$$b(\vec{r}_i, t) = p(\vec{r}_i, t). \quad (4.3)$$

Then, the reconstruction formula of the delay-and-sum algorithm reads as

$$H(\vec{r}) = \iint_B \left[ p(\vec{r}', t) \right]_{t=|\vec{r}-\vec{r}'|/c_s} dS(\vec{r}'). \quad (4.4)$$

One of the most prominent optoacoustic time-domain inversion formulas is the Universal Back-Projection algorithm, which has been published in 2005 [28]. The algorithm was initially derived for planar, cylindrical and spherical detection geometries by analytically inverting equation 4.1. In this case, function  $b$  defined during the preprocessing step is

$$b(\vec{r}, t) = 2p(\vec{r}, t) - 2t \frac{\partial p(\vec{r}, t)}{\partial t}. \quad (4.5)$$

Apart from a varying weighting-factor, compensating for different solid angles belonging to different detection geometries, the inversion formula reduces to

$$H(\vec{r}) = \iint_B \left[ 2p(\vec{r}', t) - 2t \frac{\partial p(\vec{r}', t)}{\partial t} \right]_{t=|\vec{r}-\vec{r}'|/c_s} dS(\vec{r}'), \quad (4.6)$$

for all geometries.

Implementation of the back-projection formula 4.6 is straightforward as can be seen exemplarily for the two-dimensional case and a circular detection boundary in figure 4.1. Thereby,

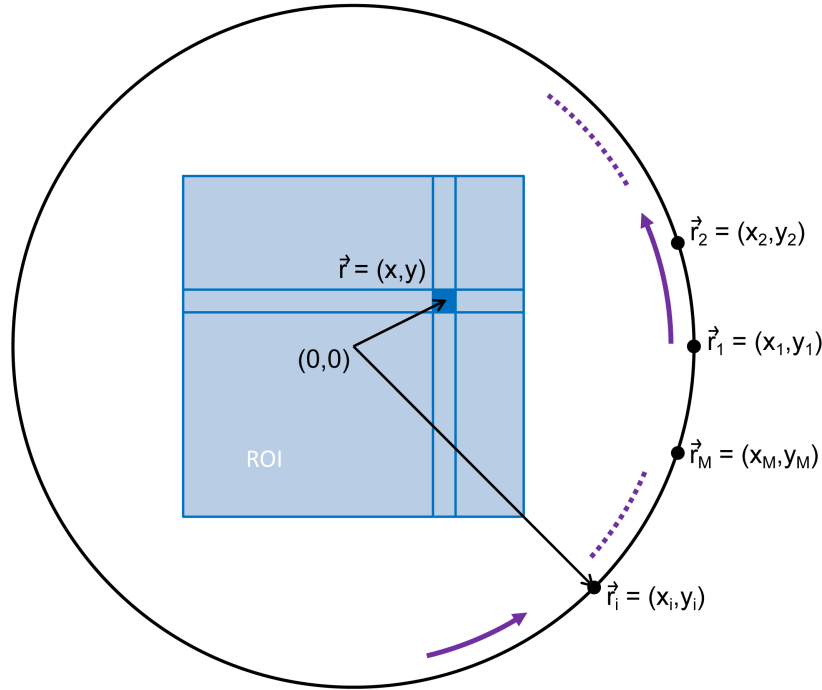


Figure 4.1: Geometry for the two-dimensional Universal Back-Projection formula.

the ROI is discretely represented by their pixel values with x- and y-coordinates,  $H(\vec{r}) = H(x, y)$ . The pressure data is measured at  $M$  distinct detector positions  $\vec{r}_1 \dots \vec{r}_M$ , with coordinates  $\vec{r}_i = (x_i, y_i)$ . Then, the temporal dimension is discretely sampled at  $Q$  time points  $t_1 \dots t_Q$  with a sampling frequency of  $f_s$  resulting in a time vector  $\vec{t} = (t_1, \dots, t_Q)^T$ . Spatial and temporal discretization enable the definition of  $p(\vec{r}_i, \vec{t}) = p_i(\vec{t})$ , the discrete pressure values reaching a transducer at position  $\vec{r}_i$ . Thereby, the pressure value detected by a transducer located at  $\vec{r}_i$  at time-point  $t_j$  is denoted by

$$p(\vec{r}_i, t_j) = p_{i,j}. \quad (4.7)$$

The temporal derivative of a pressure signal at position  $\vec{r}_i$  is taken numerically by subtracting adjacent pressure values and dividing them by the inverse of the sampling frequency

$$\frac{\partial}{\partial t} p_{i,j} \approx \frac{p_{i,j} - p_{i,j-1}}{1/f_s}. \quad (4.8)$$

Thereby,  $\frac{\partial}{\partial t} p_{i,1} \equiv 0$  for all detector positions. Equation 4.8 defines a set of discrete pressure derivative vectors  $\frac{\partial}{\partial t} p_i(\vec{t})$ .

In two-dimensional optoacoustics the surface integral in equation 4.6 simplifies to a line integral. Now, in the case where all detectors are positioned along a circle, the line integral reduces to a discrete summation over all transducer positions  $\vec{r}_i$ ,

$$H(x, y) = \sum_{i=1}^M \left[ 2p_i(\vec{t}) - 2\vec{t} \frac{\partial}{\partial t} p_i(\vec{t}) \right]_{t_j = \sqrt{(x-x_i)^2 + (y-y_i)^2} / c_s}. \quad (4.9)$$

In general, no time instant  $t_j \in \vec{t}$  will fulfill the constraint  $t_j = \sqrt{(x-x_i)^2 + (y-y_i)^2} / c_s$  in the above summation. Therefore, simple rounding will define the time instant  $t_j$  closest to meeting the constraint.

Initially, analytical inversion formulas dominated image reconstruction in most optoacoustic systems. Their simplicity and low memory requirements, as shown above, made implementation easy and led to very fast reconstruction times. Nowadays, parallelization on graphics processing units (GPU) enables ultra-fast volumetric reconstructions of large datasets [78].

### 4.1.2 Frequency Domain Algorithms

Optoacoustic image reconstruction algorithms in the frequency domain transfer the inversion problem, originally stated in temporal and spatial variables (2.53 – 2.55), to the frequency domain. Taking advantage of Fourier techniques such as the Fast Fourier Transform (FFT) algorithm, the algorithms efficiently solve the inversion problem in the frequency domain and back-transform the solution into the spatial domain. Algorithms have been suggested for all important detection geometries, namely planar [29],[31], cylindrical [30],[32] and spherical [32] geometry.

Before deriving a reconstruction algorithm, the solution to the wave equation Cauchy problem is transferred to the frequency domain. As demonstrated in chapter 2, the optoacoustic effect, generated by an electromagnetic energy Dirac-pulse, can be modeled by the optoacoustic wave equation 2.50. Under the assumptions made in section 2.2.2, the wave equation in 2.50 can be equivalently reformulated as the wave equation Cauchy problem (2.53 – 2.55). Then, the time domain solution has been found with a Green's function approach, where the Green's function  $g(\vec{r}, t)$  satisfies

$$\frac{\partial^2}{\partial t^2} g(\vec{r}, t) - c_s^2 \nabla^2 g(\vec{r}, t) = \delta(\vec{r} - \vec{r}') \delta(t - t') \quad (4.10)$$

$$g(\vec{r}, 0) = 0, \quad (4.11)$$

$$\frac{\partial}{\partial t} g(\vec{r}, 0) = 0, \quad (4.12)$$

the wave equation Cauchy problem with a Dirac-source term at position  $\vec{r}'$  and time instant  $t'$ . Now, transferring equation 4.10 to the frequency domain, a three-dimensional

Fourier-transformation with respect to  $\vec{r}$  and a one-dimensional Fourier transformation with respect to  $t$  is performed, yielding

$$-\omega^2 \tilde{G}(\vec{k}, \omega) + c_s^2 k^2 \tilde{G}(\vec{k}, \omega) = \exp(-i\omega t') \exp(-i\vec{r}' \cdot \vec{k}), \quad (4.13)$$

where  $\vec{k} = (k_x, k_y, k_z)^T$  denotes the three-dimensional wavenumber vector with norm  $k := \|\vec{k}\| = \sqrt{k_x^2 + k_y^2 + k_z^2}$ . Now, by algebraically solving for  $\tilde{G}$  and applying a four-dimensional inverse Fourier transform, the Green's function  $g$  in the time domain can be (up to a constant) easily expressed as

$$g(\vec{r}, t; \vec{r}', t') = \frac{1}{(2\pi)^4} \iiint_{\mathbb{R}^3} \int_{-\infty}^{\infty} \frac{\exp(i\omega(t-t')) \exp(i\vec{k} \cdot (\vec{r} - \vec{r}'))}{k^2 - (\omega/c_s)^2} d\omega d\vec{k}. \quad (4.14)$$

In equation 2.68, the Green's function is expressed as a spherical wave, whereas above equation 4.14 is a representation by means of a sum of plane waves with direction  $\vec{k}$  and frequency  $\omega$ . When solving the integrals in equation 4.14 one can first consider the inner integral with respect to  $\omega$  for  $t' = 0$

$$\int_{-\infty}^{\infty} \frac{\exp(i\omega t) \exp(i\vec{k} \cdot (\vec{r} - \vec{r}'))}{k^2 - (\omega/c_s)^2} d\omega, \quad (4.15)$$

which has two singularities at  $\omega = \pm c_s k$ . Applying Cauchy's residue theorem [82] one can solve the above inner integral and inserting the result in 4.14 gives a new expression for the Green's function with a source term at  $t' = 0$

$$g(\vec{r}, t; \vec{r}') = \frac{c_s}{(2\pi)^3} \iiint_{\mathbb{R}^3} \frac{\sin(c_s k t)}{k} \exp(i\vec{k} \cdot (\vec{r} - \vec{r}')) d\vec{k}. \quad (4.16)$$

Referring to equation 2.70, the forward solution of the optoacoustic wave equation Cauchy problem can be expressed as

$$p(\vec{r}, t) = \Gamma H_r(\vec{r}) \frac{\partial}{\partial t} \delta(t) * g(\vec{r}, t) \quad (4.17)$$

$$= \int_{-\infty}^{\infty} \iiint_{\mathbb{R}^3} \Gamma H_r(\vec{r}') \frac{\partial \delta(t')}{\partial t'} g(\vec{r}, t; \vec{r}', t') d\vec{r}' dt' \quad (4.18)$$

$$= \Gamma \iiint_{\mathbb{R}^3} H_r(\vec{r}') \frac{\partial}{\partial t} g(\vec{r}, t; \vec{r}') d\vec{r}'. \quad (4.19)$$

Thereby, the above rationale takes advantage of the following properties

- $\int \frac{\partial \delta(t-t_0)}{\partial t} f(t) dt = -f'(t_0)$ ,
- $\frac{\partial}{\partial t} g(\vec{r}, t; \vec{r}', t') = -\frac{\partial}{\partial t'} g(\vec{r}, t; \vec{r}', t')$ .

Inserting 4.16 into 4.19 leads to

$$p(\vec{r}, t) = \Gamma \frac{c_s^2}{(2\pi)^3} \iiint_{\mathbb{R}^3} \iiint_{\mathbb{R}^3} H_r(\vec{r}') \cos(c_s k t) \exp(i\vec{k} \cdot (\vec{r} - \vec{r}')) d\vec{k} d\vec{r}'. \quad (4.20)$$

By closely looking at equation 4.20, one can separate the calculation of pressure  $p(\vec{r}, t)$  into two parts.

1. 3D Fourier transform  $\tilde{H}_r(\vec{k})$  of the initial pressure

$$\tilde{H}_r(\vec{k}) = \Gamma c_s^2 \iiint_{\mathbb{R}^3} H_r(\vec{r}') \exp(-i\vec{k} \cdot \vec{r}') d\vec{r}'. \quad (4.21)$$

2. Propagation of the initial pressure to time point  $t$  and 3D inverse Fourier transform

$$p(\vec{r}, t) = \frac{1}{(2\pi)^3} \iiint_{\mathbb{R}^3} \tilde{H}_r(\vec{k}) \cos(c_s k t) \exp(i\vec{k} \cdot \vec{r}) d\vec{k}. \quad (4.22)$$

The two steps 4.21 and 4.22 can be realized computationally very fast and effective with the FFT algorithm and are at the basis of the freely available optoacoustic simulation toolbox *k-Wave*, [83].

Now, considering optoacoustic imaging in three dimensions, the reconstruction problem can be characterized as follows. The pressure function  $p(\vec{r}, t)$  may be written as a sum of separable product functions

$$p(\vec{r}, t) = \sum_j \alpha_j s_{1,j}(r_1) s_{2,j}(r_2) s_{3,j}(r_3) s_{4,j}(t), \quad (4.23)$$

where  $\vec{r} = (r_1, r_2, r_3)^T$  are the three spatial variables, which depend on the geometry of the imaging problem, and  $\alpha_j$  is a scalar defining the contribution of the  $j$ -th base function. The infinite sum over  $j$  in equation 4.23 has to be understood symbolically and may also represent an integration over a continuous parameter as in the case of a Fourier transform. The image one tries to recover, corresponds to the pressure distribution  $p(\vec{r}, t)$  upon laser excitation at time point  $t = 0$ . Expressing it by means of the same spatial expansion functions, it can be written in 3D space as

$$p(\vec{r}, 0) = \sum_j \beta_j s_{1,j}(r_1) s_{2,j}(r_2) s_{3,j}(r_3). \quad (4.24)$$

Likewise, equation 4.23 can be evaluated at time point  $t = 0$

$$p(\vec{r}, 0) = \sum_j \alpha_j s_{1,j}(r_1) s_{2,j}(r_2) s_{3,j}(r_3) s_{4,j}(0), \quad (4.25)$$

with  $\beta_j$  as scalar coefficients defining the contribution of the spatial base functions. Comparing equation 4.24 and equation 4.25 requires the coefficients to correspond to

$$\beta_j = \alpha_j s_{4,j}(0) \quad \forall j, \quad (4.26)$$

a unique dependence referred to as dispersion relation.

Optoacoustic measurements are obtained via detectors commonly positioned on a possibly infinite plane, an infinite cylinder or a sphere enclosing the ROI. In mathematical terms this means that pressure data is obtained on a two-dimensional manifold (plane, cylinder, sphere) in three-dimensional euclidean space  $\mathbb{R}^3$ . Using the above representation of the pressure function, the set of measurements  $p(\vec{r}, t)$  can be expressed as

$$p(r_1, r_2, r_3 = C, t) = \sum_j \alpha_j s_{1,j}(r_1) s_{2,j}(r_2) s_{3,j}(C) s_{4,j}(t), \quad (4.27)$$

where the two spatial degrees of freedom of the measurement boundary are  $r_1$  and  $r_2$ . Without loss of generality the manifold where the detectors are positioned, can be expressed by the constant  $r_3 = C$ . Now, optoacoustic image reconstruction consists of calculating  $p(r_1, r_2, r_3, t = 0)$  with the input data being  $p(r_1, r_2, r_3 = C, t)$ . Considering the four-dimensional space consisting of three spatial and one temporal dimension, knowing  $p(\vec{r}, t)$  entirely over two spatial and the temporal variable (through optoacoustic measurements) one tries to calculate  $p(\vec{r}, t)$  over the three spatial variables at just the single time point  $t = 0$ . Finally the identity  $p(\vec{r}, 0) = H_r(\vec{r})$  yields the image one tries to reconstruct.

As shown in the beginning of this section, a solution of the wave equation Cauchy problem can be decomposed into a set of planar waves by means of a 3D Fourier transformation (see 4.14). The representation of an optoacoustic pressure function by means of planar waves corresponds to a planar detection geometry. Accordingly, cylindrical or spherical detection geometries demand a representation of the pressure by cylindrical or spherical waves. However, the application of cylindrical or spherical waves leads to a complicated mathematical formulation of the inversion problem. In contrast to that, as shown above, a planar geometry benefits from its simple mathematical formulation via Fourier transforms, which can be realized numerically efficient with the FFT algorithm. Therefore, in the following, the deduction of a frequency domain reconstruction algorithm is merely shown for planar detection geometry. The rationale is based on [83].

Without loss of generality, it is assumed that the detection plane is positioned at  $z = 0$ , and that  $\vec{r} = (r_1, r_2, r_3)^T = (x, y, z)^T$  holds. The solution of the wave equation Cauchy problem  $p(\vec{r}, t)$  can be decomposed into a set of separable functions, as introduced in 4.22,

$$p(\vec{r}, t) = \frac{1}{(2\pi)^3} \int_{-\infty}^{\infty} \int_{-\infty}^{\infty} \int_{-\infty}^{\infty} \tilde{H}_r(k_x, k_y, k_z) \cos(c_s kt) e^{i(k_x x + k_y y + k_z z)} dk_x dk_y dk_z. \quad (4.28)$$

In order to simplify the following rationale, above pressure function is symmetrically extended for negative time points,  $p(\vec{r}, -t) = p(\vec{r}, t)$ . Then, the pressure measurements on the plane  $z = 0$  are denoted by  $M(x, y, t)$  and its Fourier transform by  $\tilde{M}(k_x, k_y, \omega)$ ,

$$M(x, y, t) = \frac{1}{(2\pi)^3} \int_{-\infty}^{\infty} \int_{-\infty}^{\infty} \int_{-\infty}^{\infty} \tilde{M}(k_x, k_y, \omega) e^{i(k_x x + k_y y + \omega t)} dk_x dk_y d\omega. \quad (4.29)$$

By definition,  $M(x, y, t)$  is symmetric in  $t$  and real. Therefore, also  $\tilde{M}(k_x, k_y, \omega)$  is symmetric in  $\omega$  leading to

$$M(x, y, t) = \frac{1}{(2\pi)^3} \int_0^\infty \int_{-\infty}^\infty \int_{-\infty}^\infty 2\tilde{M}(k_x, k_y, \omega) \cos(\omega t) e^{i(k_x x + k_y y)} dk_x dk_y d\omega \quad (4.30)$$

as an alternative expression for the measurement function  $M$ . Now, as in equations 4.24 and 4.25, the pressure measured can also be expressed by setting  $z = 0$  in 4.28

$$M(x, y, t) = \frac{1}{(2\pi)^3} \int_{-\infty}^\infty \int_{-\infty}^\infty \int_{-\infty}^\infty \tilde{H}_r(k_x, k_y, k_z) \cos(c_s k t) e^{i(k_x x + k_y y)} dk_x dk_y dk_z. \quad (4.31)$$

Comparing equations 4.30 and 4.31 gives an expression for the dispersion relation

$$\omega = c_s k = c_s \sqrt{k_x^2 + k_y^2 + k_z^2} \quad (4.32)$$

and its differential

$$d\omega = c_s^2 \frac{k_z}{\omega} dk_z. \quad (4.33)$$

Then, by inserting the dispersion relation 4.32 and its differential 4.33 into equation 4.31 and comparing the result to equation 4.30 one gets

$$\tilde{H}_r \left( k_x, k_y, \sqrt{\left(\frac{\omega}{c_s}\right)^2 - k_x^2 - k_y^2} \right) + \tilde{H}_r \left( k_x, k_y, -\sqrt{\left(\frac{\omega}{c_s}\right)^2 - k_x^2 - k_y^2} \right) = \frac{2c_s^2 k_z}{\omega} \tilde{M}(k_x, k_y, \omega). \quad (4.34)$$

Equation 4.34 illustrates, that symmetric optoacoustic sources at  $H_r(x, y, z)$  and  $H_r(x, y, -z)$  generate identical pressure measurements on their symmetry plane  $z = 0$ . However, assuming a symmetric source with  $\tilde{H}_r(k_x, k_y, k_z) = \tilde{H}_r(k_x, k_y, -k_z)$ , formula 4.34 reduces to

$$\tilde{H}_r \left( k_x, k_y, \sqrt{\left(\frac{\omega}{c_s}\right)^2 - k_x^2 - k_y^2} \right) = \frac{c_s^2 k_z}{\omega} \tilde{M}(k_x, k_y, \omega). \quad (4.35)$$

In summary, a frequency domain reconstruction algorithm comprises of the following three steps.

1. Time-symmetry and Fourier transform of measurement data.

The optoacoustic measurements  $M(x, y, t)$  are symmetrically extended for  $t < 0$ ,

$$M(x, y, t) = p(x, y, z = 0, t) + p(x, y, z = 0, -t), \quad (4.36)$$

and its three-dimensional Fourier transform  $\tilde{M}(k_x, k_y, \omega)$  is calculated,

$$\tilde{M}(k_x, k_y, \omega) = \int_{-\infty}^\infty \int_{-\infty}^\infty \int_{-\infty}^\infty M(x, y, t) e^{-i(k_x x + k_y y + \omega t)} dx dy dt. \quad (4.37)$$

2. Image reconstruction in the frequency domain.

The Fourier transform  $\tilde{H}_r(k_x, k_y, k_z)$  is calculated via equation 4.35. Numerically, as only discrete values of  $\omega$  are given, interpolation techniques are needed, to obtain discrete values for  $k_z$ .

3. Inverse Fourier transform of image and positivity constraint.

The reconstructed image  $H_r(x, y, z)$  is calculated by an inverse Fourier transform

$$H_r(x, y, z) = \frac{1}{(2\pi)^3} \int_{-\infty}^{\infty} \int_{-\infty}^{\infty} \int_{-\infty}^{\infty} \tilde{H}_r(k_x, k_y, k_z) e^{i(k_x x + k_y y + k_z z)} dk_x dk_y dk_z. \quad (4.38)$$

As the reconstructed image will be symmetric with respect to  $z = 0$ , the negative part is omitted.

The interpolation method chosen in step two has a major effect on image quality. Some interpolation methods even require the application of regularization techniques to reconstruct an accurate image [84].

## 4.2 Algebraic Inversion Algorithms

Algebraic reconstruction techniques differ conceptually from analytic formulas as the inversion is performed numerically instead of analytically. Thereby, the solution of the optoacoustic wave equation Cauchy problem without constants

$$p(\vec{r}, t) = \frac{\partial}{\partial t} \oint_{|\vec{r} - \vec{r}'| = c_s t} \frac{H_r(\vec{r}')}{|\vec{r} - \vec{r}'|} dS(\vec{r}') \quad (4.39)$$

is discretized in space and time resulting in a matrix vector equation

$$\vec{p} = \mathcal{M} \cdot \vec{H}. \quad (4.40)$$

Here, vector  $\vec{p}$  represents the (measured) pressure data and vector  $\vec{H}$  stands for the spatially varying optical absorption coefficient defining the image. The two vectors are connected by the model matrix  $\mathcal{M}$ , incorporating measurement geometry and constants related to the optoacoustic effect. Reconstruction techniques relying on a model (matrix) for the forward problem which is subsequently inverted, are often referred to as *model-based algorithms*.

### 4.2.1 IMMI Algorithm

In the following section, a recent version of the 2010 suggested interpolated-matrix-model inversion (IMMI) algorithm [85] is presented. Starting point is the solution of the optoacoustic forward problem shown in 4.39. In three dimensions, the surface integral has to be solved over spherical shells. Assuming a source  $H_r(x, y, z)$  confined to the plane  $z = 0$ ,

$$H_r(x, y, z) = H_r(x, y) \delta(z), \quad (4.41)$$

reduces the surface integral in 4.39 to a line integral over concentric arcs. The restriction in equation 4.41, essentially defines a two-dimensional problem where both sources and detectors are located in a plane. As the derivation of the algorithm is less complex for the planar case, all concepts of the IMMI algorithm will be presented in two dimensions. However, all basic ideas translate analogously to the three-dimensional case. Therefore, for the rest of this section, all vectors are restricted to the xy-plane,  $\vec{r} = (x, y)^T$ . Then, the solution of the optoacoustic wave equation reads as

$$p(\vec{r}, t) = \frac{\partial}{\partial t} \oint_{|\vec{r}-\vec{r}'|=c_s t} \frac{H_r(\vec{r}')}{|\vec{r}-\vec{r}'|} dl(\vec{r}'). \quad (4.42)$$

In order to discretize equation 4.42, first, temporal and spatial domain have to be discretized. Therefore, a time vector with  $Q$  equidistant time points is defined,  $\vec{t} = (t_1, \dots, t_Q)^T$ , where the sampling frequency is given as  $f_S = 1/(t_2 - t_1)$ . The spatial domain is discretely represented by a set of pixels, defined by the x- and y-coordinates of their center. The pixel size in each dimension is denoted by  $dx$  and  $dy$ . For simplicity, a square pixel grid centered in the xy-plane and  $n$  pixels in each dimension is assumed, resulting in a total of  $N = n^2$  image pixels with coordinates  $\vec{r}_1, \dots, \vec{r}_N$ .

The left hand side of equation 4.42 represents a pressure measurement of an optoacoustic point transducer positioned at  $\vec{r}$ . By sampling the pressure at the time points defined by the time vector  $\vec{t}$ , a pressure vector  $\vec{p}$  is defined. Then, a set of pressure measurements obtained by  $M$  transducers located at positions  $\vec{r}^1, \dots, \vec{r}^M$  defines  $M$  distinct pressure vectors. By lexicographically arranging them into a single pressure vector  $\vec{p}$ , the left hand side of equation 4.42 can be discretized for multiple measurements.

The right hand side of equation 4.42 can be essentially divided into a time derivative and a line integral along a circle,

$$p(\vec{r}, t) = \frac{\partial}{\partial t} \mathfrak{I}(t), \quad (4.43)$$

where

$$\mathfrak{I}(t) = \oint_{|\vec{r}-\vec{r}'|=c_s t} \frac{H_r(\vec{r}')}{|\vec{r}-\vec{r}'|} dl(\vec{r}'). \quad (4.44)$$

Then, by considering the discrete time points of time vector  $\vec{t}$ , the time derivative can be approximated by a difference quotient

$$\frac{\partial}{\partial t} \mathfrak{I}(t_j) \approx \frac{\mathfrak{I}(t_j + \delta t) - \mathfrak{I}(t_j - \delta t)}{2\delta t}, \quad (4.45)$$

defining a time derivative vector.  $\delta t$  denotes an incremental time step. The integral  $\mathfrak{I}$  itself has to be calculated along a circle with radii  $c_s t_j$  centered at  $\vec{r}$ . In practice, integration over a part of the circle line will be sufficient as optoacoustic sources will be confined to the ROI and be zero outside. In order to simplify the calculation of the integral, each circle is approximated by a set of  $L$  straight lines defined by  $L + 1$  points  $\vec{r}_{j,1}, \dots, \vec{r}_{j,L+1}$  distributed equidistantly on the circle line. The length of the lines is calculated for  $g = 1, \dots, L$  as

$$l_j = |\vec{r}_{j,g} - \vec{r}_{j,g+1}|. \quad (4.46)$$

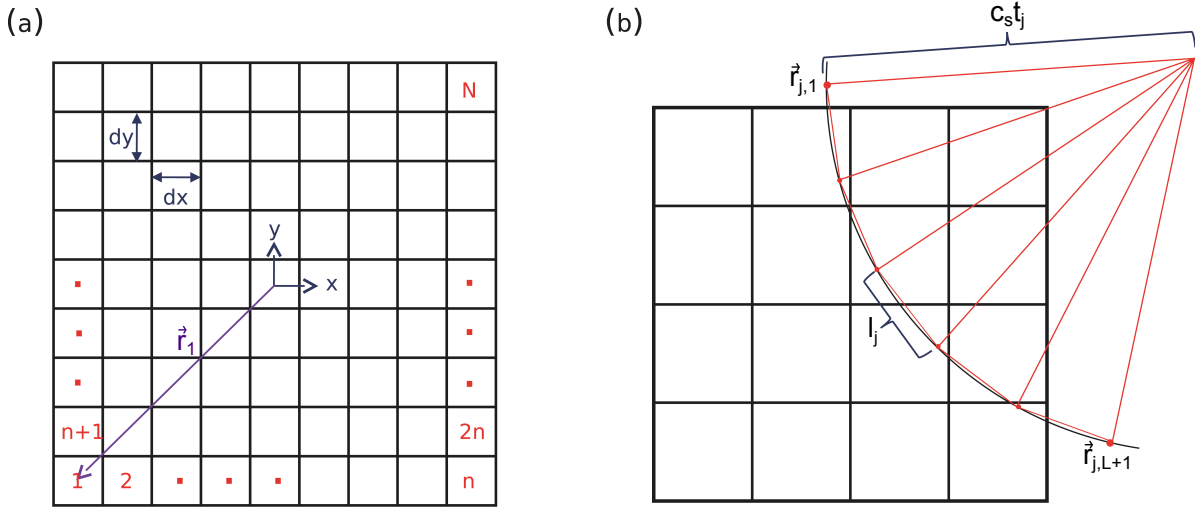


Figure 4.2: (a) Grid with  $N = n^2$  pixels. (b) Approximation of the detection arc by a set of straight lines.

On each of the lines the value of function  $H_r(\vec{r}')/(\vec{r} - \vec{r}')$  is estimated as the mean of the line end points,

$$H_r^{j,g} = \frac{1}{2} \left[ \frac{H_r(\vec{r}_{j,g})}{|\vec{r} - \vec{r}_{j,g}|} + \frac{H_r(\vec{r}_{j,g+1})}{|\vec{r} - \vec{r}_{j,g+1}|} \right]. \quad (4.47)$$

Then, the integral can be approximately expressed as

$$\mathfrak{J}(t_j) \approx l_j \sum_{g=1}^L H_r^{j,g}. \quad (4.48)$$

Now, in general, the auxiliary points  $\vec{r}_{j,g}$  on the circle line will not coincide with the pixel positions for which  $H_r$  has to be determined. Therefore, the function value for each circle point,  $H_r(\vec{r}_{j,g})$ , will be interpolated by pixel grid points. Several interpolation schemes have been implemented, with linear interpolation providing the best tradeoff between accuracy and calculation velocity [85],[86]. Accordingly, each circle point  $\vec{r}_{j,g} = \begin{pmatrix} x_{j,g} \\ y_{j,g} \end{pmatrix}$  lies on a square, limited by four adjacent pixels with coordinates  $\begin{pmatrix} x_1 \\ y_1 \end{pmatrix}$ ,  $\begin{pmatrix} x_2 \\ y_1 \end{pmatrix}$ ,  $\begin{pmatrix} x_2 \\ y_2 \end{pmatrix}$ ,  $\begin{pmatrix} x_1 \\ y_2 \end{pmatrix}$  as vertices (figure 4.3). Thereby,  $x_1 \leq x_{j,g} < x_2$  and  $y_1 \leq y_{j,g} < y_2$ . Then, the function value at a circle point can be written as

$$H_r(x_{j,g}, y_{j,g}) = \frac{1}{(x_2 - x_1)(y_2 - y_1)} \left[ H_r(x_1, y_1)(x_2 - x_{j,g})(y_2 - y_{j,g}) + \right. \\ \left. H_r(x_2, y_1)(x_{j,g} - x_1)(y_2 - y_{j,g}) + \right. \\ \left. H_r(x_2, y_2)(x_2 - x_{j,g})(y_{j,g} - y_1) + \right. \\ \left. H_r(x_1, y_2)(x_{j,g} - x_1)(y_{j,g} - y_1) \right]. \quad (4.49)$$

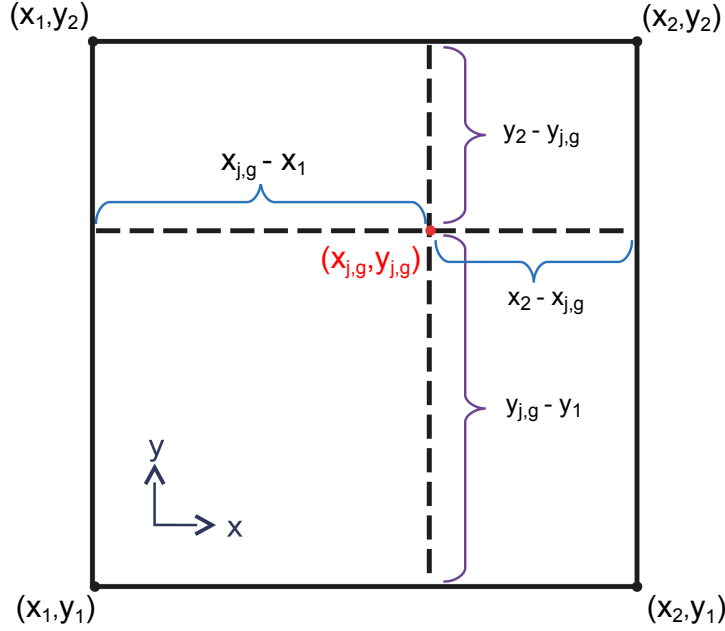


Figure 4.3: Bilinear interpolation of the point  $(x_{j,g}, y_{j,g})$  by four pixels.

Inserting 4.49 into 4.47, one can express  $H_r^{j,g}$  as a linear combination of the function values at the grid points  $\vec{r}_k$ ,

$$H_r^{j,g} = \sum_{k=1}^N \tilde{\lambda}_k H_r(\vec{r}_k). \quad (4.50)$$

Now, inserting equation 4.50 into equation 4.48 and grouping the terms, one obtains

$$\mathcal{J}(t_j) = \sum_{k=1}^N \lambda_k H_r(\vec{r}_k), \quad (4.51)$$

as an expression for the line integral at time instant  $t_j$ .  $\lambda_k$  depends on the interpolation method applied and the number of lines taken to approximate the circle line. Then, taking the time derivative and reordering the terms one can discretely express the pressure  $\vec{p}^i$  measured by a single point transducer positioned at  $\vec{r}^i$  as

$$p(\vec{r}^i, t_j) = \sum_{k=1}^N m_k^{i,j} H_r(\vec{r}_k). \quad (4.52)$$

By compactly arranging the coefficients  $m_k^{i,j}$  one obtains the matrix formulation of the optoacoustic forward problem

$$\vec{p}^i = \mathcal{M}^i \cdot \vec{H}, \quad (4.53)$$

where  $\vec{p}_j = p(\vec{r}^i, t_j)$ ,  $\mathcal{M}_{j,k}^i = m_k^{i,j}$  and  $\vec{H}_k = H_r(\vec{r}_k)$ . In case when a set of pressure measurements is considered, vector  $\vec{p}$  is defined as stated above.  $\mathcal{M}$  is obtained by stacking the matrices  $\mathcal{M}^i$  of each measurement position  $\vec{r}^i$ . Overall this results in

$$\vec{p} = \mathcal{M} \cdot \vec{H}. \quad (4.54)$$

Once equation 4.39 has been discretized to a matrix-vector equation 4.54, image reconstruction is reduced to numerically inverting equation 4.54. If  $\mathcal{M}$  is small enough, its inverse can be calculated in a decent amount of time. As, in general,  $\mathcal{M}$  will not be square, its Moore-Penrose-Pseudoinverse defined as

$$\mathcal{M}^\dagger = (\mathcal{M}^T \mathcal{M})^{-1} \mathcal{M}^T \quad (4.55)$$

has to be calculated. Reconstructing an image is then reduced to a simple matrix-vector multiplication,

$$\vec{H} = \mathcal{M}^\dagger \cdot \vec{p}, \quad (4.56)$$

which can effectively be performed in real-time. In case of very big system matrices  $\mathcal{M}$ , iterative reconstruction techniques are preferred [87]. These inversion algorithms aim at iteratively minimizing the residual

$$\vec{H} = \arg \min_{\vec{H}_{it}} \left\| \vec{p} - \mathcal{M} \cdot \vec{H}_{it} \right\|. \quad (4.57)$$

In cases where the inversion problem is badly conditioned, regularization techniques might be necessary to reconstruct a meaningful image. The most prominent regularization technique, Tikhonov-regularization, aims at minimizing the cost function

$$\vec{H} = \arg \min_{\vec{H}_{it}} \left\| \vec{p} - \mathcal{M} \cdot \vec{H}_{it} \right\| + \left\| \mathbb{T} \cdot \vec{H}_{it} \right\|, \quad (4.58)$$

where  $\mathbb{T}$  is denoted the Tikhonov matrix [88]. Commonly, if no further information about the equation system is known, the Tikhonov matrix  $\mathbb{T}$  is chosen to be the identity matrix which results in a new cost function

$$\vec{H} = \arg \min_{\vec{H}_{it}} \left\| \vec{p} - \mathcal{M} \cdot \vec{H}_{it} \right\| + \mathfrak{t} \left\| \vec{H}_{it} \right\|, \quad (4.59)$$

where the scalar regularization parameter  $\mathfrak{t}$  determines the amount of regularization of the penalty term in equation 4.59. Thereby, commonly used minimization algorithms such as the gradient descent or conjugate gradient methods are applied to find the optimal  $\vec{H}_{it}$ . The LSQR-algorithm [89] is a particularly efficient and fast algorithm, which has been especially designed for large and sparse matrices. In the above described time-domain optoacoustic model the resulting matrix  $\mathcal{M}$  is inherently sparse, as nonzero elements arise only due to the line integral, which affects merely a few pixels in proximity of the circle line. Furthermore, by applying a positivity constraint to the admissible iteration steps  $\vec{H}_{it}$ ,

negative values commonly appearing in reconstructions obtained from analytic inversion algorithms, can be circumvented,

$$\vec{H} = \arg \min_{\vec{H}_{it}, \|\vec{H}_{it}\| \geq 0} \left\| \vec{p} - \mathcal{M} \cdot \vec{H}_{it} \right\|. \quad (4.60)$$

The major advantage of model-based algorithms is that any linearizable physical effect, such as acoustic heterogeneities ([33],[90],[91],[92]) or detectors' spatial impulse responses ([36],[37],[39]) can be included in the model. In this way, a more complex and realistic model of the actual physical processes is generated, thus minimizing the discrepancies between measurements of the imaging system and signals predicted by the theoretical model.

A crucial step [93], defining the accuracy of the model and thus the quality of reconstructed images, is the choice of the technique applied to express the continuous function  $H_r$  by its values at discrete locations

$$H_r(\vec{r}) = \sum_{k=1}^N \lambda_k H_r(\vec{r}_k). \quad (4.61)$$

In case of the IMMI algorithm,  $\lambda_k$  represents previously defined interpolation functions. Interpolation techniques suggested include linear interpolation on rectangular triangles [85], bi- and trilinear [86] or higher-order interpolation. Apart from the presented IMMI algorithm, there are several other suggested models in the literature. The scope of imaging models includes cubic [87] or spherical [39] voxels as expansion functions  $\lambda_k$  as well as parabolic basis functions [94]. Recently, an imaging model using radially symmetric Kaiser-Bessel window functions has been suggested [95]. Kaiser-Bessel windows have been previously used as expansion functions in other tomographic imaging systems such X-ray CT [96].

### 4.3 Signal Recovery and Image Reconstruction in cw-Optoacoustics

Another way to generate a depth-resolved optoacoustic signal is to use amplitude-modulated electromagnetic excitation sources [45], [49], [47]. Thereby, as described in section 2.2.4, the cw-laser source is controlled by a function generator applying a linear frequency modulated (LFM) chirp resulting in a laser output (figure 4.4) of

$$l(t) = \mathcal{A} \operatorname{rect} \left( \frac{t}{\mathcal{T}} \right) \cos \left( 2\pi t \left( f_0 + \frac{k}{2} t \right) \right), \quad (4.62)$$

or in its complex notation

$$l(t) = \mathbf{R} \left[ \mathcal{A} \operatorname{rect} \left( \frac{t}{\mathcal{T}} \right) \exp \left( i 2\pi t \left( f_0 + \frac{k}{2} t \right) \right) \right], \quad (4.63)$$

where  $\mathbf{R}$  denotes the real part of a complex number. Here,  $\mathcal{A}$  denotes the peak laser

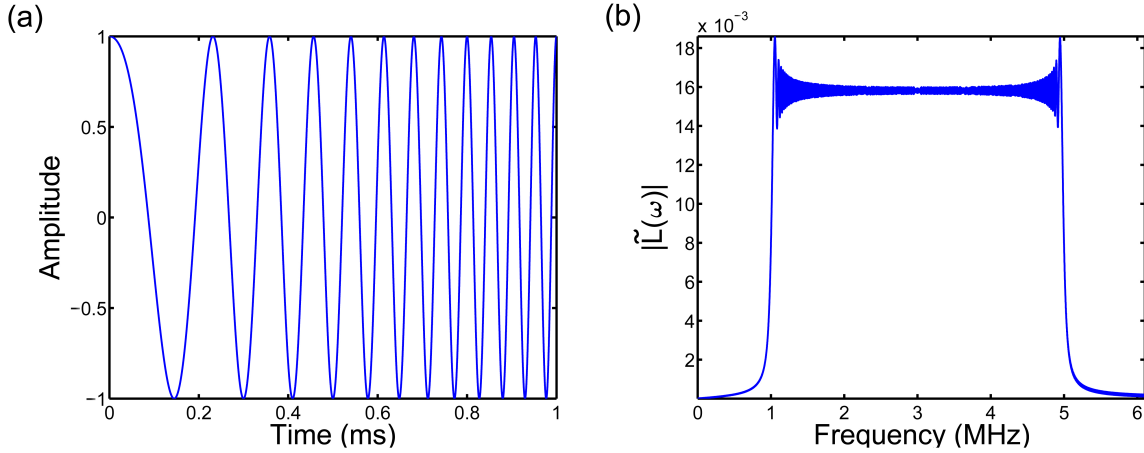


Figure 4.4: (a) LFM chirp  $l(t)$ . (b) Single-sided amplitude spectrum after Fourier transform of a LFM chirp  $l(t)$ .

intensity,  $f_0$  the initial frequency of the chirp and  $k$  the sweep rate. The sweep rate  $k$  is defined as in 2.76, where in this work only the plus sign, defining a positive chirp with increasing frequencies, is considered. After optical absorption and subsequent thermoelastic expansion within the ROI, a delayed LFM pressure signal 2.83 can be detected by a set of transducers positioned around the imaged object. As the strength of the optoacoustic effect depends on the first derivative of the temporal laser profile, signals generated with a cw-laser are much weaker as in the case of pulsed laser optoacoustic systems [49]. In effect, signals emitted by absorbers due to chirped excitation are hardly visible, being almost buried in noise. The technique presented herein to detect optoacoustic signals hidden in noise, is termed matched filter pulse compression, which is known to be the linear filter providing the maximum SNR [97]. Thereby, the impulse response  $h(t)$  of the filter has to satisfy the condition

$$h(t) = l(-t). \quad (4.64)$$

Considering a LFM chirp, as described in equation 4.62, the impulse response (without constants) becomes

$$h(t) = \text{rect}\left(\frac{t}{T}\right) \cos(\omega_0 t - \pi k t^2). \quad (4.65)$$

Then, according to the theory of linear time-invariant systems, the output of the filter,  $CC(t)$ , is calculated by convolving impulse response and signal,

$$CC(t) = (h * l)(t) = \int_{-\infty}^{\infty} h^*(\tau) l(t - \tau) d\tau = \frac{1}{2\pi} \int_{-\infty}^{\infty} \tilde{H}^*(\omega) \tilde{L}(\omega) \exp(i\omega t) d\omega, \quad (4.66)$$

and is termed *cross-correlation* function.  $\tilde{H}$  and  $\tilde{L}$  denote the temporal Fourier transform of  $h$  and  $l$ , respectively, and  $*$  represents the complex conjugate. Now, if the detected signal

was an exact replica of the excitation chirp 4.62, the output of the matched filter would be

$$CC(t) = \mathcal{A} \int_{-\mathcal{T}/2}^{\mathcal{T}/2} \cos(\omega_0\tau - \pi k\tau^2) \cos(\omega_0(t - \tau) + \pi k(t - \tau)^2) d\tau. \quad (4.67)$$

In the specific case, where the filter's impulse response is a time-reversed copy of the input signal, the output is termed *auto-correlation* function. The above integral can be solved analytically for a LFM chirp [98], which results in

$$\begin{aligned} CC(t) &= \mathcal{A}\mathcal{T} \Lambda\left(\frac{t}{\mathcal{T}}\right) \frac{\sin\left(\pi tk\mathcal{T}\Lambda\left(\frac{t}{\mathcal{T}}\right)\right)}{\pi tk\mathcal{T}\Lambda\left(\frac{t}{\mathcal{T}}\right)} \cos(\omega_0 t) \\ &= \mathcal{A}\mathcal{T} \Lambda\left(\frac{t}{\mathcal{T}}\right) \operatorname{sinc}\left(\pi tk\mathcal{T}\Lambda\left(\frac{t}{\mathcal{T}}\right)\right) \cos(\omega_0 t). \end{aligned} \quad (4.68)$$

In the above equation, the triangular function  $\Lambda$  is defined as

$$\Lambda(x) = \begin{cases} 1 - |x|, & |x| \leq 1, \\ 0, & |x| > 1, \end{cases} \quad (4.69)$$

and can be seen in figure 4.5. Correlation signal processing can be implemented in time-

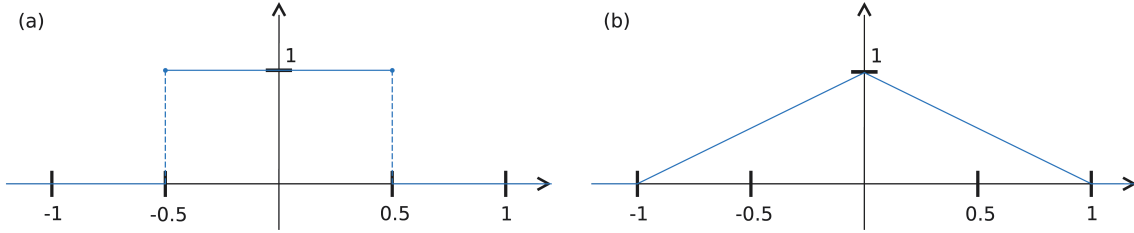


Figure 4.5: (a) Rectangular function. (b) Triangular function.

domain, however, the efficiency and speed of FFT-routines advocates an implementation in frequency-domain. As shown in section 2.2.4, the optoacoustically induced pressure upon laser excitation with a LFM chirp is a time-delayed LFM chirp with constant phase-shift  $\Phi_{th}$ . Specifically, the pressure detected by a point transducer positioned at  $\vec{r}$  will be

$$p(\vec{r}, t) = \mathcal{A}_p \cos\left(\omega(t) \left(t - \frac{|\vec{r} - \vec{r}_s|}{c_s}\right) + \Phi_{th}\right), \quad (4.70)$$

where  $\mathcal{A}_p$  denotes the amplitude and  $\omega(t) = \omega_0 + \pi kt$ . Taking the detected pressure  $p$  as the signal function and 4.64 as the matched filter impulse response yields a cross-correlation function  $CC(t)$ , which serves as the input data of an inversion algorithm,

$$CC(t) = \int_{-\infty}^{\infty} p^*(\vec{r}, \tau) l(t + \tau) d\tau. \quad (4.71)$$

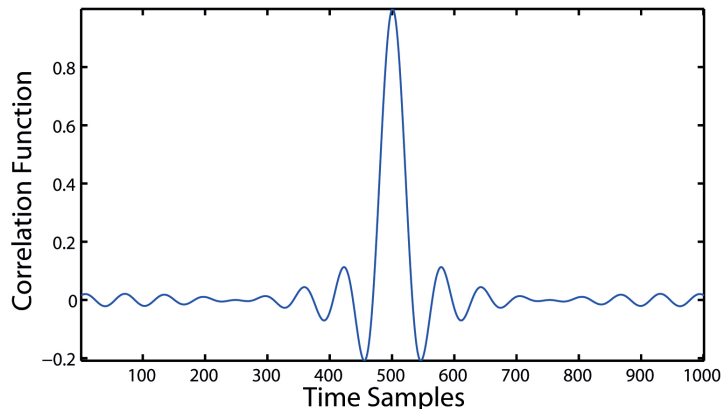


Figure 4.6: Cross-Correlation Function  $CC(t)$ .

As matched filter correlation processing optimizes the SNR of a measured signal, hardly visible optical absorbers will become visible in the time signal of the correlation function  $CC(t)$ . Finally, any time-domain inversion algorithm reconstructs an image of the ROI. Ideally, any point absorber lying within the ROI will be visible in the cross-correlation function by showing a distinct peak, as it can be seen in figure 4.6 for a noise-free case. The width of the peak determines the resolution of the imaging system and is mainly influenced by the width of the main lobe of the sinc-function in 4.68. The width of the main lobe in turn is determined by the first root of the sinc-function, which can be calculated as  $\approx \frac{1}{k\mathcal{T}} = \frac{1}{\mathcal{B}}$ , [98]. Therefore, by increasing the bandwidth  $\mathcal{B}$  of swept frequencies per chirp, a better resolution of the imaging system is expected.



# Chapter 5

## Incorporation of Geometric Detector Properties

The previous chapter 4 gave an overview of available reconstruction algorithms currently used in optoacoustic imaging. All of them have in common, that they assume the ultrasonic detector to be confined to a point  $\vec{r}$  in space, which stems from the mathematical modeling with the wave equation. Realistic ultrasonic transducers, however, have an extended surface, sometimes even combined with a focus (see section 3.2.2). In case of the predominant ultrasonic detectors based on piezoelectric materials, larger detection surfaces imply higher SNR. The discrepancy between theoretically assumed point-like transducers and realistic finite-size detectors is the source of severe imaging artifacts that hinder correct interpretation and quantification of optoacoustic reconstructions.

Model-based algorithms, as presented in section 4.2, offer the possibility to incorporate any linear physical effect of the imaging system. Therefore, geometric detector properties can readily be included into the forward model. In the following chapter, two concepts to incorporate geometric properties of an ultrasonic transducer into the model matrix of the IMMI algorithm are presented. After summarizing the theoretical rationale, the benefit of the two concepts is shown in simulations and experiments for two- and three-dimensional optoacoustic imaging systems.

### 5.1 Discretization by Points

The IMMI algorithm presented in 4.2.1, realizes a discretization of the forward solution of the optoacoustic wave equation Cauchy problem,

$$p(\vec{r}, t) = \frac{\partial}{\partial t} \oint_{|\vec{r}-\vec{r}'|=c_s t} \frac{H_r(\vec{r}')}{|\vec{r}-\vec{r}'|} dS(\vec{r}'), \quad (5.1)$$

into a matrix-vector equation

$$\vec{p} = \mathcal{M} \cdot \vec{H}. \quad (5.2)$$

Now, for a realistic transducer, where the detector cannot be assumed point-like, the acoustic pressure measured is spatially averaged on the active surface. Thereby, the signal detected by a transducer having a detection surface  $\mathcal{S}$  can be expressed as

$$p_{\mathcal{S}}(\vec{r}_c, t) = \oiint_{\mathcal{S}} p(\vec{r}', t) dS(\vec{r}'), \quad (5.3)$$

where  $\vec{r}_c$  denotes the center of the extended detector surface  $\mathcal{S}$ . In order to calculate the surface integral in 5.3, the transducer surface  $\mathcal{S}$  can be discretized by a set of  $n$  evenly distributed surface elements with central positions  $\vec{r}_i$ ,  $\mathcal{P}_n = \{\vec{r}_i\}_{i=1}^n \subset \mathcal{S}$ , and size  $\Delta_{\mathcal{S}, \vec{r}_i}$ . Thereby, equation 5.3 is approximated by

$$p_{\mathcal{S}}(\vec{r}_c, t) \approx \sum_{\vec{r}_i \in \mathcal{P}_n} p(\vec{r}_i, t) \Delta_{\mathcal{S}, \vec{r}_i}. \quad (5.4)$$

Then, for each of the  $n$  points, a point-model matrix  $\mathcal{M}_{\vec{r}_i}$  can be calculated. The effect of the entire surface  $\mathcal{S}$  is accordingly captured by a new model matrix  $\mathcal{M}_{sum}$ , generated as the sum of the individual point-model matrices,

$$\mathcal{M}_{sum} = \sum_{i=1}^n \mathcal{M}_{\vec{r}_i} \Delta_{\mathcal{S}, \vec{r}_i}. \quad (5.5)$$

If the size of the surface elements  $\Delta_{\mathcal{S}, \vec{r}_i}$  is constant, the term in the above equation can be dropped for simplicity. Overall, reconstructing optoacoustically generated pressure data  $\vec{p}_{\mathcal{S}}$ , measured with a finite-size detector, with a model-based algorithm, results in inverting the new matrix-vector equation

$$\vec{p}_{\mathcal{S}} = \mathcal{M}_{sum} \cdot \vec{H}. \quad (5.6)$$

## 5.2 Discretization by Lines

Previously, in section 3.2.4, it has been shown, that an ultrasonic transducer can be entirely described by its TIR  $h_{TIR}$ . Moreover, the TIR can be divided into the SIR describing the detectors geometry and the EIR modeling the material components and the entire electric transduction of the detector,

$$h_{TIR} = h_{SIR} *_{t} h_{EIR}. \quad (5.7)$$

For certain, regular geometries, a SIR can be calculated analytically. Rosenthal et al. presented the case of a line detector in a two-dimensional setting and integrated the solution into the IMMI algorithm [36]. Thereby, in order to obtain the SIR, equation 3.14 was solved analytically,

$$h_{SIR}(\vec{r}_c, \vec{r}', t) = \iiint_{\mathcal{S}} \frac{\delta\left(t - \frac{|\vec{r}_d - \vec{r}'|}{c_s}\right)}{4\pi|\vec{r}_d - \vec{r}'|} dS(\vec{r}_d). \quad (5.8)$$

Now, in two dimensions, any finite-size transducer is modeled as a line or can be approximated by a set of lines. Then, in three-dimensional OAT, also the three dimensions of the

ultrasonic detector's surface  $\mathcal{S}$  can be included in the model. In practice, high-resolution volumetric optoacoustic imaging is largely performed by cross sectional tomographic systems, which make use of cylindrically focused transducers to selectively collect signals originated in the imaging plane. Volumetric imaging is then achieved by translating the transducer in the elevational direction, [22].

A cylindrically focused detector surface  $\mathcal{S}$  can be approximated by a set of  $m$  lines centered at  $\vec{r}_i$ ,  $\mathcal{L}_m = \{\vec{r}_i\}_{i=1}^m \subset \mathcal{S}$ . For each of these lines, an analytical SIR  $h_{SIR}^{\vec{r}_i}$  can be calculated. Now, the effect due to the SIR of the entire surface  $\mathcal{S}$  can be approximated by summing up all the SIR of the lines,

$$h_{SIR} \approx \sum_{i=1}^m h_{SIR}^{\vec{r}_i}. \quad (5.9)$$

Finally, recalling equation 3.19, the effect of the SIR can also be incorporated into the IMMI algorithm model matrix. This results in an expression for the pressure  $p_{\mathcal{S}}$ , detected by a three-dimensional finite-size transducer,

$$p_{\mathcal{S}}(\vec{r}_c, t) = \frac{\Gamma}{4\pi} \iiint_{\mathbb{R}^3} |\vec{r}_c - \vec{r}'| h_{SIR}(\vec{r}_c, \vec{r}', t + \frac{|\vec{r}_c - \vec{r}'|}{c_s}) *_t \frac{\partial}{\partial t} \frac{\delta(t - \frac{|\vec{r}_c - \vec{r}'|}{c_s})}{|\vec{r}_c - \vec{r}'|} H_r(\vec{r}') d\vec{r}', \quad (5.10)$$

where  $*_t$  denotes the temporal convolution operator and  $\vec{r}_c$  the center of the detection surface  $\mathcal{S}$ . The temporal convolution in the above equation has been implemented with high numerical efficiency within the framework of the IMMI algorithm, resulting in a new model matrix  $\mathcal{M}_{SIR}$ . Now, model-based reconstruction of optoacoustically generated pressure data, measured with a finite-size detector, consists of inverting the new matrix-vector equation

$$\vec{p}_{\mathcal{S}} = \mathcal{M}_{SIR} \cdot \vec{H}. \quad (5.11)$$

### 5.3 Simulations in Two Dimensions

In order to examine the capabilities of the two models described in the previous sections, numerical simulations were employed. Thereby, an optical absorption distribution  $H_r(x, y)$  was assumed by a two-dimensional truncated paraboloid, positioned at  $(x_0, y_0)$  with radius  $r_0$ , i.e.,

$$H_r(x, y) = \begin{cases} 1 - \frac{(x-x_0)^2 + (y-y_0)^2}{r_0^2}, & (x-x_0)^2 + (y-y_0)^2 \leq r_0^2, \\ 0, & (x-x_0)^2 + (y-y_0)^2 > r_0^2. \end{cases} \quad (5.12)$$

For this absorption pattern, the laser-induced pressure wave detected at a point in space can be calculated analytically (see appendix A.1.1). Then, the surface of a finite-size detector was discretized uniformly and very densely with  $>100$  equidistant points, and the analytical signals corresponding to each point were summed by equation 5.4 to determine the response of the entire detector area. Henceforth, the signals calculated in this manner, are referred to as the *analytical signals*.

### 5.3.1 Line Transducer

In the first simulation, a 1 cm line transducer was considered as a detector. In order to assess the accuracy of the models, the analytical signals were compared to the ones estimated by the two models introduced in section 5.1 and 5.2. For this purpose, the pressure vector predicted by the models was calculated from the matrices  $\mathcal{M}_{sum}$  and  $\mathcal{M}_{SIR}$  using equations 5.6 and 5.11. The discrete ROI considered, consists of  $201 \times 201$  pixels, equivalent to  $2 \times 2 \text{ cm}^2$ , resulting in a uniform resolution of about  $100 \mu\text{m}$ . The optical absorption distribution contained four different absorber sizes with radii of  $r_0 = 200 \mu\text{m}$ ,  $r_0 = 500 \mu\text{m}$ ,  $r_0 = 1 \text{ mm}$  and  $r_0 = 2 \text{ mm}$ , see figure 5.3 (a).

The signals shown in figure 5.1 (a) correspond to a single transducer, positioned at  $(x,y) = (4 \text{ cm}, 0 \text{ cm})$ . Both models replicate almost identical copies of the analytical signals. For all other positions on a detector ring with radius 4 cm, analytical signals and signals predicted by the models match equally. As absorbers with different sizes emit pressure waves at different frequencies, it is important that the whole frequency spectrum of broadband signals is accurately calculated. Therefore, the Fourier transforms of the signals were compared (figure 5.1 (b)) and proved good accuracy of the two models throughout the frequency spectrum.

Then, in a second step, the analytical signals were calculated for a tomographic geometry (figure 5.2). For this purpose, a 1 cm line transducer was scanned along a circumference surrounding the object with a  $2^\circ$  step so that 180 transducer positions are taken. In order to show the effects in absorbers of different sizes, the same absorption distribution as in the previous paragraph, corresponding to absorbers with radii of  $r_0 = 200 \mu\text{m}$ ,  $r_0 = 500 \mu\text{m}$ ,  $r_0 = 1 \text{ mm}$  and  $r_0 = 2 \text{ mm}$ , was considered. Model inversion was performed iteratively by means of the LSQR algorithm [89], with a preset tolerance as a stopping criterion.

When inverting model matrix  $\mathcal{M}$ , representing a point detector, severe image artifacts can be observed (figure 5.3 (b)). Specifically, smaller absorbers get considerably damped in its absorption coefficient. Furthermore, the more off the rotation axis of the detection circumference an absorber lies, the more smeared it will appear in the reconstruction. This is due to the discrepancy between signals detected by a line transducer and the model assuming a point detector. A point transducer positioned at  $\vec{r}_{det}$ , will only register a pressure wave emitted by a point absorber, positioned at  $\vec{r}_{abs}$ , at the time instant  $t = |\vec{r}_{det} - \vec{r}_{abs}|/c_s$ . Compared to that, a line transducer will receive signals from absorbers off the rotation axis for a longer amount of time. Moreover, the smearing effect visible in figure 5.3 (b) is frequency dependent. Smaller absorbers, emitting higher frequencies, get more severely affected than bigger absorbers, where the effect is hardly visible. However, by including geometric detector properties into the model, image distortions can be corrected. As expected from the analysis performed above, both models,  $\mathcal{M}_{sum}$  and  $\mathcal{M}_{SIR}$ , achieve equally good results (5.3 (c) and (d)).

In case of the point model, the 1 cm line of the transducer was approximated by 21 points. The number of points is a key factor in the evaluation of the two models. Calculation time  $\mathcal{T}_{sum}$  of the model matrix  $\mathcal{M}_{sum}$  scales linearly with the number of points  $n$  applied to

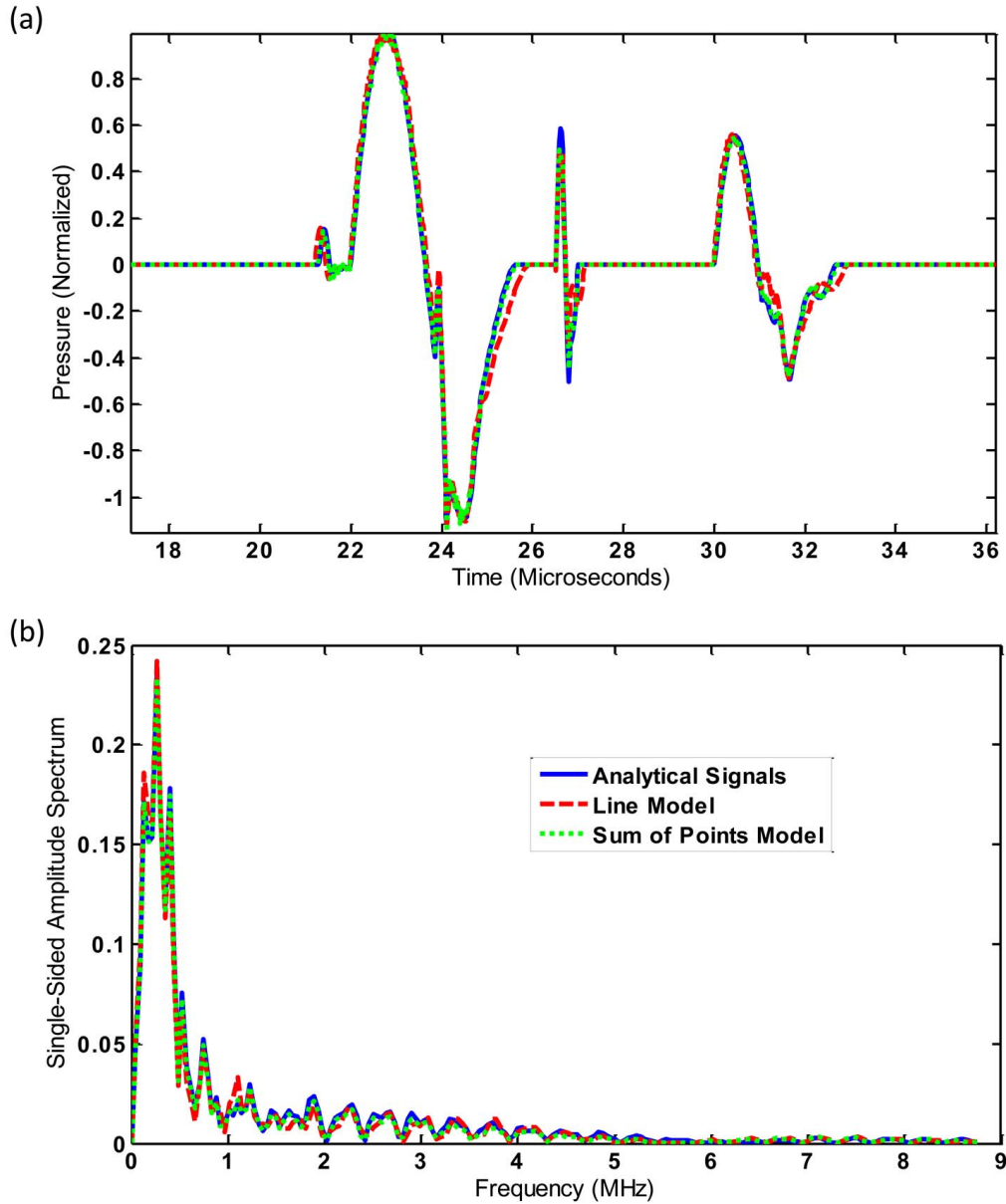


Figure 5.1: (a) Time-domain signal (blue) emitted by the two-dimensional absorption pattern shown in figure 5.3 (a) and the signals predicted by model matrices  $\mathcal{M}_{SIR}$  (red) and  $\mathcal{S}_{sum}$  (green). (b) Corresponding frequency-domain representation of the signals in (a).

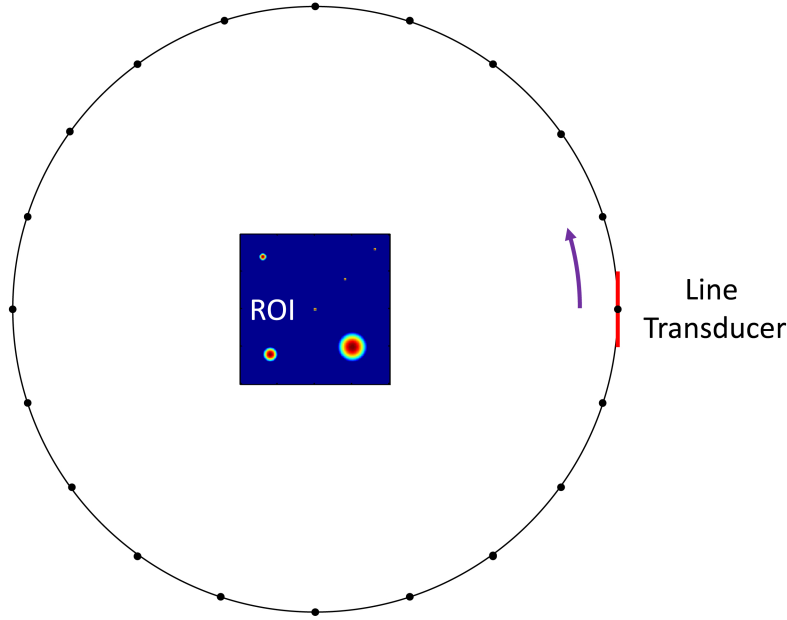


Figure 5.2: Tomographic detection geometry with a line transducer.

discretize the line,

$$\mathcal{T}_{sum} = n\mathcal{T}, \quad (5.13)$$

where  $\mathcal{T}$  denotes the time to calculate a single (point-detector) model matrix. The more points used to approximate the line, the more accurate the model will perform. However, after a threshold depending on the spatial resolution of the reconstruction, no further improvement in the model is observed. In contrast to that, calculation of the model matrix  $\mathcal{M}_{SIR}$  takes always the same amount of time  $\mathcal{T}_{SIR}$ . It consists of calculating a single model matrix  $\mathcal{M}$ , the SIR  $h_{SIR}$  (calculation time  $\mathcal{T}_{h_{SIR}}$ ) and the time  $\mathcal{T}_{conv}$  needed for temporal convolution,

$$\mathcal{T}_{SIR} = \mathcal{T} + \mathcal{T}_{h_{SIR}} + \mathcal{T}_{conv}. \quad (5.14)$$

Especially for long line transducers, where a lot of points would be needed to approximate the line, model matrix  $\mathcal{M}_{SIR}$  is preferable, as it can be calculated much quicker in this case than model matrix  $\mathcal{M}_{sum}$ . When holding the matrix in the computer memory, it must be noted, that, depending on the length of the detector line,  $\mathcal{M}_{sum}$  and  $\mathcal{M}_{SIR}$  occupy roughly up to ten times the memory as compared to the point detector model matrix  $\mathcal{M}$ . For the setting of the above simulations the memory requirements can be seen in table 5.1. However, at the expense of inversion speed, storing the matrix can be circumvented by only computing the action of the model matrix in each step of the iterative reconstruction.

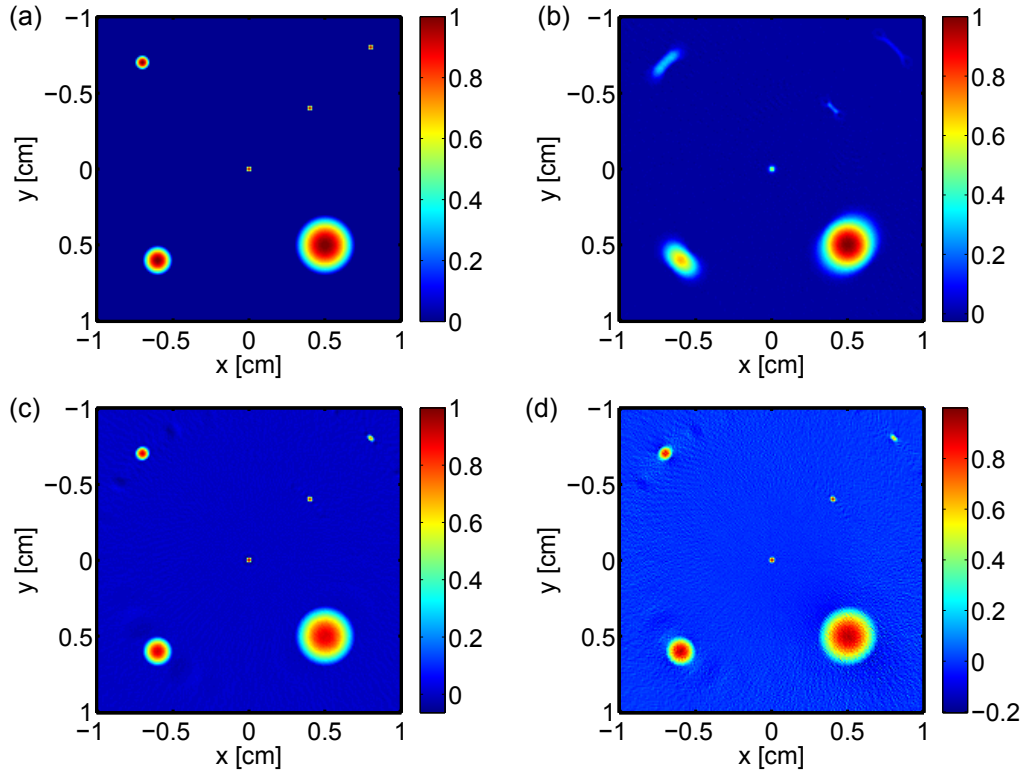


Figure 5.3: (a) Original image. (b) Model-based reconstruction assuming point detectors. (c) Reconstruction applying model matrix  $\mathcal{M}_{sum}$ . (d) Reconstruction applying model matrix  $\mathcal{M}_{SIR}$ .

Model Matrix	Memory [MB]
$\mathcal{M}$	700
$\mathcal{M}_{sum}$	5130
$\mathcal{M}_{SIR}$	6310

Table 5.1: Memory requirements for two-dimensional model matrices with  $n = 201$

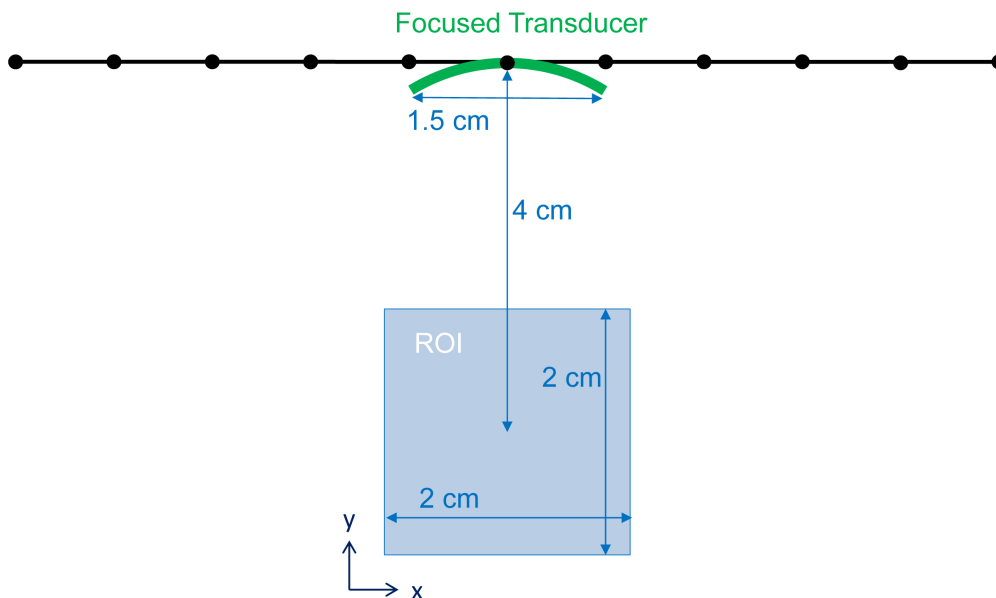


Figure 5.4: Two-dimensional geometry of line scan with a focused transducer.

### 5.3.2 Focused Transducer Scanning

In the following simulation a focused transducer was scanned along a line as depicted in figure 5.4. The transducer considered had a width of 1.5 cm and a radius of curvature of 4 cm. The scan was performed along a line of 8 cm length, taking optoacoustic measurements at 801 equally spaced detector positions. As an optical absorber a two-dimensional truncated paraboloid of radius  $r_0 = 1$  mm was placed at the center of the ROI which covered  $2 \times 2$  cm<sup>2</sup> and was discretized by  $101 \times 101$  pixels. The focused detector geometry was modeled by approximating the surface with 51 evenly distributed points. Then, as in the previous section, analytical signals were calculated by summing signals received at 151 surface positions representing 151 surface elements. Image reconstruction was performed by means of the IMMI algorithm. First, model matrix  $\mathcal{M}$ , representing point detectors was taken for inversion. Then, model matrix  $\mathcal{M}_{sum}$ , incorporating geometric detector properties was considered for image reconstruction.

The parabolic absorber placed in the center of the ROI can be seen in figure 5.5 (a), whereas the model-based reconstruction with matrix  $\mathcal{M}$  is depicted in sub-figure (b). Clearly, the absorber is smeared all over the ROI in x-direction losing all spatial resolution in that dimension. This results from the discrepancy between the assumed point detectors in the model and the actually recorded signals. Sub-figure 5.5 (c) shows the reconstruction obtained by inversion of model matrix  $\mathcal{M}_{sum}$ . A drastic improvement of the resolution in x-direction can be observed, closely approximating the actual size of the absorber. Due to inherently missing projection angles for a limited line scan, it is not expected that a reconstruction would perfectly match the original image, as the geometry only covers a limited view of the ROI.

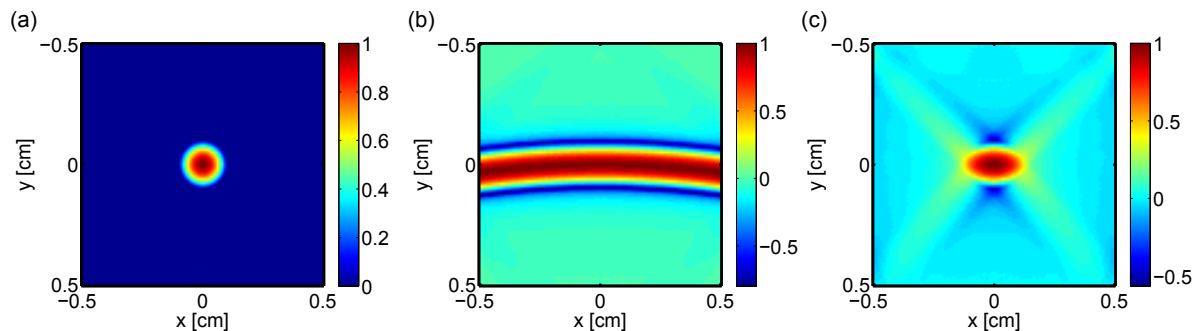


Figure 5.5: (a) One parabolic absorber placed in the center of the ROI. (b) Image reconstruction obtained with the IMMI algorithm assuming point detectors. (c) Model-based image reconstruction taking the detector geometry into account. All reconstructions show only the central part of the ROI.

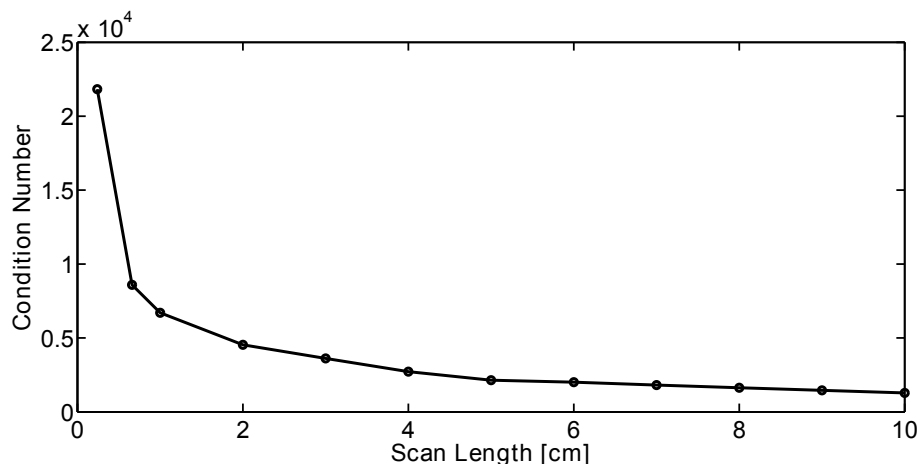


Figure 5.6: Condition number of the model matrix  $\mathcal{M}_{sum}$  for different scan lengths.

It should be noticed, that the improvement of the resolution in x-direction is strongly dependent on the length of the line scan. The longer the scan, the better conditioned the model matrix  $\mathcal{M}_{sum}$  became, therefore facilitating the model inversion. In order to corroborate this assertion, the condition number of the model matrix  $\mathcal{M}_{sum}$  has been calculated for different scan lengths. The results shown in figure 5.6 show a steady decrease of the condition number for increasing scan length, indicating a better conditioned inversion problem.

## 5.4 Simulations in Three Dimensions

As a physical phenomenon, the optoacoustic effect involves all three spatial dimensions and is most accurately modeled in three dimensions. This applies both to the optical absorption distribution as well as to the ultrasonic detection surfaces. Therefore, three-dimensional

model-based inversion techniques, incorporating the geometric detector properties, offer a holistic possibility to calculate quantitatively and qualitatively most comprehensive image reconstructions. In order to present the capabilities of model-based reconstruction algorithms in a noise-less setting, computer simulations were performed in a first step. To this end, again, optoacoustically excited pressure waves emitted by the optical absorption pattern of a three-dimensional truncated paraboloid, positioned at  $(x_0, y_0, z_0)$  with radius  $r_0$ ,

$$H_r(x, y, z) = \begin{cases} 1 - \frac{(x-x_0)^2 + (y-y_0)^2 + (z-z_0)^2}{r_0^2}, & (x-x_0)^2 + (y-y_0)^2 + (z-z_0)^2 \leq r_0^2, \\ 0, & (x-x_0)^2 + (y-y_0)^2 + (z-z_0)^2 > r_0^2, \end{cases} \quad (5.15)$$

are calculated analytically for the case of a point-like detector, as shown in appendix A.2.1. Then, optoacoustic pressure signals detected by a finite-size transducer with a three-dimensional detection surface  $\mathcal{S}$  can be approximated by discretizing the surfaces  $\mathcal{S}$  with more than 2000 equidistant points and summing the signals detected at each of the surface points. As in the previous section, the signals calculated by this procedure are referred to as the *analytical signals*.

#### 5.4.1 Cylindrically Focused Transducer

Widely-used cross sectional optoacoustic tomographic systems make use of cylindrically focused transducers to selectively collect signals originating in the imaging plane. Therefore, in this section, image reconstruction of optoacoustic data measured with cylindrically focused transducers is investigated. Specifically, the cylindrically focused transducer used in the imaging system introduced in section 3.4.1 is considered. It has a circular shape of 1.3 cm diameter and a focal length of 2.54 cm.

Then, the two model-based approaches presented in sections 5.1 and 5.2, capable of including geometric detector properties, are evaluated. Therefore, the transducer's detection surface  $\mathcal{S}$  is approximated by points as well as lines. In order to assess the accuracy of both models, the analytical signals are compared to the ones predicted by the two model matrices  $\mathcal{M}_{sum}$  and  $\mathcal{M}_{SIR}$ . For this purpose, the pressure vector is calculated from the two matrices using equations 5.6 and 5.11.  $\mathcal{M}_{SIR}$  is calculated by approximating the surface of the transducer with 21 lines, which can be seen in figure 5.7 (b). No significant changes in the signals are produced if a higher number of lines is used to approximate detection surface  $\mathcal{S}$ .  $\mathcal{M}_{sum}$  is calculated by considering 350 equally spaced points on the transducer surface, shown in figure 5.7 (a), so that the distance between the points for calculating  $\mathcal{M}_{sum}$  is approximately the same as the distance between the lines for calculating  $\mathcal{M}_{SIR}$ . The discrete ROI considered, consists of  $101 \times 101 \times 21$  voxels, equivalent to  $2 \times 2 \times 0.4$  cm<sup>3</sup>, resulting in a uniform resolution of 200  $\mu$ m. The detector receiving the optoacoustic signals is positioned at  $\vec{r} = (2.54 \text{ cm}, 0 \text{ cm}, 0 \text{ cm})$ . In order to cover a wide range of frequencies emitted by optical absorbers, first, four truncated paraboloids with radius  $r_0 = 200 \mu$ m and then with radius  $r_0 = 1 \text{ mm}$  are considered. The paraboloids are positioned along the positive x-axis in the middle plane at  $z = 0$ , starting at the center of the ROI

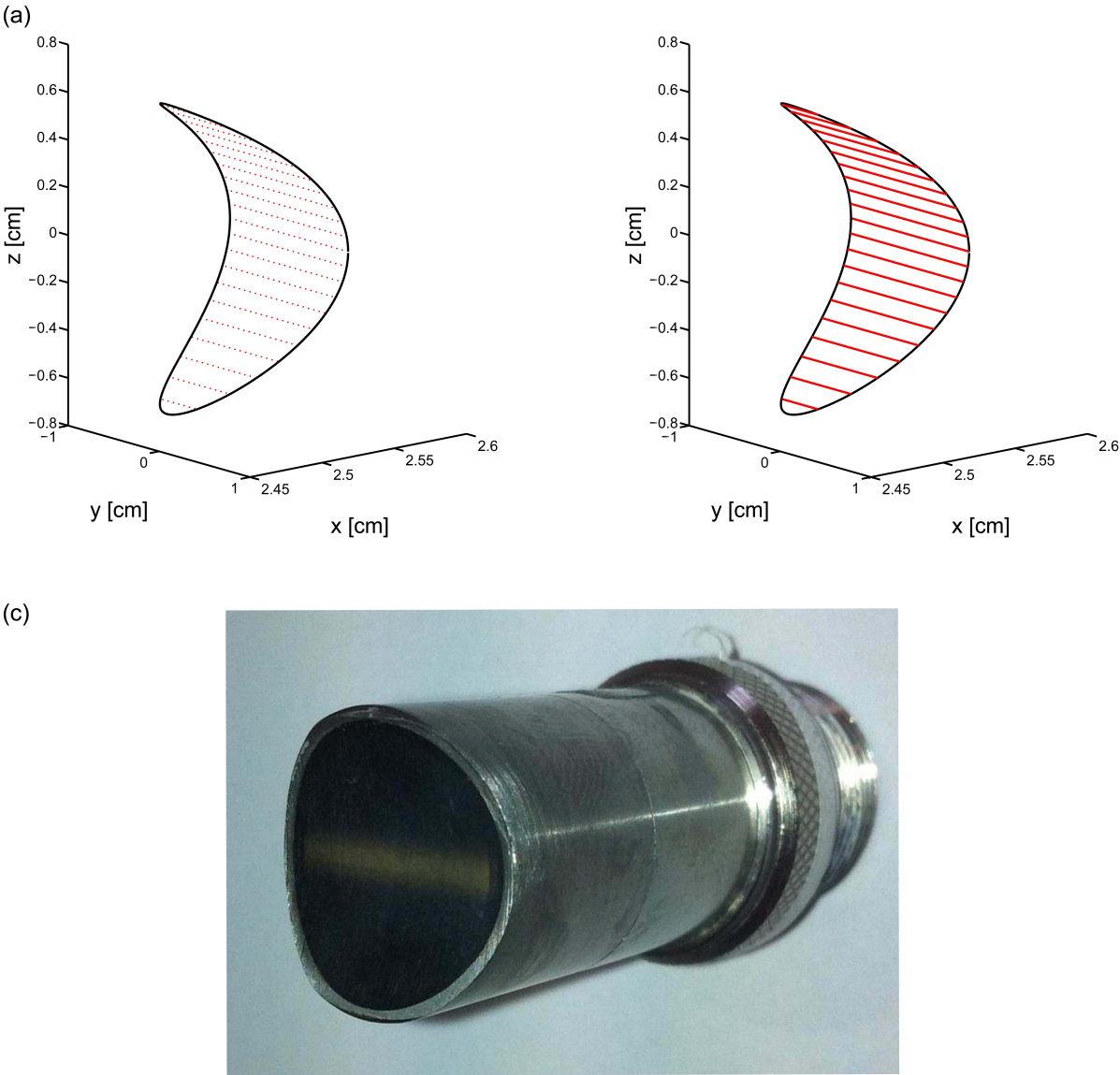


Figure 5.7: Approximation of a cylindrically focused transducer by (a) points and (b) lines. (c) Cylindrically focused transducer used in the imaging system described in 3.4.1.

as can be seen in figure 5.8 (a) and (d). The signals predicted by the two model matrices show good agreement with the analytical ones, ensuring that the models precisely capture the cylindrical detector surface. A comparison of the signals for one detector position is depicted in figure 5.8 (b) and (e). As absorbers with different sizes emit pressure waves at different frequencies, it is important that the whole frequency spectrum of broadband signals is accurately calculated. The Fourier transform of the signals, illustrated in figure 5.8 (c) and (f), showcases the good accuracy of the two models throughout the frequency spectrum. There is, however, a discrepancy between the analytical signals and the signals predicted by the models for the smaller absorbers. The reason for this difference is mainly due to fact, that the small absorbers are in the order of the pixel size. Therefore discretization errors are produced by approximating the actually continuous absorption distribution within the discrete ROI. Furthermore, to showcase the equivalent behavior of the two models, a stack of cross sectional images of a mouse is positioned inside the ROI and the signals predicted by the two matrices are compared. The central slice of the stack of images is depicted in figure 5.8 (g). Also here, figure 5.8 (h) and (i) corroborate, that the signals are almost identical, both in time and frequency domain. As the two models demonstrate the same behavior, only model matrix  $\mathcal{M}_{SIR}$  is considered for image reconstruction in the rest of the simulations and experiments, due to the lower computational time for wide detectors.

Thereupon, the analytical signals of four point absorbers with radius  $r_0 = 200 \mu\text{m}$  and radius  $r_0 = 1 \text{ mm}$  are calculated for a tomographic geometry. For this, a cylindrically focused transducer is considered to be scanned along a circumference surrounding the ROI with a  $2.25^\circ$  step, resulting in 160 projections per plane. Then, the detector is additionally scanned linearly along 0.6 cm in the elevational direction with a  $200 \mu\text{m}$  step size (31 steps), so that overall 4960 transducer positions are taken into account, which is shown in figure 5.9.

The inversion is performed using two alternative methods. First, a two-dimensional model matrix, capturing the 160 detector positions in one plane, is calculated. Thereby, each plane is reconstructed separately with this matrix. The inversion is done by means of the LSQR algorithm, resulting in a stack of 2D reconstructions representing the volumetric ROI. Here, no Tikhonov regularization needs to be employed, as the LSQR algorithm converges for full-view acquisition in the two-dimensional case, i.e., the optimal regularization parameter for Tikhonov regularization is  $t = 0$  in equation 4.59. Second, the full three-dimensional model matrix  $\mathcal{M}_{SIR}$ , incorporating the SIR of the transducer, is calculated. The inversion in this case is performed with the LSQR algorithm including standard Tikhonov regularization. Then, the results obtained by reducing the reconstruction problem to two dimensions can be compared with those obtained by a full three-dimensional reconstruction including the geometric shape of the transducer.

Figure 5.10 shows the results obtained by the two reconstruction procedures. The reconstruction achieved by inverting a 2D model for each plane, shows the expected smearing in the imaging plane of the absorbers located away from the center of the image. These in-plane artifacts can be seen in figure 5.10 (b) and (h) and are due to the assumed point transducers in the model which do not correspond to the actual signals collected by the

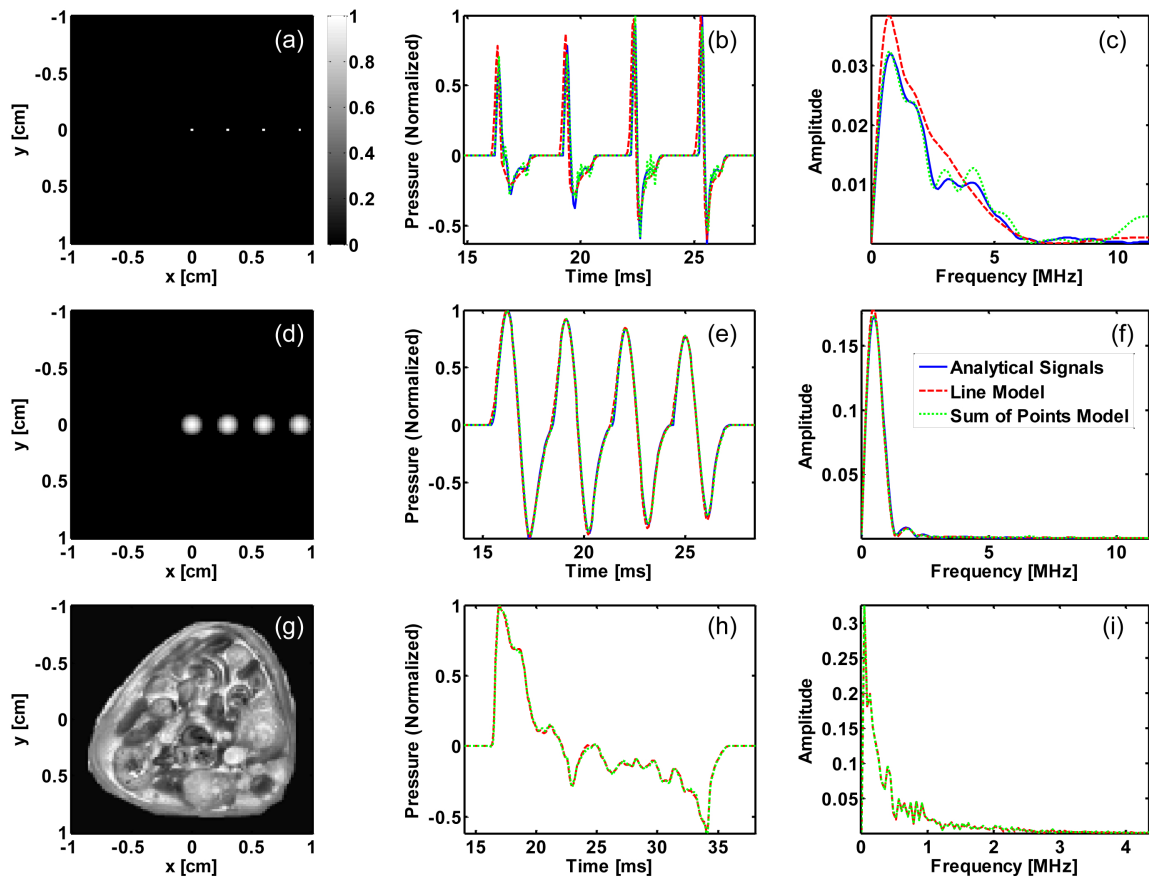


Figure 5.8: Comparison of pressure signals emitted by four absorbers of different size. (a) and (d) show the middle plane of the three-dimensional ROI with four parabolic absorbers of radius  $200 \mu\text{m}$  and  $1 \text{ mm}$  placed along the positive  $x$ -axis. (b) and (e) depict the signals predicted by the model matrices  $\mathcal{M}_{SIR}$  (dashed red) and  $\mathcal{M}_{sum}$  (dotted green) together with the analytical signals (blue) for a cylindrically focused transducer positioned at  $(x,y,z) = (2.54 \text{ cm}, 0 \text{ cm}, 0 \text{ cm})$ . (c) and (f) display the Fourier transforms of the signals in (b) and (e), respectively. (g) Middle plane of a stack of cross-sectional images of a mouse. (h) and (i) show the signals emitted by the mouse cross-sections predicted by the two matrices and their Fourier transforms.

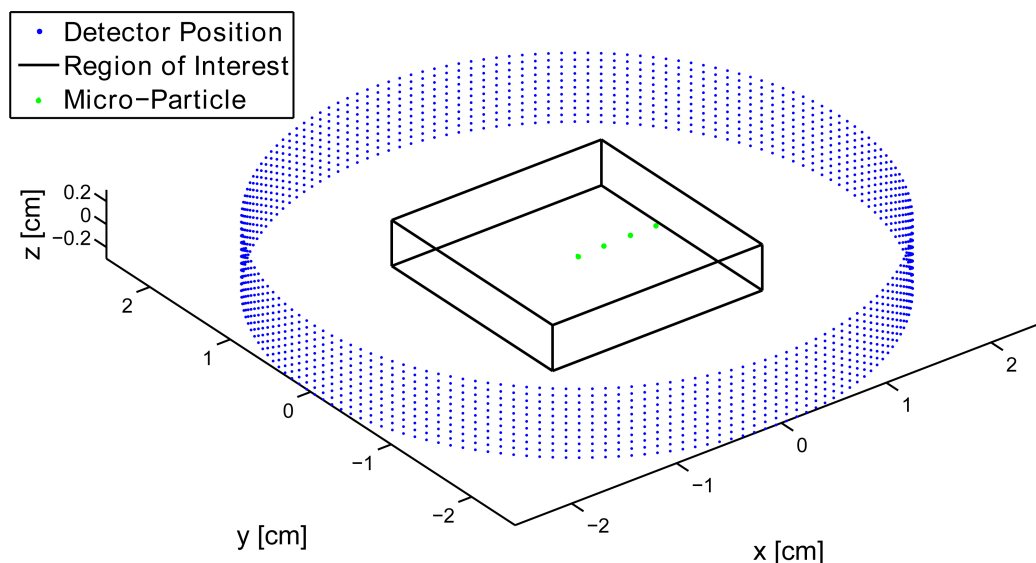


Figure 5.9: Detector positions and ROI for the cylindrical detection geometry used in simulations and experiments. For better visibility only every second z-scan position is depicted.

transducer. The effect has already been described in section 5.3 about two-dimensional measurements of a line transducer. Also, the reconstructed absorption values are severely reduced for peripheral absorbers, resulting in significant quantification errors. Figure 5.10 (e) and (k) demonstrates smearing of the absorbers over almost the entire ROI in the z-direction, corresponding to strong out-of-plane artifacts. In contrast to that, the reconstructions retrieved with the full three-dimensional model including the SIR of the detector significantly reduce the smearing in the out-of-plane (figure 5.10 (f) and (l)) and in-plane directions (figure 5.10 (c) and (i)). Altogether, the resolution in all spatial dimensions can be strongly improved with the 3D model incorporating the SIR of the transducer.

Furthermore, it is shown that the error in the reconstructed absorption value is size dependent. More precisely, figure 5.11 (a) and (d) shows the horizontal profiles of the four absorbers along the x-axis in the middle plane. In case of two-dimensional model-based reconstructions, the values of the ratio between the retrieved amplitudes for the outer and the inner absorbers are  $\approx 10\%$  for the small absorbers and  $40\%$  for the big absorbers, respectively. When the full 3D model is applied, these values increase to  $40\%$  and  $75\%$ , respectively, which indicates that the quantitative errors are considerably reduced with the latest approach. It is important to notice that the overall improvement of the reconstruction was also influenced by the length of the scan in the z-direction. The influence of the scan length on the reconstruction was already shown for the two-dimensional case in section 5.3.2. Overall, longer scans led to a better conditioned model matrix and thereby inversion problem, so that better quality reconstructions were generally obtained.

Considering computational requirements, building a three-dimensional model matrix for

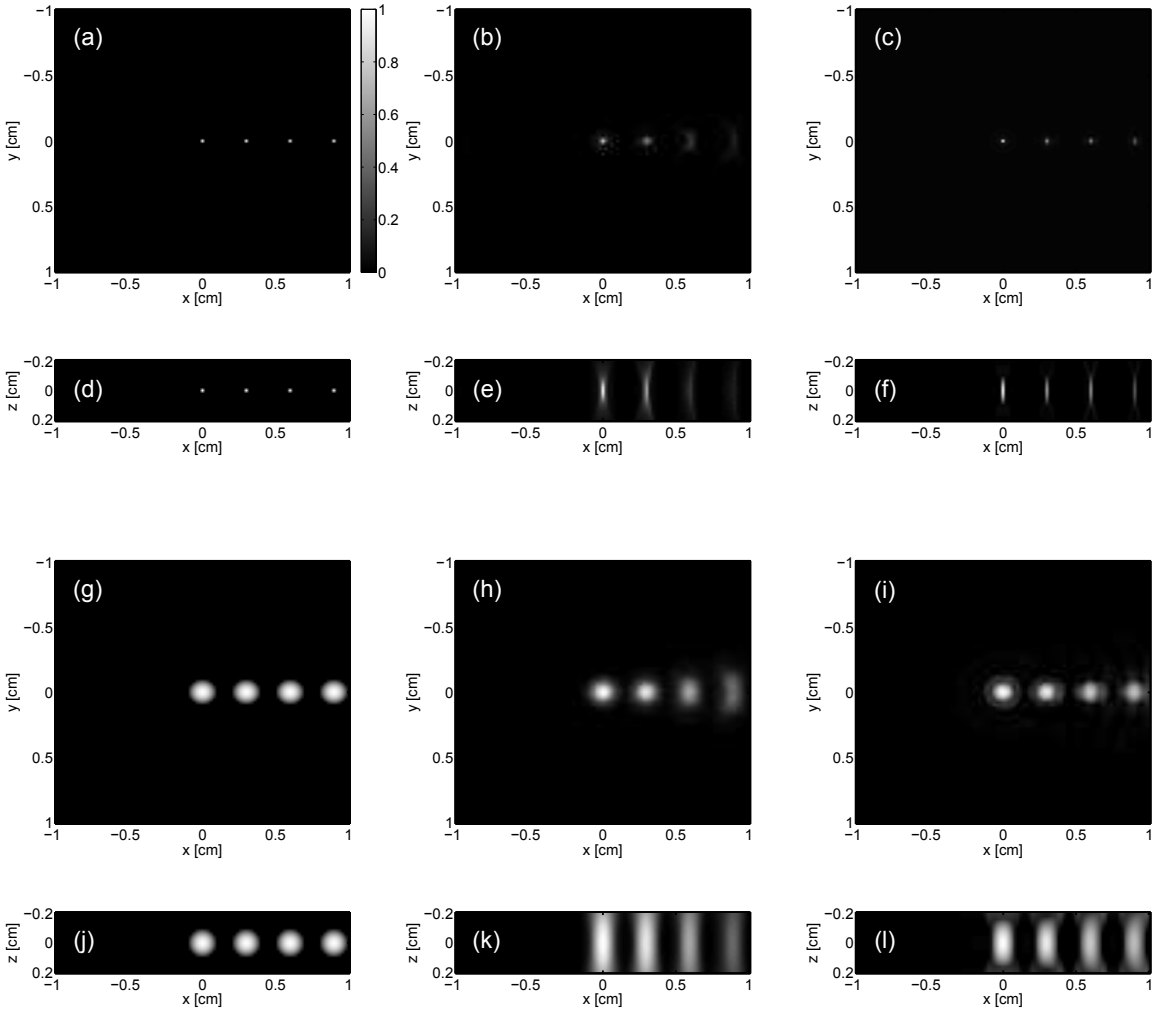


Figure 5.10: Simulation of four absorbers with radius  $r_0 = 200 \mu\text{m}$  (a) and (d) and radius  $r_0 = 1 \text{ mm}$  (g) and (j) placed along the positive x-axis in the center of the ROI. (b) and (h) depicts the maximum intensity projection (MIP) along the z-axis of the stack of 2D reconstructions and (e) and (k) its MIP along the y-axis. (c) and (i) show the MIP along the z-axis of the 3D reconstruction taking the spatial impulse response (SIR) of the transducer into account. The MIP along the y-axis is depicted in (f) and (l).

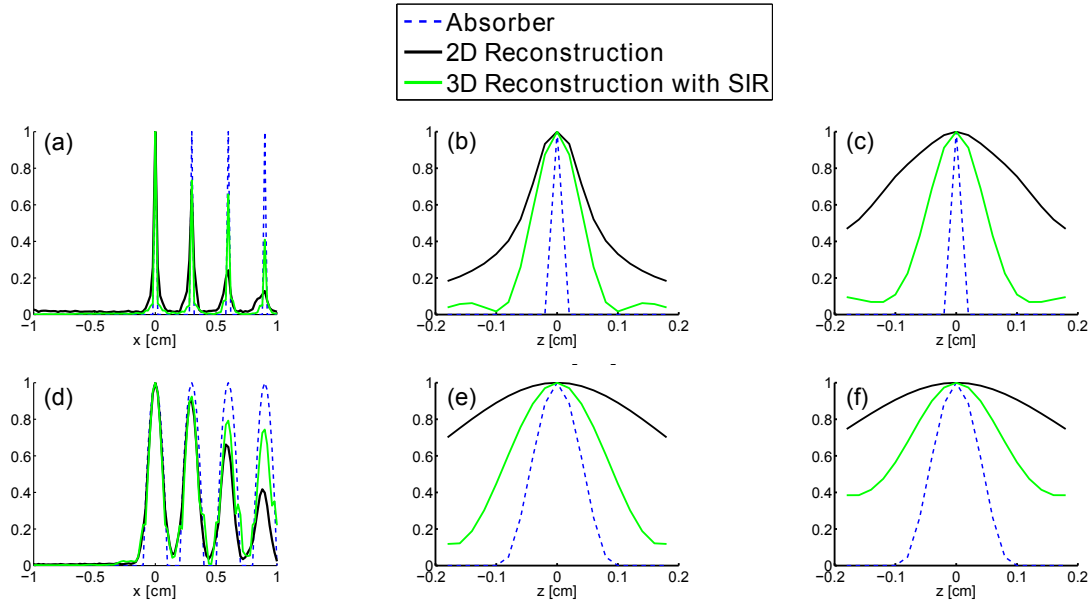


Figure 5.11: (Normalized) absorption values along the  $x$ -axis in the middle plane for four absorbers with radius  $r_0 = 200 \mu\text{m}$  are shown in (a) and  $r_0 = 1 \text{ mm}$  in (d). Relative improvement of the absorption values in the  $z$ -direction is depicted for the central absorber in (b) and (e) and the outmost absorber in (c) and (f).

the entire detection geometry, assuming point detectors, took about 130 seconds. Therefore, calculation of the entire matrix  $\mathcal{M}_{sum}$ , which is the sum of 350 such point detector matrices, would have taken over 12 hours and require 12.8 GB of memory for storage. In contrast, computation of the model matrix  $\mathcal{M}_{SIR}$  comprised of three steps. First, a three-dimensional point-detector matrix  $\mathcal{M}$  had to be calculated. Then, for each of the lines defining the surface  $\mathcal{S}$  of the transducer, an analytic SIR was calculated. The entire surface's SIR,  $h_{SIR}$ , was then approximated as in equation 5.9, by summing the individual SIRs of the lines. Finally, model matrix  $\mathcal{M}$  and SIR  $h_{SIR}$  had to be convolved, yielding  $\mathcal{M}_{SIR}$ . In total, the calculations had a duration of roughly 8 hours. Memory requirements for storage of  $\mathcal{M}_{SIR}$  were the same as for  $\mathcal{M}_{sum}$ . All three-dimensional model matrices were computed on a workstation computer  $2 \times$  Intel Xeon DP X5650 ( $6 \times 2.67 \text{ GHz}$ ) with 144 GB of random-access memory (RAM).

## 5.5 Experiments in Two Dimensions

In order to emphasize the benefits of including the detector size into the reconstruction algorithm, experiments with tissue-mimicking Agar phantoms containing micro-particles were carried out. The cylindrical phantoms with a diameter of 2 cm were prepared using a gel made from distilled water, containing Agar (Sigma-Aldrich, St. Louis, Missouri, USA)

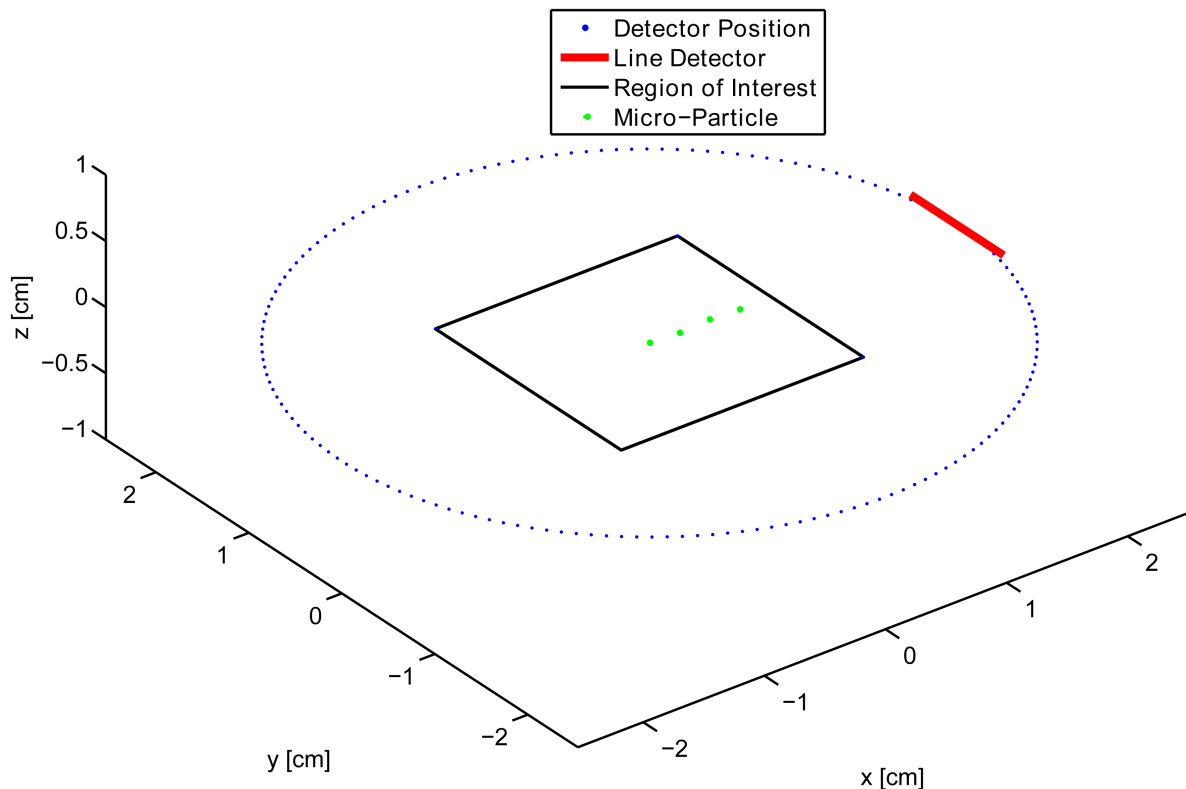


Figure 5.12: Transducer positions along a circumference enclosing the ROI with four micro-particles. At each detector position a pressure wave is recorded with a line transducer.

for jellification (1.3% w/w) and an Intralipid 20% emulsion (Sigma-Aldrich, St. Louis, Missouri, USA) for light diffusion and more uniform illumination (6% v/v), resulting in a gel presenting a reduced scattering coefficient of  $\mu'_s \approx 10 \text{ cm}^{-1}$ . Then, four polyethylene micro-particles with an approximate diameter of  $200 \mu\text{m}$  (BKPMS 180 to 212  $\mu\text{m}$ , Cospheric LLC, Santa Barbara, California, USA) had been placed in one plane, starting at the center of the ROI, moving outwards on a line (figure 5.12). Imaging was performed with the system described in 3.4.1, using a cylindrically focused transducer with a 1.3 cm diameter. Within the focal plane, the transducer acts approximately as a line transducer. Thereby, optoacoustic signals were acquired every  $2.25^\circ$ , resulting in 160 projections of a single plane. The radius of the detection circumference was set identical to the focal width of the transducer at 2.54 cm (see figure 5.12). Again, the ROI consisted of  $201 \times 201$  pixels, equivalent to  $2 \times 2 \text{ cm}^2$ , resulting in a uniform resolution of  $100 \mu\text{m}$ .

Image reconstruction was performed in three different ways. First, an image was calculated by means of the Universal Back-Projection formula presented in 4.6. Then, model-based inversion by means of the IMMI algorithm was employed. Thereby, a model matrix  $\mathcal{M}$  assuming point transducers and model matrices  $\mathcal{M}_{SIR}$  and  $\mathcal{M}_{sum}$  (31 points) incorporating the detector geometry were calculated. Inversion was performed iteratively by means

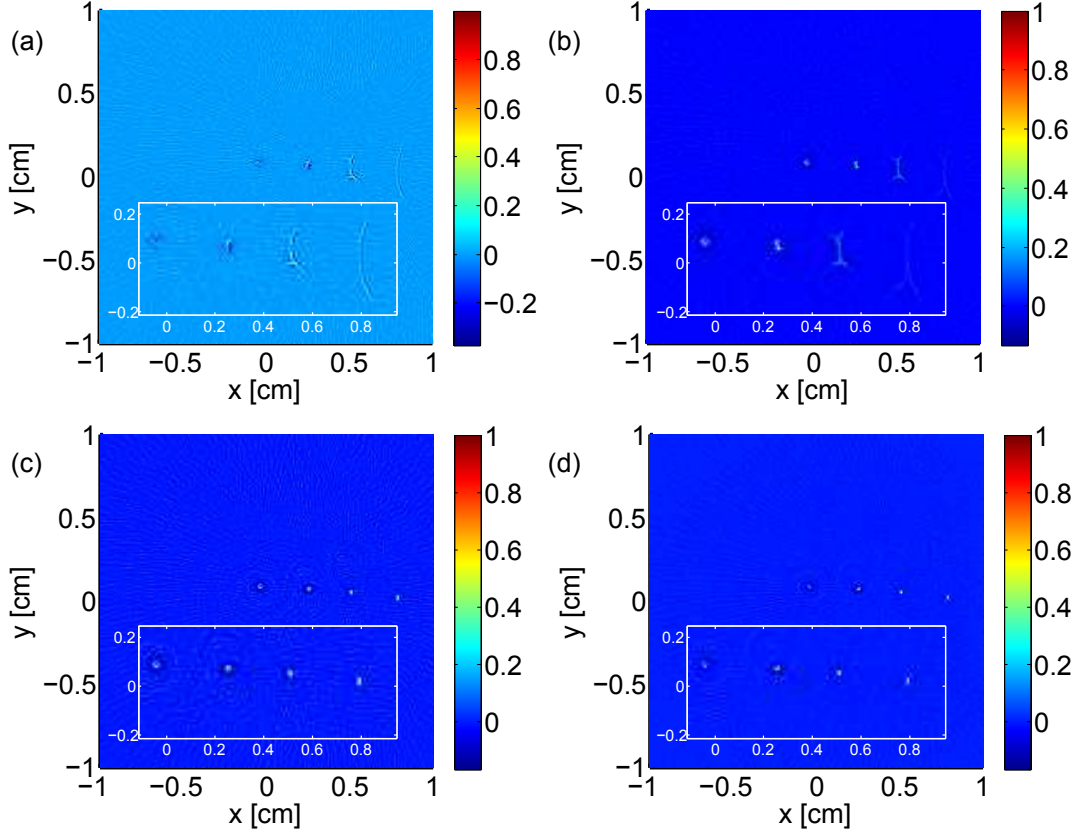


Figure 5.13: (a) Reconstruction of four micro-spheres using the Universal Back-Projection formula. (b) Model-based reconstruction assuming point detectors. Image reconstruction applying (c) model matrix  $\mathcal{M}_{sum}$  and (d) applying model matrix  $\mathcal{M}_{SIR}$ .

of the LSQR-algorithm.

In analogy to the results shown in the simulations section, the discrepancy between theoretically assumed point detectors and actually applied finite-size transducers, affects heavily the reconstructions, as can be seen in figure 5.13. Thereby, figure 5.13 (a) and (b) clearly show the characteristic smearing and damping of the absorption coefficients in the cases where point absorbers are assumed. Again, the effect becomes more explicit with increasing distance of the absorbers from the rotation center of the detection circle. However, the micro-particle positioned approximately in the center of the ROI gets reconstructed perfectly. When applying the enhanced model matrices  $\mathcal{M}_{SIR}$  and  $\mathcal{M}_{sum}$  for reconstruction, figure 5.13 (c) and (d) demonstrate, that the smearing effect vanishes and the original size of the micro-particles can be approximately recovered.

When comparing the maximum value of the reconstructions projected along the columns of the images (figure 5.14), it can be seen, that the algorithms assuming point-like detectors barely recover the micro-sphere positioned at the edge of the ROI. The absorption value reconstructed is about 10% of the peak value. In comparison to that, both model-based

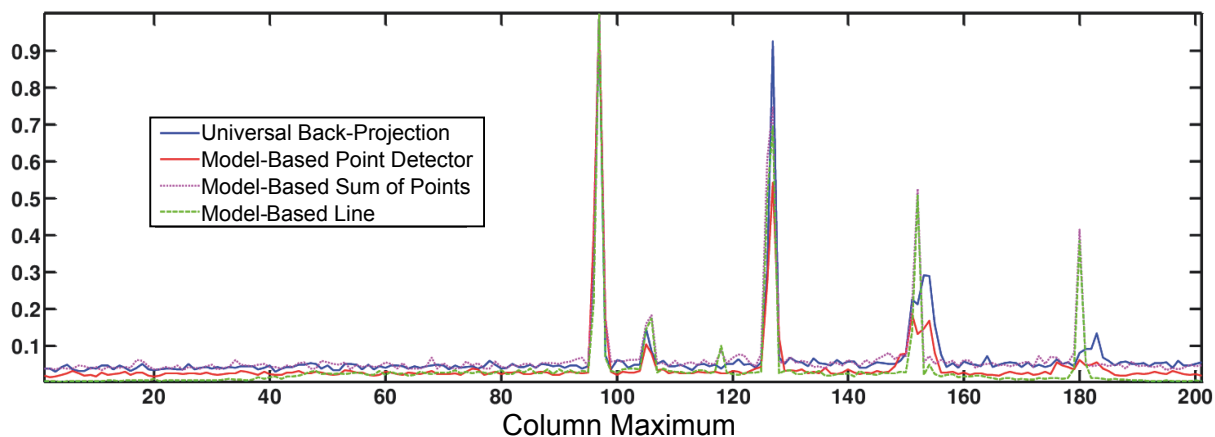


Figure 5.14: Maximum along the x-axis of the image reconstructions shown in figure 5.13.

approaches incorporating the detector shape reconstruct the absorption coefficient with approximately 45% of the peak value. However, the micro-sphere positioned at the center of rotation of the imaging system gets reconstructed perfectly by all inversion algorithms. This is due to the fact, that the finite-size effect of the detector is minimal at the center of rotation, as pressure waves originating at the center hit all detector surfaces perpendicularly at the same time instant. Another effect becoming visible in the reconstructions is that the Universal Back-Projection algorithm creates negative values around the absorbers, which have no physical interpretation. This effect is much weaker for model-based reconstructions and can be even prevented by including a positivity constraint within the iterative inversion of the matrix-vector equation. Moreover, figure 5.14 confirms that the noise level of the model-based reconstruction using matrix  $\mathcal{M}_{SIR}$  is significantly lower as compared to the other reconstructions.

## 5.6 Experiments in Three Dimensions

Finally, the advantages of modeling the entire detector shape within a three-dimensional reconstruction algorithm were showcased by conducting several optoacoustic experiments. Therefore, the imaging systems introduced in section 3.4.1 and 3.4.2 were used, both covering a cylindrical detection geometry with cylindrically focused transducers. Image reconstruction in all cases was performed in two different ways. On the one hand, a two-dimensional model matrix  $\mathcal{M}_{2D}$ , representing the detector positions of a single circumference surrounding the three-dimensional ROI, was calculated. Then, only the optoacoustic measurements, corresponding to a single detection circumference, are considered for inversion with model matrix  $\mathcal{M}_{2D}$ . Consecutively taking all the detector ring measurements into account, a stack of two-dimensional images is reconstructed, representing the volumetric ROI. On the other hand, a full three-dimensional model matrix  $\mathcal{M}_{SIR}$ , including the geometry of the transducer, is calculated. Then, image reconstruction of the entire

ROI implies inversion of the matrix-vector equation 5.11, considering all measurements at the same time.

### 5.6.1 Micro-Particles

First, the same tissue-mimicking Agar phantoms containing micro-particles, as described in the previous section, were measured with the imaging system presented in section 3.4.1. Briefly, the cylindrical phantoms had a diameter of 2 cm and were prepared with a gel made from distilled water, containing Agar (Sigma-Aldrich, St. Louis, Missouri, USA) for jellification (1.3% w/w) and an Intralipid 20% emulsion (Sigma-Aldrich, St. Louis, Missouri, USA) for light diffusion and more uniform illumination (6% v/v). The resulting opaque gel had a reduced scattering coefficient of  $\mu'_s \approx 10 \text{ cm}^{-1}$ . As optoacoustic sources, four polyethylene micro-particles with an approximate diameter of 200  $\mu\text{m}$  (BKPMS 180 to 212  $\mu\text{m}$ , Cospheric LLC, Santa Barbara, California, USA) were placed in a single cross-sectional plane, starting at the center of the ROI, moving outwards on a line (figure 5.15 (a) and (d)). Optoacoustic signals were acquired for the tomographic geometry of section 5.4.1 which is depicted in figure 5.9. More precisely, 160 projections were measured along a circumference (2.25° step). Subsequently, this detection ring was scanned along 0.6 cm in elevational direction with a 200  $\mu\text{m}$  step size (31 steps) resulting in 4960 total measurement positions of the transducer. The radius of the detection circumference was adjusted at 2.54 cm, to be identical to the focal width of the transducer. After discretization, the ROI consisted of  $101 \times 101 \times 21$  pixels, covering  $2 \times 2 \times 0.4 \text{ cm}^3$ , with a uniform resolution of about 200  $\mu\text{m}$  and centered inside the detector ring and the scanning range.

As in section 5.4.1, image reconstructions, with both  $\mathcal{M}_{2D}$  and  $\mathcal{M}_{SIR}$ , were computed on a workstation computer 2× Intel Xeon DP X5650 (6 × 2.67 GHz) with 144 GB of RAM. The LSQR algorithm was executed with MATLAB (Mathworks, Natick, MA, USA). For inversion in the two-dimensional case, the LSQR algorithm showed convergence, so no Tikhonov regularization was employed. The three-dimensional reconstruction was performed by means of the LSQR algorithm with standard Tikhonov regularization, optimizing the value of  $t$  to give the best possible image quality. The results of the image reconstructions can be seen in figure 5.15. More precisely, sub-images 5.15 (a) and (d) show the approximate position of the four micro-particles as a maximum intensity projection (MIP) along the  $z$ - and  $y$ -axis, respectively. The corresponding MIPs resulting from the stack of two-dimensional reconstructions can be seen in sub-figures 5.15 (b) and (e). In plane, as expected from the simulations, absorbers positioned remotely from the center of rotation, appear smeared and with a damped pixel value in the reconstructions. The effect becomes stronger with increasing distance from the center of rotation. By examining the MIP along the  $y$ -axis, micro-particles actually confined to the middle plane, appear elongated and spread out over the entire ROI, resulting in strong out-of-plane artifacts. At the position of the outmost absorber even several peaks are expressed, suggesting the existence of more than one absorber.

Then, sub-images 5.15 (c) and (f), depict the results obtained by inverting the full 3D model matrix  $\mathcal{M}_{SIR}$ . In plane, all four micro-particles can be clearly identified, being

confined to their actual position and size. Moreover, sub-image (f) shows four distinct micro-particles, that are limited in their extension in z-direction. The positive effect of the incorporation of the impulse response are corroborated by sub-images 5.15 (h) and (i). Incorporating detector properties within model-based reconstruction, improves focusing of both the central and outmost absorber to their actual position around image plane  $z=0$ . Furthermore, sub-image (g) suggests, that the overall signal-to-noise level is higher in the 3D reconstruction including the detector shape. Figure 5.15 (k) depicts the middle plane of the stack of 2D reconstructions with a threshold between 0 and 0.1 in order to make the noise floor more visible. Clearly, the same plane, obtained via the full 3D reconstruction and the same threshold, shows visibly less noise (5.15 (l)). As a measure for the noise level, the standard deviation  $\sigma_{noise}$  of the reconstructed pixel values excluding the absorber region has been calculated. Therefore, the regions marked in figure 5.15 (j), containing all pixels with y-values between  $[-1, -0.5]$  and  $[0.5, 1]$ , have been defined and the standard deviation among those pixels has been determined. For the 2D model reconstruction the value was  $\sigma_{noise}^{2D} = 1.1655$  whereas in the case of the full 3D model reconstruction the calculation yielded  $\sigma_{noise}^{3D,SIR} = 0.5373$ , corroborating the assertion of a lower noise level in the 3D reconstruction.

### 5.6.2 Mouse Spleen

The present section, aims at substantiating the advantages of applying a full three-dimensional imaging model incorporating the detector shape, for optoacoustic measurements of biological tissue. To that end, an *ex-vivo* spleen of a mouse was embedded in a translucent gel made from Agar and imaged with the high-throughput optoacoustic tomographic system described in section 3.4.2. After discretization, the ROI consisted of  $111 \times 111 \times 31$  pixels, covering  $2.2 \times 2.2 \times 0.6 \text{ cm}^3$ , with a uniform resolution of about  $200 \mu\text{m}$  and centered inside the detector ring. As the imaging system comprises of a detector ring, the size of each transducer element is limited to approximately 2 mm in azimuthal and 15 mm in elevational directions, respectively. Due to the small width of the elements as compared to their height, the main effect in the reconstructions is the out-of-plane spreading in z-direction of the absorbers. Therefore, modeling of the transducer surface in this case was simplified by discretizing it with 150 surface elements in the elevational direction and neglecting azimuthal extension. A comparison of the results obtained with the two-dimensional model and the simplified three-dimensional model is displayed in figure 5.16. The 3D model shows a visible improvement in the elevational resolution, as can be seen in the MIPs along the y-direction (figure 5.16 (c) and (d)). The out-of-plane artifacts are especially significant for the background absorption, which generates mainly low-frequency acoustic waves, and the focusing capacity of the transducer is lower in this case. The reduction of the out-of-plane artifacts corresponding to low spatial frequencies also improves the visual quality of the MIP along the z-direction. The weak SNR observed in the stack of two-dimensional reconstructions of figure 5.16 (a) was enhanced by applying the 3D model (figure 5.16 (b)).

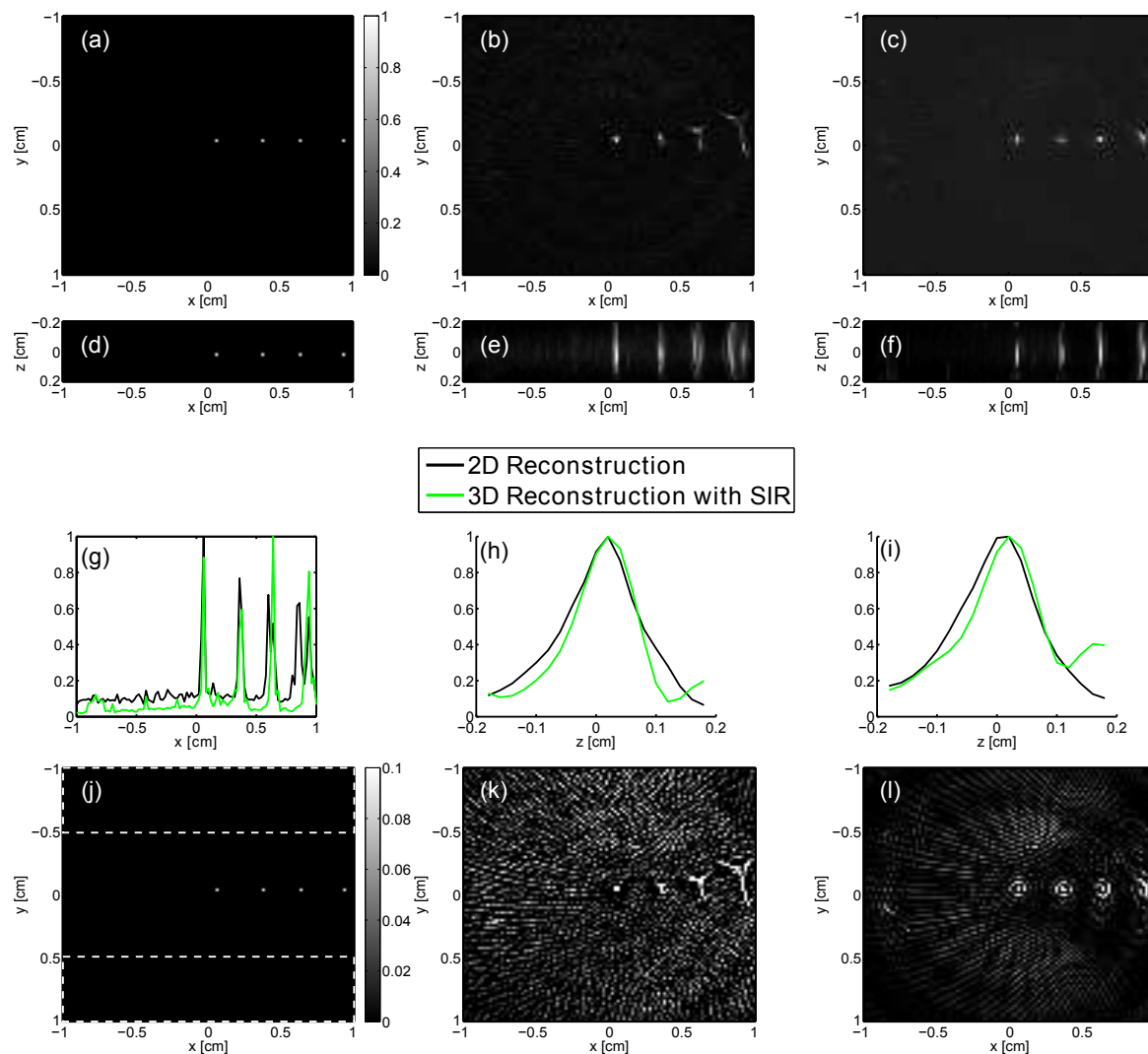


Figure 5.15: Approximate position of four micro-spheres within the three-dimensional ROI. (a) depicts the MIP along the  $z$ -axis and (d) the MIP along the  $y$ -axis. (b) and (e) show the corresponding MIPs of the stack of reconstructions obtained via inversion of the 2D model. (c) depicts the MIP along the  $z$ -axis of the reconstruction obtained by inverting the full 3D model matrix  $\mathcal{M}_{SIR}$ . The MIP along the  $y$ -axis is shown in (f). In (g), the absorption values of the four micro-spheres projected along the  $y$ -axis for both reconstructions are shown. The relative improvement of the absorption values in the  $z$ -direction is shown for the central absorber in (h) and the outmost absorber in (i). (j) The position of the four absorbers in the middle plane with a threshold set from 0 to 0.1. The two regions used for determining the noise level in the reconstructions are marked with the white dashed boxes. (k) depicts the middle plane of the stack of 2D reconstructions, whereas (l) shows the central plane of the reconstruction obtained by inverting the full 3D model with the same threshold from 0 to 0.1.

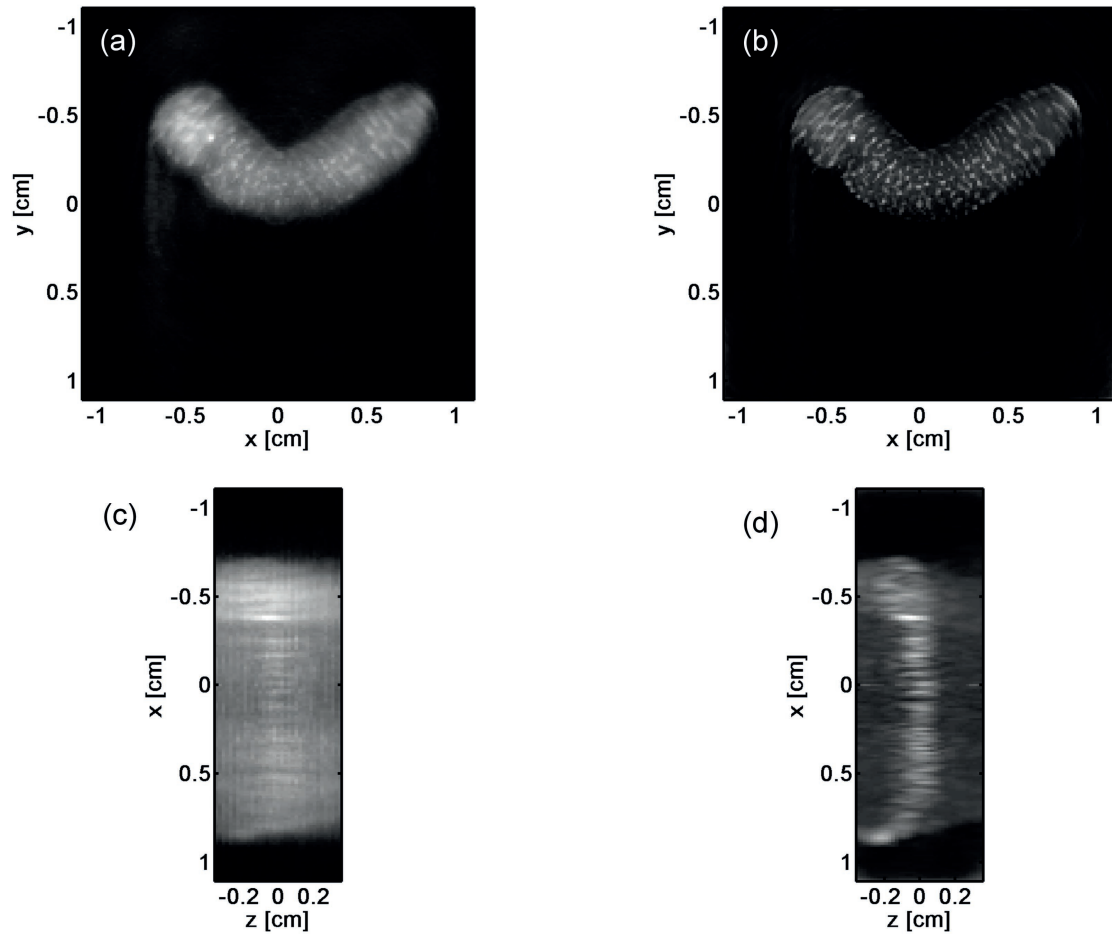


Figure 5.16: Reconstructions of a mouse spleen embedded in Agar. (a) and (c) show the MIPs along the z- and y-axis resulting from the stack of reconstructions obtained via the two-dimensional IMMI algorithm. (b) and (d) depict the corresponding MIPs resulting from the 3D model with the detector properties incorporated.

## 5.7 Concluding Remarks

This chapter introduced two strategies to incorporate geometric detector properties into model-based image reconstruction. Thereby, the detector surface was approximated either by points or lines. The inclusion of the transducer shape into the reconstruction algorithm can be performed both in two and three dimensions. In order to substantiate the benefits of an enhanced imaging model, a series of simulations and experiments has been conducted. In this process, it could be shown that, both the point and line model accurately capture the effects of an extended detection surface. However, especially for large detectors, the line model should be favored over the point model, as calculation times are significantly lower. The improvements achieved in simulations could be translated even to experiments involving biological tissue. Overall, image resolution in all spatial dimensions could be restored, allowing the correct interpretation and quantification of optoacoustic reconstructions.

# Chapter 6

## Optoacoustic Tomography with a cw-Laser System

Besides generating optoacoustic signals by means of a pulsed laser system, an alternative method implies the application of a cw-laser. Thereby, the output of the cw-laser is modulated with a LFM chirp, generating a pressure wave response with an identical, time-delayed profile, as has been shown in section 2.2.4. By using correlation processing techniques, such as matched-filter compression, weak optoacoustic signals, mostly hidden in the imaging system's noise, can be recovered and serve as the input of a reconstruction algorithm. The current chapter presents results, that demonstrated for the first time the capability of optoacoustic cw-laser systems to operate tomographically and *in-vivo* [47].

### 6.1 Experimental Results with a cw-Laser System

Throughout this chapter, all optoacoustically generated pressure data was acquired with the cw-laser imaging system described in section 3.4.3. Subsequent to the experimental measurements, the detected pressure signals  $p(\vec{r}, t)$  are cross-correlated with the LFM chirp signal  $l(t)$ , which is simultaneously recorded by a photo-diode. Signal-processing by means of matched filter pulse compression, as explained in section 4.3, generates the cross-correlation function

$$CC(t) = \int_{-\infty}^{\infty} p^*(\vec{r}, \tau)l(t + \tau)d\tau, \quad (6.1)$$

for every detector position  $\vec{r}$  on the detection circumference enclosing the ROI. The cross-correlation function  $CC(t)$  serves as the input of the back-projection algorithm described in 4.9 which was used for reconstruction of all images shown herein.

First, in order to showcase the ability to perform tomographic imaging, two cylindrical phantoms with a diameter of approximately 4 mm were prepared. The phantoms consisted of a clear gel made from distilled water containing Agar (Sigma-Aldrich, St. Louis, Missouri, USA) for jellification (1.3%  $w/w$ ), enclosing a rectangular insertion mixed from

India ink and Agar. The rectangular absorber had an absorption coefficient of approximately  $\mu_a \approx 2 \text{ cm}^{-1}$ , which was determined through measurements with a spectrometer. A photograph of the phantom and its reconstruction can be seen in figure 6.1 (a) and (b). The boundaries at the interface of the absorber and the transparent Agar phantom are clearly highlighted in the reconstruction and correspond to the excited frequencies 1-5 MHz of the LFM chirp. Spectral frequency components of less than 1 MHz, which would excite the absorption distribution within the insertions, are not prominently stimulated by the frequency band employed, and consequently do not appear in the reconstruction.

Then, a second cylindrical phantom containing a smaller insertion with a hexagonal shape of 1.5 mm diameter was imaged. Again, the absorption coefficient was determined to be approximately  $\mu_a \approx 2 \text{ cm}^{-1}$ . Photograph and optoacoustic image reconstruction of the phantom are depicted in figure 6.1 (c) and (d). Size and shape of the smaller insertion match exactly the original phantom, proving the ability of the cw-laser system to optoacoustically image cross-sectional slices.

Assessing the SNR performance of the cw-laser imaging system, was done by the measure

$$SNR_{cw} = 20 \log_{10} \left( \frac{\mu_{signal}}{\sigma_{noise}} \right), \quad (6.2)$$

where  $\mu$  denotes the mean and  $\sigma$  the standard deviation of the signal and noise within the ROI. The value for the reconstruction in figure 6.1 (b) was  $SNR_{cw} = 32.1 \text{ dB}$  and for figure 6.1 (d)  $SNR_{cw} = 32.3 \text{ dB}$ . All artifacts visible in the reconstructions, especially speckles and small oscillations, can be attributed to the signal processing procedure of calculating the cross-correlation function, which represents a sinc-function.

Following the positive results obtained by tomographically imaging cross-sections of Agar-phantoms, an *in-vivo* experiment with a mouse was conducted. Considering the experience gained with phantom measurements, imaging the mouse-tail fitted the dimensions of the absorbers in the previous experiments. For this purpose, the mouse tail of a female BALB/c mouse was measured at a height of about 4 cm from the distal end. In accordance with the measurement protocol, approved by the Government of Bavaria, the mouse was anesthetized by isoflurane gas, followed by catheterization of the right vein at 2 cm from the distal end. During the experiment, in order to ensure a stable measurement, the mouse was attached to a custom-made mouse-tail holder.

Then, a first tomographic measurement of the mouse-tail was performed to serve as a base line dataset. Following, 130 nmol of Indocyanine green (ICG) were injected via the catheter into the mouse tail and additional measurements were acquired at several time points. In order to compensate the ICG clearance from the blood stream through the hepatobiliary tract, occurring during the acquisition time of  $\approx 10$  minutes per image, an additional 100 nmol of ICG were administered at a projection angle of  $140^\circ$ . Subsequent to the *in-vivo* measurements, the mouse was euthanized and frozen to  $-80 \text{ }^\circ\text{C}$ , in order to cryoslice and photograph the mouse tail for comparison with the image reconstructions. All mouse-tail images reconstructed from the measurements can be seen in figure 6.2, with sub-figure (a) showing the reconstruction from the base line dataset. All four major tail blood vessels, both lateral caudal veins, the dorsal vein and the ventral artery, are visible. Accordingly,

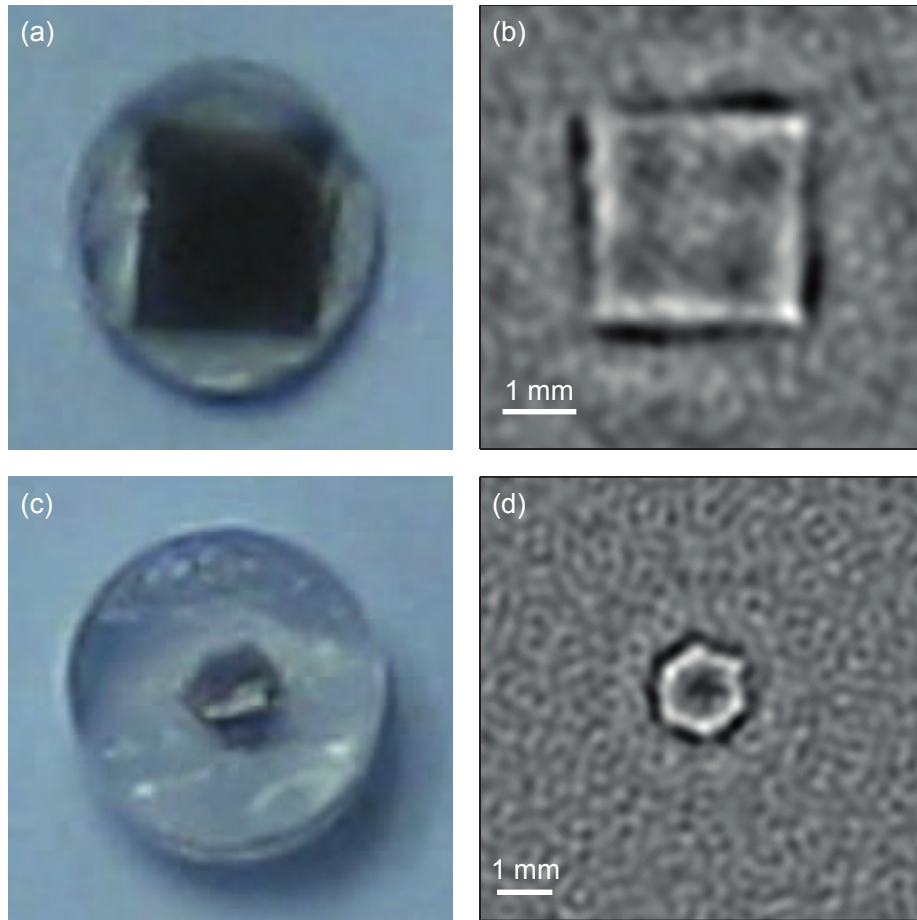


Figure 6.1: (a) Photograph of the Agar-phantom with a rectangular optical absorber inclusion of absorption  $\mu_a = 2 \text{ cm}^{-1}$  and (b) its tomographic reconstruction. (c) Photograph of the Agar-phantom including a hexagonal insertion of 1.5 mm diameter and absorption coefficient of  $\mu_a = 2 \text{ cm}^{-1}$ . (d) Reconstruction of the hexagonal phantom.

figure 6.2 (b) and (c) depict the reconstructions of post-ICG administration measurements obtained at two time points approximately 10 minutes apart. The aim was to investigate the ability to record dynamic variations of optical absorption in response to the ICG clearance from the blood circulation. Specifically, by comparing the scale bars, figure 6.2 (b) depicts a two-fold increase in the absorption coefficient, whereas figure 6.2 (c) indicates reduced intensity due to ICG clearance. Again, assessing the SNR of reconstructions with the measure introduced in 6.2, yields a value of  $SNR_{cw} = 40.7 \text{ dB}$  for sub-figure 6.2 (a) and  $SNR_{cw} = 49.6 \text{ dB}$  for sub-figure (b). As compared to the phantom reconstructions, an increase of the SNR for the *in-vivo* images is justified by the fact that the absorption coefficient of blood vessels before ICG injection is twice that of the Agar phantoms [99] [100]. The photograph depicted in figure 6.2 (d) shows the frozen and cryosliced mouse-tail.

Here, all four major blood vessels can be identified and showcase the good correspondence of the optoacoustic reconstructions with actual cross-section of the mouse-tail.

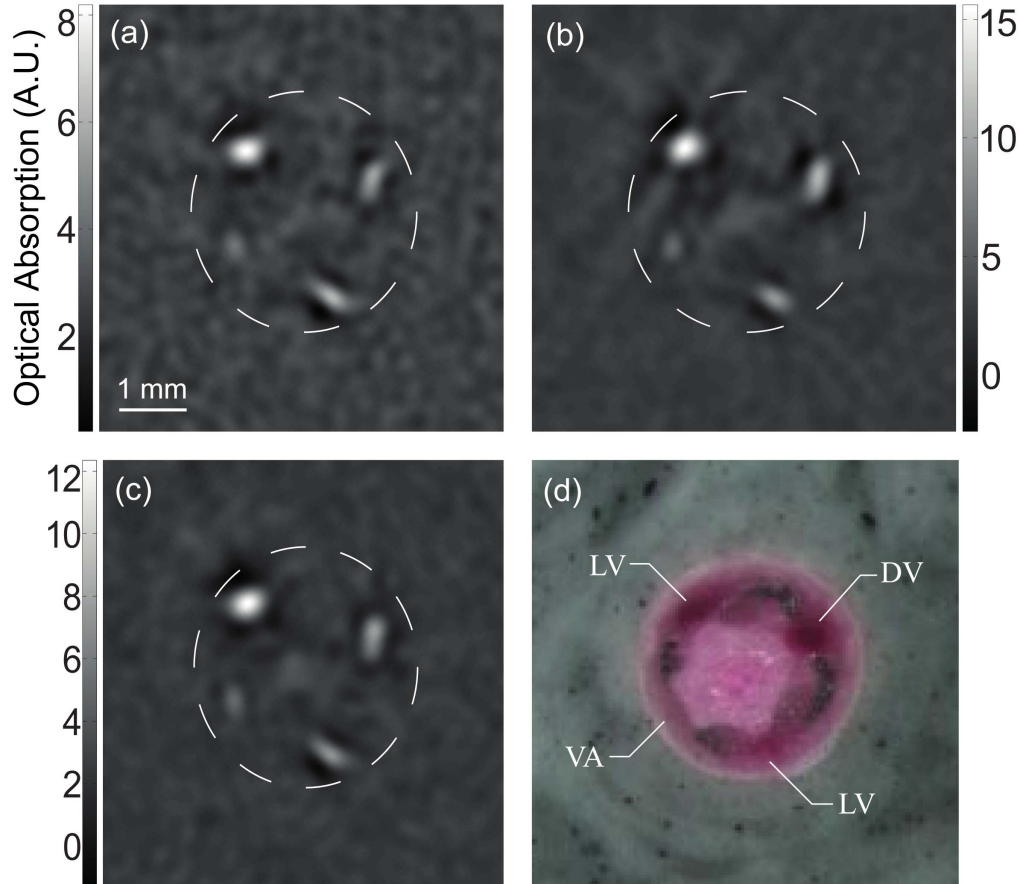


Figure 6.2: (a) Tomographic reconstructions of a mouse tail measured *in-vivo* with the cw-laser system. (b) Reconstruction of data measured during ICG injection and (c)  $\approx 10$  minutes after ICG injection. (d) Cryoslice of the mouse tail showing the lateral caudal veins (LV), the dorsal caudal vein (DV) and the ventral caudal artery (VA). The dashed circle represents approximately the tail surface.

## 6.2 Concluding Remarks

This chapter puts the theoretically derived image reconstruction algorithm of section 4.3 into practice. It could be shown for the first time, that optoacoustic signals excited with a cw-laser source are suited to generate cross-sectional images. The developed system in combination with the dedicated reconstruction algorithm proofed its imaging capabilities with Agar-phantoms and by monitoring the dynamic variations of optical absorption in

---

response to ICG clearance from blood circulation within an *in-vivo* mouse-tail. Furthermore, in contrast to commonly used pulsed lasers, which are bulky and expensive, cw-laser sources are relatively cheap and compact, allowing to reduce costs and size of optoacoustic imaging systems.



# Chapter 7

## Efficiency Techniques for Model-Based Image Reconstruction

The main disadvantage of the model-based approach proposed in chapter 5 is its memory requirements. As all algebraic reconstruction methods, also the IMMI algorithm employed herein, become very time- and memory-consuming with increasing temporal and spatial resolution. Extending the imaging task to three dimensions only aggravates the problem. Both models presented,  $\mathcal{M}_{sum}$  and  $\mathcal{M}_{SIR}$ , needed each 12.8 GB of memory for storage of the matrix. Calculation time for building the matrices was  $\approx 8$  hours for  $\mathcal{M}_{SIR}$  and more than 12 hours for  $\mathcal{M}_{sum}$ . Depending on the size of the considered detector surface the number of nonzero elements of a model matrix increases significantly. For transducers typically used in optoacoustics, a 10-fold increase in nonzero elements is produced with respect to the model matrix  $\mathcal{M}$  for point detectors. Then, storage of the model matrix is an important issue to address in order for the method to be a viable tool in algebraic image reconstruction. This can be partially alleviated by simplifications of the model, as done in section 5.6.2 for imaging the spleen. However, larger matrices inevitably require the development of strategies to efficiently reconstruct high resolution images from multiple optoacoustic measurements.

### 7.1 Detection Symmetries

Tomographic imaging systems tend to acquire data from as many detection angles as possible, surrounding the ROI. Optimal angular coverage minimizes reconstruction artifacts, as the mathematical inversion of the forward problem becomes better conditioned. Therefore, also most optoacoustic tomographic imaging systems try to fully enclose the ROI by implementing a detection circumference (imaging systems 3.4.1 and 3.4.3) or, out of spatial limitations, detecting on a circle segment (imaging system 3.4.2).

Considering a model-based approach for image reconstruction implies the calculation of a model matrix, whose size, when held in storage, scales linearly with the number of angular projections taken into account. However, by choosing the detector positions wisely,

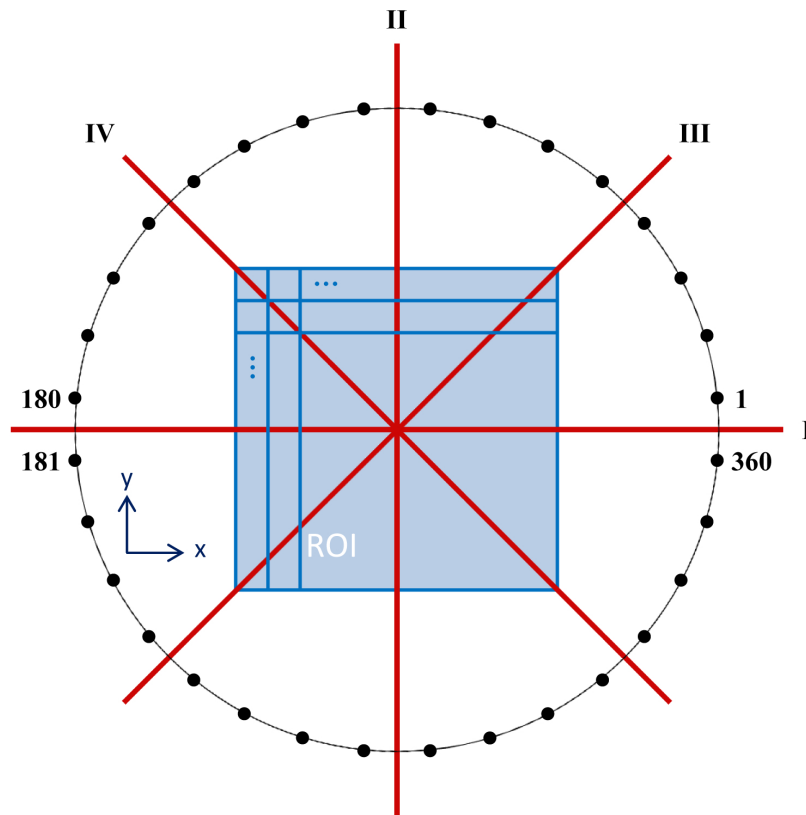


Figure 7.1: Four symmetry axes of a quadratic ROI and a  $360^\circ$  detection circumference.

calculating the entire model matrix is not necessary, as only a few projections contain the entire information about the imaging system. All other measurement positions can be easily obtained by taking advantage of symmetries within the detection geometry.

### 7.1.1 In-Plane Symmetries

In this section, the two-dimensional case of a detection circumference covering all  $360^\circ$  around a quadratic ROI, as depicted in figure 7.1, is considered. For the purpose of enabling an easy rationale, it is assumed, that 360 measurement positions are taken, resulting in a  $1^\circ$  step. The quadratic ROI possesses four symmetry axes, also shown in figure 7.1.

In a first step, by just calculating the model matrix for the upper half of symmetry axis I, only the first 180 transducer positions between  $0^\circ$  and  $180^\circ$  are taken into account. Thereby, one saves half of the memory required for storing the model matrix. However, detector position number 1 has the same relative position towards the ROI as detector position 181, up to renumbering the pixels. By properly creating a book-keeping list of how to renumber the pixels within the ROI for symmetry axis number I, the information of all measurement positions can be stored in a matrix of half the size. Iteratively applying

this technique to all four symmetry axes, merely one eighth of the measurement positions are needed, covering  $45^\circ$  of the entire circle. Altogether, besides the book-keeping list for reordering the pixels, the actually calculated model matrix requires now only one eighth of the memory initially needed for all 360 projections. In order to be able to exploit all four above described detection symmetries, the transducer positions must be equally distributed around the detection circumference. Furthermore, the total number of detector positions along the circle line has to be a factor of eight. For this reason, simulations and experiments, in this work, conducted with the single transducer imaging system described in 3.4.1 acquired 160 signals over  $360^\circ$ .

### 7.1.2 Out-of-Plane Symmetries

A lot of three-dimensional optoacoustic tomography systems, prefer a cylindrical detection geometry over a spherical one. This stems from spatial limitations, that hinder the ROI to be fully enclosed, as in case of a mouse for example, an anesthesia system with breathing tubes has to be connected to the ROI. In analogy to the rationale in the previous section, translational symmetries apply for a cylindrical detection surface. This fact can be exploited in order to further minimize the memory consumption of a model matrix used for image reconstruction. For simplicity, consider a volumetric ROI with one detector ring position per plane in  $z$ -direction (figure 7.2 (a)). It is assumed, that the number of scan positions in  $z$ -direction is an odd number. Now, instead of calculating the model matrix  $\mathcal{M}$  for all detector ring positions in  $z$ -direction, only the central position  $\mathcal{M}_{central}$  is calculated, yet, for a ROI of double the extension in  $z$ -direction (figure 7.2 (b)). Then, if the part of model matrix  $\mathcal{M}$  corresponding to detector ring position 1 is needed in a calculation (7.3 (a)), the exact same sub-matrix can be extracted from model matrix  $\mathcal{M}_{central}$ , by appropriately selecting a sub-ROI. From the perspective of detector ring position 1, all planes of the ROI have a  $z$ -coordinate greater than or equal to the detector's  $z$ -coordinate. Therefore, the corresponding part in matrix  $\mathcal{M}_{central}$  only considers those planes of the enlarged ROI whose  $z$ -coordinates are greater than or equal to the  $z$ -coordinate of the central detector ring (7.3 (b)). Iteratively, all detector ring positions within model matrix  $\mathcal{M}$  can be found in  $\mathcal{M}_{central}$  by stepping a sub-ROI through the enlarged ROI of matrix  $\mathcal{M}_{central}$  (7.3 (c) and (d)).

Overall, a model matrix for only one detector ring position has to be calculated. Even though the considered ROI is bigger, reduction of the memory capacity needed for storing the model matrix is significant, especially if a lot of detector positions per plane are considered. Finally, in analogy to the strategy for in-plane symmetries, taking advantage of the symmetry axis at the central detector ring position can further cut the memory consumption in half. All three-dimensional model-based reconstructions shown in this work, have been calculated by applying the above techniques.

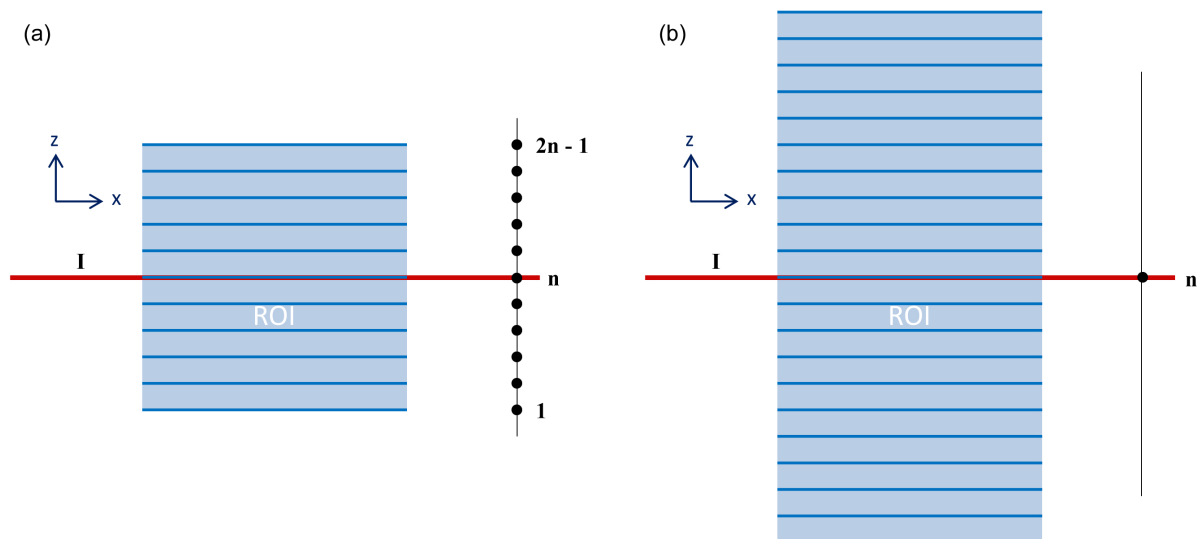


Figure 7.2: (a)  $2n-1$  positions of a linear scan with a detector ring and the corresponding planes of a volumetric ROI. The red line defines the symmetry axis in  $z$ -direction. (b) Central position  $n$  of a linear scan with a detector ring and a larger ROI used for the efficient calculation of the model matrix corresponding to the geometry defined in (a).

## 7.2 Wavelet Packets

High quality optoacoustic images commonly imply high resolution of the ROI to be reconstructed and a large number of optoacoustic measurements surrounding the ROI. This leads to very big model matrices used for algebraic image reconstruction, resulting in high computational demands for storing and handling the matrices. In effect, image reconstruction becomes either very slow or impracticable. A large model matrix  $\mathcal{M}$  implicates that either the matrix inverse  $\mathcal{M}^\dagger$  cannot be calculated due to memory limitations or even iterative inversion algorithms do not converge in a decent amount of time. This constriction can turn model-based inversion impracticable from a certain size of the matrix on.

A novel approach to handle model-based inversion and overcoming the above mentioned limitations, was first reported by Rosenthal et al.[101], which laid the groundwork of the following rationale. The basic concept consists of decomposing the reconstruction problem into a set of smaller inversion problems, which in turn can be solved with a sophisticated algorithm that would be impossible to use for model matrix  $\mathcal{M}$ . Inversion can then be performed, for example, by calculating the Moore-Penrose-Pseudoinverse, applying a least squares minimization algorithm, a  $\ell_1$ -norm minimization algorithm or by means of a singular value decomposition (SVD) for each of the matrices representing the set of smaller inversion problems.

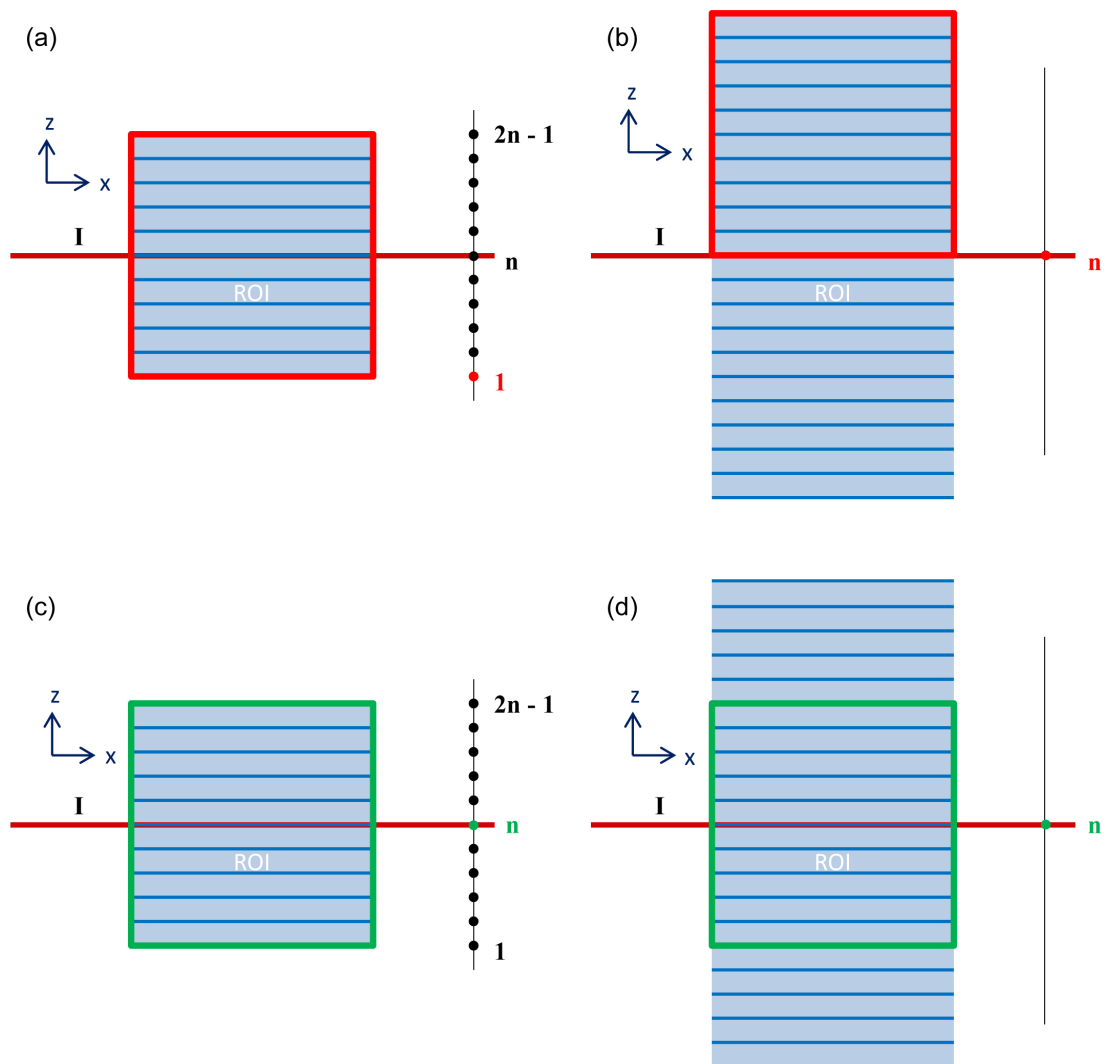


Figure 7.3: (a) ROI as seen from detector position 1 (red). (b) Enlarged ROI with a sub-ROI marked in red. The relative position of the red ROI towards detector position  $n$  corresponds to the setting of sub-figure (a). (c) ROI (green) as seen from the central detector position  $n$  and (d) the corresponding sub-ROI (green) of the enlarged ROI.

### 7.2.1 Theoretical Rationale

In the following derivation, a two-dimensional tomographic geometry setting as described in section 7.1.1 is considered (figure 7.1). In general, model-based reconstruction algorithms establish a connection between a set of optoacoustic measurements  $\vec{p}$  and an image  $\vec{H}$  in terms of the model matrix  $\mathcal{M}$ . With this framework, matrix  $\mathcal{M}$  can be understood as a finite-dimensional operator between the image space  $\mathcal{I} \subset \mathbb{R}^N$  and the projection space  $\mathcal{P} \subset \mathbb{R}^{MQ}$ ,

$$\mathcal{M} : \begin{cases} \mathcal{I} & \longrightarrow & \mathcal{P}, \\ \vec{H} & \longmapsto & \vec{p} = \mathcal{M} \cdot \vec{H}. \end{cases} \quad (7.1)$$

Here,  $M$  denotes the number of transducer positions,  $Q$  the number of time samples per detector measurement and  $N$  defines the total number of pixels in the image resulting in matrix  $\mathcal{M} \in \mathbb{R}^{MQ \times N}$ .

The forward model of the imaging system defined in 7.1 is now decomposed into a set of smaller models by means of the wavelet packet decomposition [102]. As all practical computations are in discrete space, also all wavelet packets in this work are presented in their discrete form as conjugate mirror filter banks [103]. Thereby, only orthogonal wavelets, such as the Daubechies wavelets, are considered herein. They can be defined by a finite sequence  $h[n]$  of length  $2A$ , acting as a low-pass finite impulse response (FIR) filter, called the scaling filter. Then, the corresponding high-pass filter, termed the wavelet filter, is represented by its FIR  $g[n]$  of even length  $2A$ , and can be calculated as the quadrature mirror filter of sequence  $h[n]$ ,

$$g[n] = \begin{cases} h[2A + 1 - n], & \text{n odd,} \\ -h[2A + 1 - n], & \text{n even.} \end{cases} \quad (7.2)$$

Naturally, image  $\vec{H}$  is a discrete two-dimensional object with the number of pixels in x- and y-direction defining its size. However, also optoacoustic measurements  $\vec{p}$  may be represented as discrete two-dimensional images in form of their sinogram, with  $Q$  and  $M$ , the number of time samples and measurement positions, as the image size. Then, a first level discrete wavelet decomposition of a two-dimensional object  $O[k, l]$ , ( $k = 1, \dots, K; l = 1, \dots, L$ ) is defined as

$$a[k, l] = \mathcal{A}O[i, j] = \sum_{i, j=-\infty}^{\infty} h[i - 2k]h[j - 2l]O[i, j], \quad (7.3)$$

$$d_1[k, l] = \mathcal{D}_1O[i, j] = \sum_{i, j=-\infty}^{\infty} h[i - 2k]g[j - 2l]O[i, j], \quad (7.4)$$

$$d_2[k, l] = \mathcal{D}_2O[i, j] = \sum_{i, j=-\infty}^{\infty} g[i - 2k]h[j - 2l]O[i, j], \quad (7.5)$$

$$d_3[k, l] = \mathcal{D}_3 O[i, j] = \sum_{i, j=-\infty}^{\infty} g[i - 2k]g[j - 2l]O[i, j]. \quad (7.6)$$

Wavelet reconstruction, on the other side, obeys the formula

$$\begin{aligned} O[k, l] &= \sum_{i, j=-\infty}^{\infty} h[k - 2i]h[l - 2j]a[i, j] \\ &+ \sum_{i, j=-\infty}^{\infty} h[k - 2i]g[l - 2j]d_1[i, j] \\ &+ \sum_{i, j=-\infty}^{\infty} g[k - 2i]h[l - 2j]d_2[i, j] \\ &+ \sum_{i, j=-\infty}^{\infty} g[k - 2i]g[l - 2j]d_3[i, j]. \end{aligned} \quad (7.7)$$

Applying operator  $\mathcal{A}$  to object  $O[k, l]$  in the decomposition process, yields the approximation coefficients  $a[k, l]$ , representing a down-sampled, low-passed version of  $O[k, l]$ . Equivalently, the three operators  $\mathcal{D}_1$ ,  $\mathcal{D}_2$  and  $\mathcal{D}_3$  generate the detail coefficients  $d_1[k, l]$ ,  $d_2[k, l]$  and  $d_3[k, l]$ , constituting a down-sampled version of  $O[k, l]$  that is high-passed over either one or both dimensions. In contrast to the wavelet decomposition, where only the approximation coefficients are further decomposed, the wavelet packet decomposition takes all coefficients into account for further decomposition. Any additional level of decomposition is obtained by applying the operators  $\mathcal{A}$ ,  $\mathcal{D}_1$ ,  $\mathcal{D}_2$  and  $\mathcal{D}_3$  iteratively to both approximation coefficients  $a[k, l]$  and detail coefficients  $d_1[k, l]$ ,  $d_2[k, l]$  and  $d_3[k, l]$ . Thereby, a so-called full-tree decomposition of depth  $Z$  is defined as decomposition where all coefficients were decomposed  $Z$  times. At level  $Z$ , a full-tree decomposition possesses  $4^Z$  leaves. Each leaf represents a set of coefficients defining a down-sampled version of object  $O[k, l]$ . Thereby, the frequency content of every leaf corresponds to a distinct spectral band, where all spectral bands have approximately the same bandwidth. Furthermore, all leaves at level  $Z$  have the same number of coefficients, approximately determined by  $4^{-Z}KL$ . A full-tree decomposition for  $Z = 2$  can be seen in figure 7.4. A set of full-tree wavelet packets is often referred to as a pseudo-local cosine basis, as their frequency content is confined to a certain spectral band, yet collectively covering all frequencies.

Rosenthal et al. use the fact that the integral over an arc, used in the description of optoacoustic detection, locally approximates an integral along a line, which is at the basis of the formulation of the Radon-transform. Then, with rationale of the Radon transform, it can be shown that projection data of objects that are confined in their spatial and frequency domain (such as wavelets), can be localized in their sinogram when the projection operator locally approximates the Radon transform. Specifically, this finding implies, that objects which consist of a superposition of various translated wavelet packets, can be reconstructed from a projection dataset that is smaller than the one needed when no a priori information on the object is given.

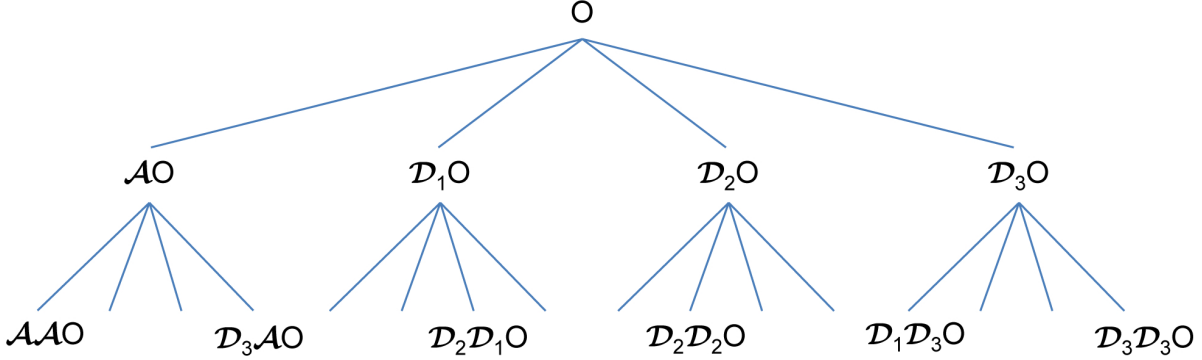


Figure 7.4: Full-tree wavelet packet decomposition of depth 2.

Now, for both the image  $\vec{H}$  and its projection data  $\vec{p}$ , a full-tree decomposition can be calculated. By doing so, image and projection data are decomposed in a wavelet packet base, where each base function has the same support in space and approximately the same effective support in frequency. Then, for each leaf in the tree, the projection dataset required for reconstructing the decomposition coefficients can be identified. Each set of wavelet packet coefficients demands a different piece of information of the projection data in order to be reconstructed correctly. In case where no overlap between information datasets for reconstructing different leaves occurs, the inversion problem may be efficiently divided into a set of smaller problems. This means that the wavelet packet coefficients of each leaf can be reconstructed independently from the coefficients of all other leaves.

In order to formulate image reconstruction in the wavelet domain, two column vectors,  $\vec{H}_W$  and  $\vec{p}_W$ , containing a full-tree decomposition of the image  $\vec{H}$  and pressure data  $\vec{p}$  are defined,

$$\vec{H}_W = \left[ (\vec{H}_W^1)^T, \dots, (\vec{H}_W^{4^Y})^T \right]^T, \quad (7.8)$$

$$\vec{p}_W = \left[ (\vec{p}_W^1)^T, \dots, (\vec{p}_W^{4^Z})^T \right]^T. \quad (7.9)$$

Here,  $\vec{H}_W^y$  denotes the column vector containing the wavelet packet coefficients of the image  $\vec{H}$ , corresponding to the  $y$ -th leaf. Likewise,  $\vec{p}_W^z$  represents the column vector with the wavelet packet coefficients of pressure data  $\vec{p}$ , associated with the  $z$ -th leaf.  $Y$  and  $Z$  are the respective depths of the decomposition. The lengths of the vectors defined in 7.8 and 7.9 are denoted by  $l_W^H$  and  $l_W^p$ . Then, wavelet reconstruction in the formulation of equation 7.7 can be written in matrix form as

$$\vec{H} = \mathcal{R} \cdot \vec{H}_W, \quad (7.10)$$

with matrix  $\mathcal{R}$  composed of  $4^Y$  sub-matrices, each representing a leaf

$$\mathcal{R} = \left[ \mathcal{R}^1, \dots, \mathcal{R}^{4^Y} \right]. \quad (7.11)$$

Therefore, the reconstruction formula may equivalently be written as

$$\vec{H} = \sum_{y=1}^{4^Y} \mathcal{R}^y \cdot \vec{H}_W^y. \quad (7.12)$$

Then, also the wavelet decomposition process can be represented by a matrix  $\mathcal{D}$ , leading to the following formulation

$$\vec{p}_W = \mathcal{D} \cdot \vec{p}. \quad (7.13)$$

Substituting 7.10 and 7.13 into matrix equation 4.40, representing the optoacoustic forward problem, yields

$$\vec{p}_W = \mathcal{D} \cdot \mathcal{M} \cdot \mathcal{R} \cdot \vec{H}_W, \quad (7.14)$$

the corresponding equation in the wavelet domain. Each wavelet packet, represented by a leaf  $y$ , defines a model matrix  $\mathcal{M}_W^y$  in the wavelet domain, calculated as

$$\mathcal{M}_W^y = \mathcal{D} \cdot \mathcal{M} \cdot \mathcal{R}^y. \quad (7.15)$$

Now, assuming that the representation in the wavelet packet basis is efficient, Rosenthal et al. showed that most rows in model matrix  $\mathcal{M}_W^y$  have little influence on an accurate prediction of the wavelet packet coefficients  $\vec{p}_W^y$  corresponding to the  $y$ -th leaf,

$$\vec{p}_W^y = \mathcal{M}_W^y \cdot \vec{H}_W^y. \quad (7.16)$$

Indeed, it is anticipated that a limited number of wavelet packet coefficients is sufficient to specify the projection data emitted from any object spanned by the  $y$ -th wavelet-packet base. Consequently, there is room to optimize memory consumption and calculation speed by only considering rows of the matrix which contain important information. As it can not be expected that the significant rows of  $\mathcal{M}_W^y$  solely correspond to a single wavelet packet, an upper limit  $LIM$  of rows taken into account is set. Then, a vector containing the maximum absolute value of each row of  $\mathcal{M}_W^y$  is built, and the  $LIM$  rows with the highest value are considered to be of significance. Considering only the selection of important rows yields a set of  $4^Y$  reduced model matrices  $\mathcal{M}_{W,LIM}^y$ , representing the optoacoustic forward problem decomposed into wavelet packets,

$$\vec{p}_{W,LIM}^y = \mathcal{M}_{W,LIM}^y \cdot \vec{H}_W^y. \quad (7.17)$$

$\vec{p}_{W,LIM}^y$  denotes the vector obtained from  $\vec{p}_W^y$  by considering only the  $LIM$  important rows of  $\mathcal{M}_W^y$ . As the matrices defining the inversion problems represented by equation 7.17 are considerably smaller than  $\mathcal{M}$ , more complex inversion algorithms can now be applied. When calculating a direct inverse, such as the Moore-Penrose-Pseudoinverse  $(\mathcal{M}_{W,LIM}^y)^\dagger$ , for each of the wavelet packets, inversion is reduced to a matrix multiplication,

$$\vec{H}_W^y = (\mathcal{M}_{W,LIM}^y)^\dagger \cdot \vec{p}_{W,LIM}^y. \quad (7.18)$$

Finally, according to equation 7.12, optoacoustic image reconstruction consists of performing an inverse discrete wavelet transform and summing the contribution of each of the  $4^Y$  wavelet packets,

$$\vec{H} = \sum_{y=1}^{4^Y} \mathcal{R}^y \cdot (\mathcal{M}_{W,LIM}^y)^\dagger \cdot \vec{p}_{W,LIM}^y. \quad (7.19)$$

### 7.2.2 Results with Simulated and Experimental Data

In order to showcase the potential of model-based image reconstruction in the wavelet domain, simulations and experiments have been conducted. To that end, analytical optoacoustic signals have been calculated for a tomographic detection geometry with 450 detectors equally positioned along a circumference of radius 4 cm. The ROI covered  $2 \times 2 \text{ cm}^2$ , discretized by  $151 \times 151$  pixels, resulting in a uniform resolution of approximately  $130 \mu\text{m}$ . Within the ROI, the two-dimensional distribution of truncated paraboloids used in section 5.3.1 was considered as optical absorbers (figure 7.5 (a)). In order to evaluate the performance of the model transfer to the wavelet domain, the detectors were assumed to be confined to points. Figure 7.5 (b) shows the reconstruction obtained by inverting the matrix vector equation of the IMMI algorithm using model matrix  $\mathcal{M}$ . All absorbers are correctly reconstructed, as the model matrix fits the measurement geometry. Figure 7.5 (c) depicts the reconstruction calculated with equation 7.19 after decomposing the imaging problem into 16 sub-problems in the wavelet domain. Also here, all optical absorbers are correctly reconstructed, exhibiting only minor flaws around the biggest absorber which could be removed by recursively improving the reconstruction with the procedure described in [101]. Inversion in the case of the IMMI algorithm was performed with the LSQR algorithm and took approximately 10 seconds per image. This value could be reduced to less than 5 seconds by using the wavelet packet approach of equation 7.19. Holding model matrix  $\mathcal{M}$  in storage required 730 MB of memory whereas the Moore-Penrose-Pseudoinverse  $(\mathcal{M}_{W,LIM}^y)^\dagger$  only occupied less than 260 MB. Beyond that, in contrast to model matrix  $\mathcal{M}$  the direct inversion matrices  $(\mathcal{M}_{W,LIM}^y)^\dagger$  are already densely populated. In the case, when geometric detector properties are incorporated into the imaging model, memory requirements for both model matrices  $\mathcal{M}_{sum}$  and  $\mathcal{M}_{SIR}$  increase up to a factor of 10. However, even with detector properties included, the size of the wavelet domain sub-problems cannot increase any more.

The simulation results with a more complex absorption distribution obtained from a photograph of mouse cross-section can be seen in figure 7.5 (d) – (f). Optoacoustic pressure signals were generated by multiplying the absorption pattern in 7.5 (d) with the model matrix  $\mathcal{M}$ . In order to avoid an inverse crime, Gaussian white noise with zero mean and standard deviation of 10 % of the maximum amplitude was added to the projection data. The reconstruction obtained with the IMMI algorithm can be seen in figure 7.5 (e) and shows, as expected, a minimal noise floor over the entire image. The result of the wavelet domain algorithm is depicted in sub-figure 7.5 (f). The image quality is almost identical to the result of the IMMI algorithm, showing only slightly more negative values.

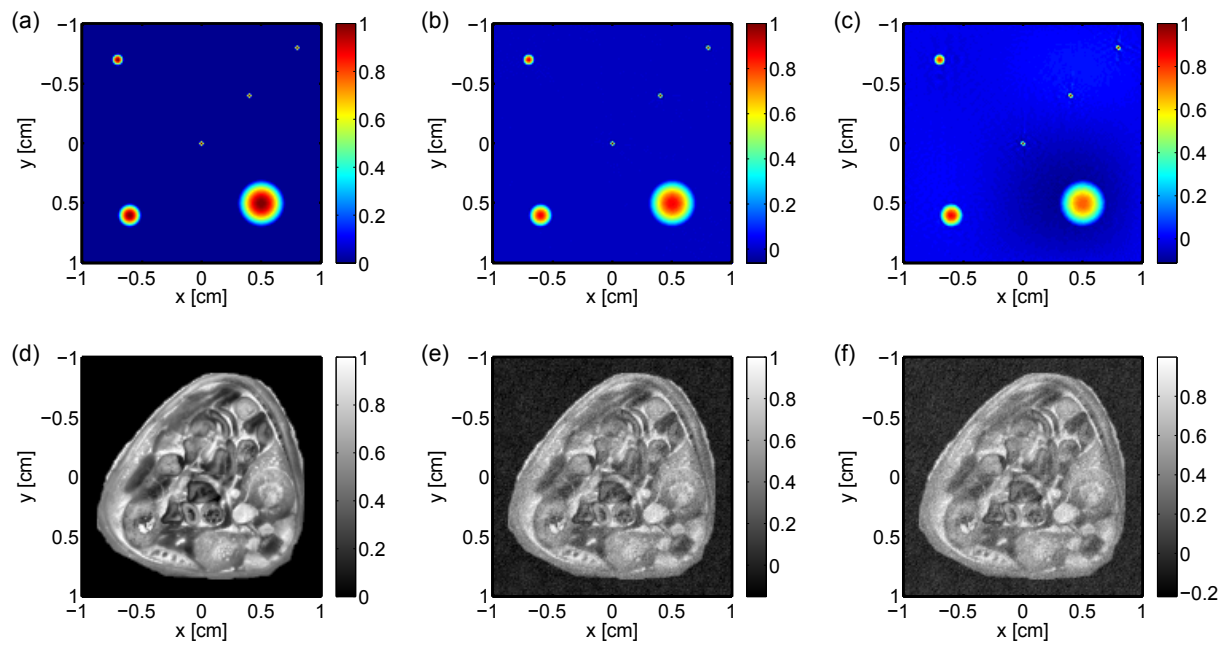


Figure 7.5: (a) Theoretical image composed by truncated paraboloids of different sizes. (b) Reconstruction obtained by the IMMI algorithm. (c) Wavelet packet reconstruction. (d) Photograph of a mouse cross-section used for signal generation. (e) Model-based image reconstruction after the addition of Gaussian white noise. (f) Reconstruction obtained by the wavelet domain algorithm.

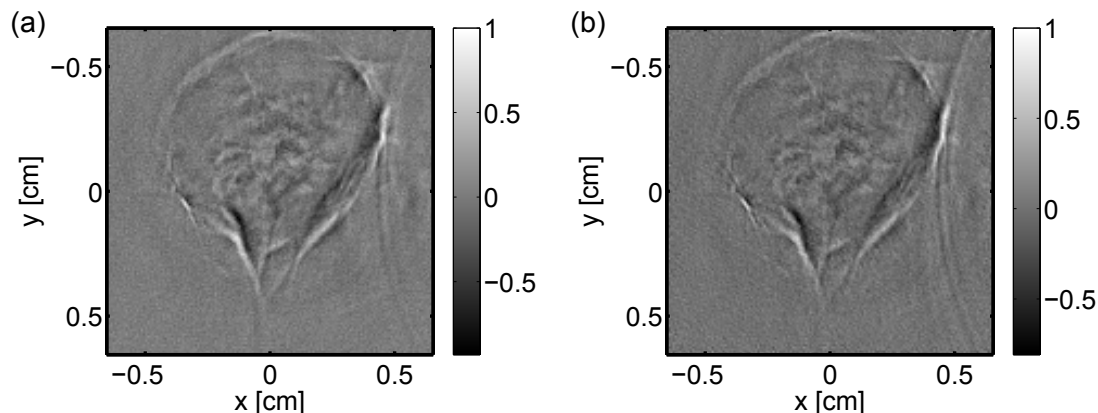


Figure 7.6: (a) Reconstruction obtained by the IMMI algorithm. (b) Reconstruction resulting from the wavelet domain algorithm.

As the simulation results proved the wavelet domain algorithm's ability to reconstruct optoacoustic images, a tomographic data-set of a mouse tumor was acquired with the imaging system presented in section 3.4.1. The experiment considered 500 equally spaced detector positions on a circumference of radius approximately 2.6 cm. The ROI covered  $1.3 \times 1.3 \text{ cm}^2$  and was discretized with  $151 \times 151$  pixels. Figure 7.6 shows in sub-figure (a) the result of the reconstruction with the IMMI algorithm and in sub-figure (b) the result of the wavelet packet algorithm. No visible difference can be observed, showcasing the applicability of the wavelet packet framework for optoacoustic image reconstructions of experimental data. Again, calculation time of the wavelet packet algorithm was less than half as compared to the IMMI algorithm.

All reconstructions using the wavelet-packet framework applied a full-tree decomposition of depth 2 to image and data space. The Daubechies 6 wavelet was chosen as mother wavelet, corresponding to conjugate mirror filters with six coefficients. All calculations were performed in MATLAB (Mathworks, Natick, MA, USA) on a personal computer with an Intel Duo 3-GHz processor and 16 GB of RAM.

### 7.2.3 Wavelet Packets in Three Dimensions

The theory developed in subsection 7.2.1 can be conceptually extended to three dimensions. In this case, the image to be reconstructed defines a volume consisting of voxels in the image space,  $\vec{H} \in \mathcal{I}$ . The optoacoustic measurements, as element of the projection space  $\vec{p} \in \mathcal{P}$ , have to be arranged in a three-dimensional sinogram, where two dimensions define the spatial position of the detector and the third dimension represents the time axis. Then, a first level three-dimensional wavelet decomposition of an object  $O[e, f, g]$ , ( $e = 1, \dots, E; f = 1, \dots, F; g = 1, \dots, G$ ) is defined as

$$a[e, f, g] = \mathcal{A}O[u, v, w] = \sum_{u, v, w=-\infty}^{\infty} h[u - 2e]h[v - 2f]h[w - 2g]O[u, v, w], \quad (7.20)$$

$$d^1[e, f, g] = \mathcal{D}^1O[u, v, w] = \sum_{u, v, w=-\infty}^{\infty} g[u - 2e]h[v - 2f]h[w - 2g]O[u, v, w], \quad (7.21)$$

$$d^2[e, f, g] = \mathcal{D}^2O[u, v, w] = \sum_{u, v, w=-\infty}^{\infty} h[u - 2e]g[v - 2f]h[w - 2g]O[u, v, w], \quad (7.22)$$

$$d^3[e, f, g] = \mathcal{D}^3O[u, v, w] = \sum_{u, v, w=-\infty}^{\infty} h[u - 2e]h[v - 2f]g[w - 2g]O[u, v, w], \quad (7.23)$$

$$d^4[e, f, g] = \mathcal{D}^4O[u, v, w] = \sum_{u, v, w=-\infty}^{\infty} h[u - 2e]g[v - 2f]g[w - 2g]O[u, v, w], \quad (7.24)$$

$$d^5[e, f, g] = \mathcal{D}^5O[u, v, w] = \sum_{u, v, w=-\infty}^{\infty} g[u - 2e]h[v - 2f]g[w - 2g]O[u, v, w], \quad (7.25)$$

$$d^6[e, f, g] = \mathcal{D}^6O[u, v, w] = \sum_{u, v, w=-\infty}^{\infty} g[u - 2e]g[v - 2f]h[w - 2g]O[u, v, w], \quad (7.26)$$

$$d^7[e, f, g] = \mathcal{D}^7O[u, v, w] = \sum_{u, v, w=-\infty}^{\infty} g[u - 2e]g[v - 2f]g[w - 2g]O[u, v, w]. \quad (7.27)$$

(Note that  $g$  is both used as variable and operator. From the context it is clear if  $g$  is either variable or operator.) Here, operators  $\mathcal{A}, \mathcal{D}^1, \dots, \mathcal{D}^7$  yield the three-dimensional approximation coefficients  $a[e, f, g]$  and detail coefficients  $d^1[e, f, g], \dots, d^7[e, f, g]$ . Three-

dimensional wavelet reconstruction, on the other side, is performed by the formula

$$\begin{aligned}
O[e, f, g] = & \sum_{u,v,w=-\infty}^{\infty} h[e-2u]h[f-2v]h[g-2w]a[u, v, w] \\
& + \sum_{u,v,w=-\infty}^{\infty} g[e-2u]h[f-2v]h[g-2w]d^1[u, v, w] \\
& + \sum_{u,v,w=-\infty}^{\infty} h[e-2u]g[f-2v]h[g-2w]d^2[u, v, w] \\
& + \sum_{u,v,w=-\infty}^{\infty} h[e-2u]h[f-2v]g[g-2w]d^3[u, v, w] \\
& + \sum_{u,v,w=-\infty}^{\infty} h[e-2u]g[f-2v]g[g-2w]d^4[u, v, w] \\
& + \sum_{u,v,w=-\infty}^{\infty} g[e-2u]h[f-2v]g[g-2w]d^5[u, v, w] \\
& + \sum_{u,v,w=-\infty}^{\infty} g[e-2u]g[f-2v]h[g-2w]d^6[u, v, w] \\
& + \sum_{u,v,w=-\infty}^{\infty} g[e-2u]g[f-2v]g[g-2w]d^7[u, v, w].
\end{aligned} \tag{7.28}$$

As in the two-dimensional case,  $a[e, f, g]$  represents a three-dimensional, down-sampled and low-passed version of object  $O[e, f, g]$ . Furthermore,  $d^1[e, f, g], \dots, d^7[e, f, g]$  denote down-sampled and high-passed versions over either one, two or all three dimensions. A three-dimensional full-tree decomposition of depth  $Z$  possesses  $8^Z$  leaves, with each leaf having approximately  $8^{-Z} EFG$  coefficients.

In two dimensions, the ideal case of a full-view scenario with uniformly distributed projections spanning all  $360^\circ$  of a detection circumference was considered. Then, projection data can be straightforwardly represented by its sinogram, where neighboring columns correspond to signals measured at adjacent detector positions. In three dimensions, a full-view detection geometry would be represented by transducers covering a sphere. Out of practical reasons it is not convenient to entirely enclose the ROI by the detection system as the positioning of samples or anesthesia hoses for *in-vivo* measurements require access which cannot be occupied by a detection system. Furthermore, the wavelet domain algorithm requires the representation of the pressure data in a three-dimensional sinogram, which can be subsequently decomposed by means of the three-dimensional wavelet packet transform (equations 7.20 - 7.27). Obviously, projection data can be represented by spherical coordinates, where two axes of the sinogram correspond to polar and azimuth angle, whereas the third axis represents the temporal dimension of the signal. However, positioning transducers equally on a sphere, in a way that the corresponding sinogram maintains the connection

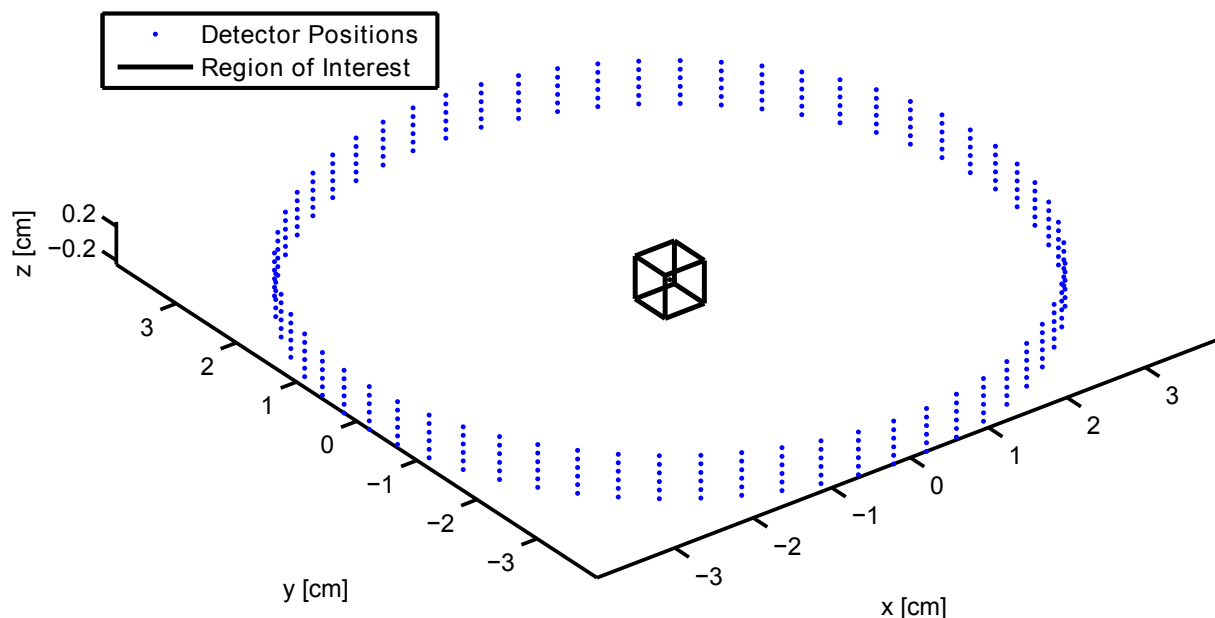


Figure 7.7: Cylindrical detection geometry for the simulations with the three-dimensional model-based reconstruction algorithm in the wavelet domain. Every tenth detection ring is depicted in the figure.

of neighboring projections, is not a trivial task.

Less complex is the application of a cylindrical detection geometry, which results from scanning a detection ring in the elevational direction. Here, a uniform coverage of the detection surface is readily obtained from the two-dimensional case. Projection data in the three-dimensional sinogram is represented by the azimuth angle, the height determining the position of each detector and the time axis as the third dimension.

In order to illustrate the performance of the wavelet packet algorithm in three dimensions, numerical simulations have been conducted. To that end, a ROI of  $51 \times 51 \times 51$  voxels covering  $5 \times 5 \times 5 \text{ mm}^3$  was considered. For each of the 51 planes of the ROI, optoacoustic measurements were acquired on a detection circumference of radius 4 cm. Measurements were recorded every  $6^\circ$  spanning all the  $360^\circ$  of each circle so that overall 3060 detector positions were taken into account. The ROI and cylindrical detection geometry can be seen in figure 7.7. In the center of the ROI a wavelet has been positioned as the image to be reconstructed (figure 7.9 (a) and (d)). In order to generate optoacoustic signals and to execute the model-based IMMI algorithm a three-dimensional model matrix has been calculated, capturing all 3060 detector positions. Optoacoustic pressure signals  $\vec{p}$  have been generated according to mapping 7.1 by multiplying the model matrix  $\mathcal{M}$  by the vectorized ROI  $\vec{H}$ . Again, in order to avoid the inverse crime, Gaussian white noise with zero mean and standard deviation of 10% of the maximum amplitude was added to the projection data. The resulting matrix vector equation has been inverted by means of the LSQR algorithm and its MIP along the z- and y-axis is depicted in figure 7.9 (b)

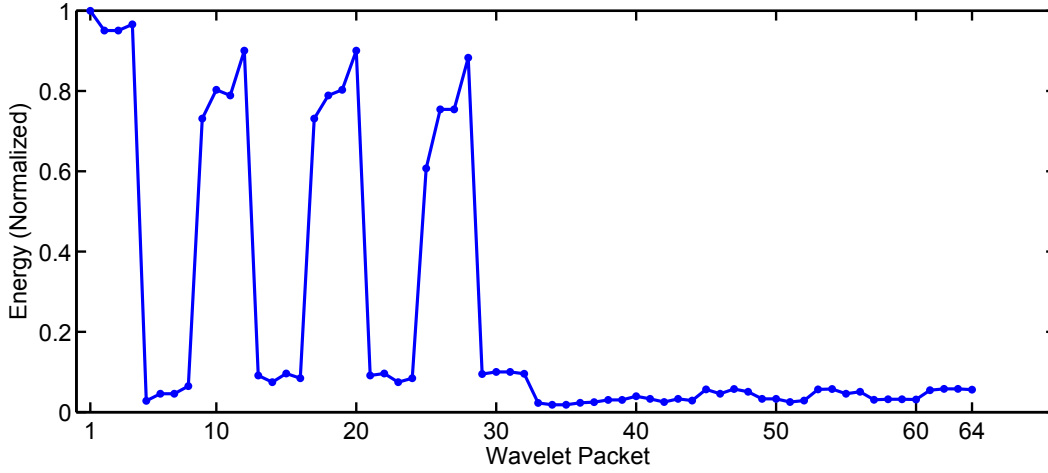


Figure 7.8: Normalized energy of the pressure signals generated by the 64 wavelet packets positioned at the center of the ROI.

and (e). Within the xy-plane the original image is accurately reconstructed showing all distinct peaks. However, as there are no detectors positioned on top or bottom of the ROI, resolution along the z-axis is strongly affected, resulting in severe out-of-plane artifacts. The reconstruction is smeared almost over the entire ROI.

Model-based inversion in the wavelet domain has been performed by decomposing the inversion problem into a set of 64 sub-problems in the wavelet domain, resulting from a decomposition of depth  $Z = 2$ . Yet, as all of the 64 wavelet packets possess directionality, not all of them are sufficiently captured by the cylindrical detection geometry of figure 7.7. This can be shown by placing all 64 wavelet packets  $\vec{H}_{WP^i}$ , ( $i = 1, \dots, 64$ ) at the center of the ROI and calculating the optoacoustic pressure  $\vec{p}_{WP^i}$  generated by them according to mapping 7.1. Now, to assess the impact of each wavelet packet on the reconstruction, the energy of the 64 pressure signals is calculated according to

$$E_{WP}^i = \|\vec{p}_{WP^i}\|_2, \quad i = 1, \dots, 64, \quad (7.29)$$

and can be seen in figure 7.8. As more than half of the wavelet packets do not generate information than can be captured by the cylindrical detection geometry, the corresponding sub-problems with an energy  $E_{WP}^i$  below the threshold  $THR$  of 10% of the maximum energy are not considered for inversion. In fact, these sub-problems effectively pose a limited view problem and are ill-conditioned as can be seen by inspecting their condition number.

Eventually, 16 sub-problems were identified as having crucial impact on the reconstruction. For all of them, in analogy to equation 7.19, a Moore-Penrose-Pseudoinverse  $(\mathcal{M}_{W,LIM}^y)^\dagger$  has been calculated and the reconstruction  $\vec{H}$  was obtained according to

$$\vec{H} = \sum_{y=1}^{64} \mathcal{R}^y \cdot (\mathcal{M}_{W,LIM}^y)^\dagger \cdot \vec{p}_{W,LIM}^y, \quad \forall y : E_{WP}^y > THR. \quad (7.30)$$

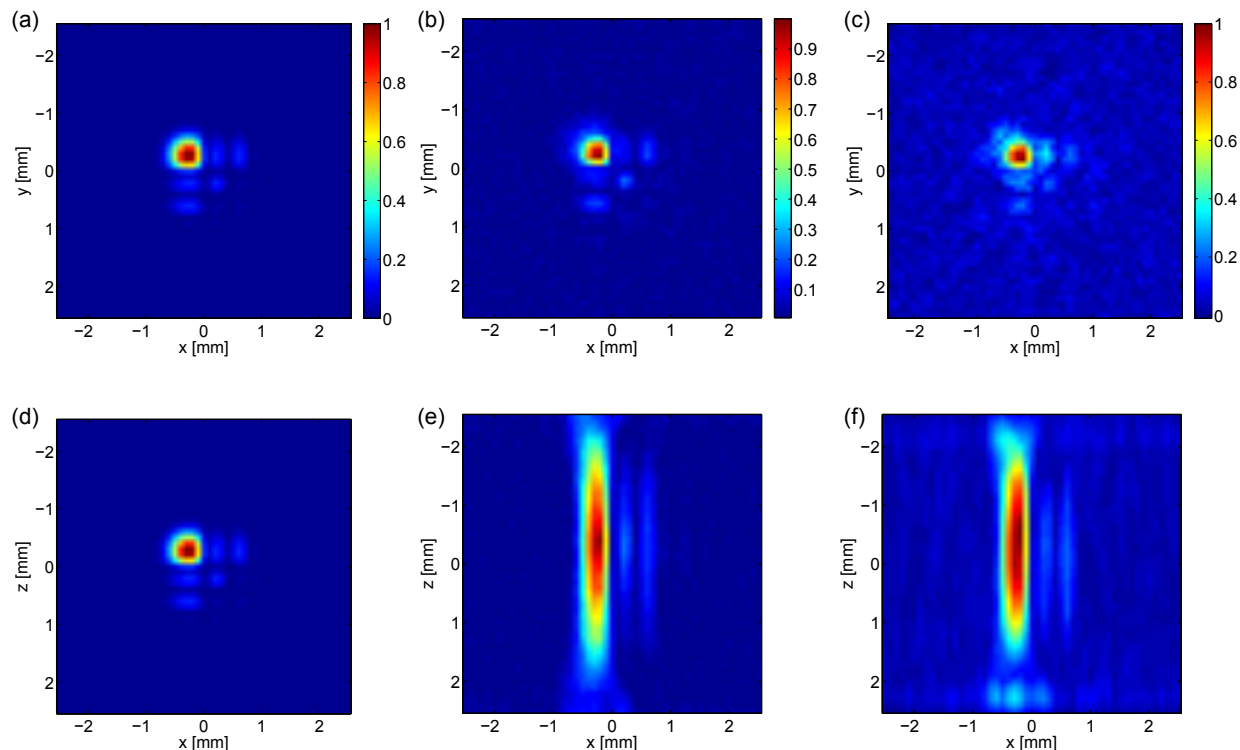


Figure 7.9: (a) MIP along the  $z$ -axis of the wavelet to be reconstructed. (b) MIP obtained from the IMMI algorithm. (c) Corresponding MIP obtained from the wavelet domain algorithm. (d) MIP along the  $y$ -axis of the original wavelet. (e) MIP of the reconstruction resulting from the IMMI algorithm. (f) MIP along the  $y$ -axis resulting from the wavelet domain algorithm.

The reconstruction obtained by equation 7.30 can be seen in figure 7.9 (c) and (f). Except for a slightly higher background noise level, the MIP along the  $z$ -axis shows all details of the expected image. In agreement with the reconstruction obtained from the IMMI algorithm, the wavelet domain reconstruction exhibits a loss of the resolution in  $z$ -direction owing to the lack of detector coverage.

Image reconstruction with the IMMI algorithm took 380 seconds and required the inversion of a matrix system occupying more than 30 GB of memory. In contrast, inversion in the wavelet domain was reduced to a summation and a set of matrix vector multiplications which took around 90 seconds. Holding a Moore-Penrose-Pseudoinverse ( $\mathcal{M}_{W,LIM}^y$ )<sup>†</sup> in storage required approximately 13 GB of memory. All three-dimensional image reconstructions were executed on a workstation computer with Intel Xeon processors and 384 GB of RAM.

### 7.2.4 Concluding Remarks

In this section, strategies to improve the performance of model-based image reconstruction were presented, focusing on memory reduction and faster reconstruction times. Thereby, in a first step, symmetries in the detection geometry were exploited to significantly minimize the memory consumption. Then, an entirely new framework to perform model-based inversion in the wavelet domain was introduced. Overall, transferring model-based optoacoustic image reconstruction to the wavelet domain reduced the size of the inversion problem, resulting in a set of smaller problems. By doing so, more complex inversion algorithms, such as calculating the Moore-Penrose-Pseudoinverse, applying  $\ell_1$ - or  $\ell_2$ -norm based minimization algorithms or a SVD of the model matrices, could be considered for inversion. Furthermore, once all direct inverse matrices had been calculated, as in equations 7.19 and 7.30, image reconstruction could be performed significantly faster than by an iterative inversion algorithm. Moreover, all modeling advantages of algebraic reconstruction algorithms are available for the wavelet packet framework and can readily be included.

# Chapter 8

## Conclusion and Outlook

### 8.1 Conclusive Summary

The present work introduced advanced image reconstruction techniques for optoacoustics. Particular emphasis was given to model-based reconstruction algorithms incorporating geometric detector properties for three-dimensional optoacoustic tomography. After establishing the theoretical background of ultrasonic transducers, two approaches to model their detection surfaces were implemented and evaluated. Thereby, the benefits of the enhanced imaging model could be shown both theoretically in computer simulations and within experimental measurements of Agar phantoms and biological tissue. Increasing computational demands were encountered with memory efficiency techniques based on symmetries in the detection geometry. Significant improvement in reconstruction times could be achieved by transferring the imaging model to the wavelet domain, which furthermore enabled the application of complex inversion algorithms. In addition, this work proved, conceptually and experimentally, the feasibility to reconstruct cross-sectional images from pressure data optoacoustically generated with a cw-laser tomography system.

There exists a considerable variety of approaches to reconstruct images in optoacoustics. Analytical inversion algorithms, both in time and frequency domain, bear inherent simplicity which makes them numerically very fast with minimal memory requirements. A crucial factor, contributing to their convenience, consists of the basic imaging model they are built upon. In general, analytic inversion algorithms merely consider the sound propagation by means of the wave equation as their imaging model. However, with increasing demands regarding accuracy and quantifiability of optoacoustic images, more sophisticated imaging models need to be applied for reconstruction. This development paved the way for the success of algebraic inversion algorithms, also termed model-based reconstruction algorithms. Their key advantage is the possibility to include any linearizable physical effect into the imaging model. As a consequence, optoacoustic images reconstructed by them provide superior image quality and fidelity at the price of increased memory requirements and calculation times.

A major contribution to image quality comes from an accurate model of the ultrasonic detection system. In general, optoacoustic imaging models assume ultrasonic detectors to be confined to points in space. Yet, a majority of optoacoustic imaging systems use ultrasound detection technology based on piezoelectricity. In effect, larger detection surfaces signify higher SNR. Moreover, piezoelectric materials offer the possibility to be manufactured forming a focus. By doing so, pressure signals can be measured only from selective regions, conveniently reducing the dimension of the imaging problem. The discrepancy between actual detection surface geometry and point-like transducers assumed in the imaging model is the cause for severe imaging artifacts. By properly modeling the detection surface of a cylindrically focused transducer within a model-based reconstruction algorithm, this work proved, that imaging artifacts related to the transducer's geometry can be significantly mitigated. In particular, resolution in all spatial dimensions could be improved, enabling localization and quantification even of small absorbers. The experimental results showed furthermore, that an imaging model including geometric detector properties abates the background noise floor present in optoacoustic reconstructions.

When holding the model matrix of an algebraic inversion algorithm in storage, more complex imaging models come along with higher memory requirements. This effect becomes even more significant if high-resolution volumetric reconstructions are demanded. In this work, I developed and implemented memory efficiency techniques that are based on symmetries in the detection geometry. In particular, tomographic signal acquisition along a cylindrical detection surface possesses symmetries within each detection plane and along the elevational direction. Combining potential memory savings in all spatial dimensions potentially reduces the size of the model matrix by a factor of more than 10. Consequently, taking advantage of memory saving strategies enables model-based reconstruction algorithms to process larger, high-resolution datasets.

Essentially, there are inversion schemes, that calculate the action of the matrix on a vector on the fly, thus avoiding to hold a large model matrix in storage. However, this process is very time consuming, especially when an iterative inversion algorithm requires a high number of iteration steps to converge. In addition, large model matrices hinder the calculation of direct inversion matrices or the application of sophisticated inversion algorithms based on calculating a SVD or minimizing the  $\ell_1$ -norm. In order to address the problem of increasing model matrices, a framework for model-based image reconstructions using wavelet packets was introduced in this work. Decomposition of the data and image space by means of a discrete wavelet transform divided the large imaging model into a set of smaller inversion problems, each corresponding to a wavelet packet. In consequence, also complex inversion procedures could be applied to the set of small inversion problems. When calculating the Moore-Penrose-Pseudoinverse as a direct inverse, in two dimensions, it could be shown that even reconstruction times decreased by a factor of more than two.

## 8.2 Outlook and Future Directions

Model-based image reconstruction has proven to provide superior image quality over any existing reconstruction algorithm in optoacoustics. However, this performance comes at the price of increased computational demands. Today, depending on the actual application, a trade-off between image quality and reconstruction time has to be made and is reflected in the complexity of the chosen imaging model.

Image reconstruction algorithms are commonly first developed in the time domain, which facilitates an intuitive understanding of the imaging model. Yet, frequency domain algorithms, as presented in section 4.1.2, offer the computational advantages inherent to Fast Fourier Transform techniques. As a next step, it is expected, that benefits of Fast Fourier Transforms can be translated to model-based reconstruction algorithms. Optoacoustic signal generation is predominately performed by pulsed lasers, approximating a Dirac-delta source term, which excites a broad-band pressure wave. This setting is reflected by the imaging model in form of the wave equation Cauchy problem. In contrast, cw-laser optoacoustic systems offer the degree of freedom to selectively apply an excitation term covering a designated frequency band or even single frequencies. Then, the excitation term can be an overlay of several modulation frequencies corresponding to the size of absorbers one wants to highlight in the image. Thereby, the selected excitation frequencies act as a spatial frequency focus on the image. In combination with a dedicated frequency domain model-based reconstruction algorithm, cw-laser systems potentially generate optoacoustic images providing concerted, detailed information.

Another promising direction is the development of the wavelet domain framework. The extension of the presented algorithm to three dimensions is an active field of work and bears the potential to apply a complex imaging model in combination with sophisticated inversion algorithms. Thereby, several complications arising in three dimension have to be overcome. A crucial requirement is the equal distribution of transducers over a spherical detection geometry, which is not a straightforward task. Moreover, as realistic optoacoustic systems do not entirely enclose the ROI, only part of the generated pressure waves is actually detected. As also wavelets possess inherent directionality, not all inversion sub-problems, each corresponding to a wavelet packet, need to be taken into account. In fact, the inversion sub-problem of wavelet packets generating information which is not covered by the detection geometry, is expected to be badly conditioned. It would therefore merely amplify noise and deteriorate the image reconstruction. In effect, the development of a three-dimensional wavelet packet framework is substantially more complex than the two-dimensional case.

During the last decades, computational hardware was subject to continuous development and improvements, enabling the handling of large datasets and the execution of complex reconstruction algorithms. Especially the availability of increasingly powerful GPUs provides the possibility to accelerate demanding calculations.



# Appendix A

## Analytical Pressure Formulas

Pressure waves, optoacoustically induced by delta-pulse excitation, can be described by equation 2.72. In the following two chapters, the solution of equation 2.72 are calculated analytically for the case of a two- and three-dimensional absorber. In each dimension, the cases of a parabolic and a uniform absorption pattern  $H_r(\vec{r})$  are considered.

### A.1 Analytical Pressure Formulas in 2D

#### A.1.1 Parabolic Absorption

In the case when optical absorbers are assumed to be confined to a plane, the three-dimensional problem 2.53 - 2.55 can be reduced to two dimensions. Therefore, equation 2.72, the representation of optoacoustically induced pressure  $p$  as a function of spatially varying absorption  $H_r$ , is simplified to

$$p(\vec{r}, t) = \frac{\Gamma}{4\pi} \frac{\partial}{\partial t} \iint_{|\vec{r}-\vec{r}'|=c_s t} \frac{H_r(\vec{r}')}{|\vec{r}-\vec{r}'|} d\vec{r}' \quad (\text{A.1})$$

$$= \frac{\Gamma}{4\pi} \frac{\partial}{\partial t} \oint_{|\vec{r}-\vec{r}'|=c_s t} \frac{H_r(\vec{r}')}{|\vec{r}-\vec{r}'|} dl(\vec{r}'). \quad (\text{A.2})$$

Here,  $\vec{r} = (x, y)^T \in \mathbb{R}^2$  is a two-dimensional vector in space. The integral in A.2 is now reduced to a line integral over the circle with radius  $c_s t$  and center  $\vec{r}$ . The scalar line element is denoted by  $dl(\vec{r})$ . Figure A.1 (a) shows the parabolic absorption pattern  $H_r$  under consideration. It is defined by

$$H_r(x, y) = \begin{cases} 1 - \frac{(x-x_0)^2 + y^2}{r_0^2}, & (x-x_0)^2 + y^2 \leq r_0^2, \\ 0, & (x-x_0)^2 + y^2 > r_0^2, \end{cases} \quad (\text{A.3})$$

with  $r_0$  being the radius of the absorbing circle. Without loss of generality, the center of the absorber is assumed to lie on the x-axis. Furthermore, the detector position is assumed

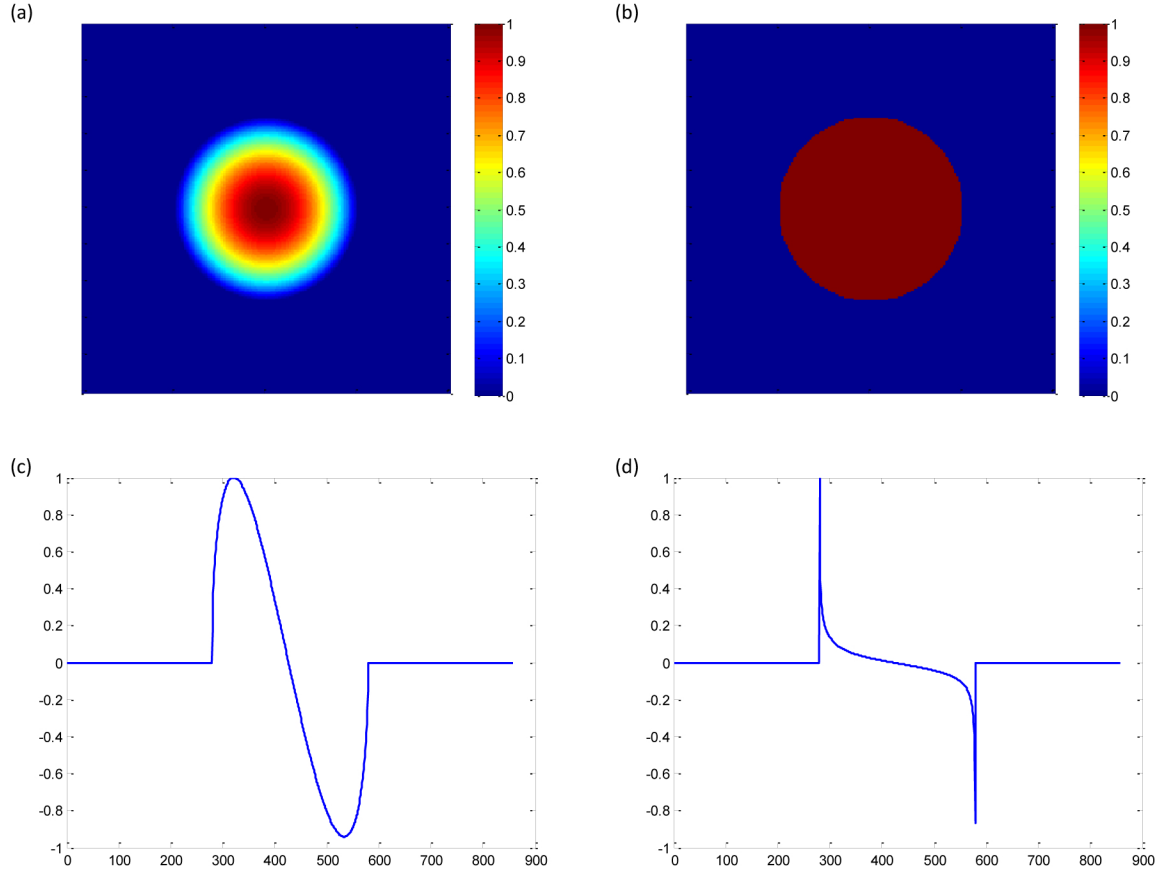


Figure A.1: (a) Parabolic absorption pattern. (b) Uniform absorption pattern. (c) Analytical signal emitted by a truncated paraboloid. (d) Analytical signal emitted by a uniform, circular absorption pattern.

to be at the origin,  $\vec{r} = (0, 0)^T$ , simplifying equation A.2 to

$$p\left(\begin{pmatrix} 0 \\ 0 \end{pmatrix}, t\right) = \frac{\Gamma}{4\pi} \frac{\partial}{\partial t} \oint_{|\vec{r}'|=c_s t} \frac{H_r(\vec{r}')}{c_s t} dl(\vec{r}'). \quad (\text{A.4})$$

$x_i$  and  $y_i$  define the coordinates in the xy-plane where the detection circumference with radius  $c_s t$  intersects the circular absorber with radius  $r_0$ . They can be calculated as

$$x_i = \frac{x_0^2 + c_s^2 t^2 - r_0^2}{2x_0}, \quad (\text{A.5})$$

$$y_i = \sqrt{c_s^2 t^2 - x_i^2} = \sqrt{c_s^2 t^2 - \frac{(x_0^2 + c_s^2 t^2 - r_0^2)^2}{4x_0^2}}. \quad (\text{A.6})$$

The line over which the integral is calculated can then be parametrized by the two mappings

$$\Psi_{\pm} : \begin{cases} [x_i, c_s t] & \longrightarrow & \mathbb{R}^2, \\ x & \longmapsto & \begin{pmatrix} x \\ \pm \sqrt{c_s^2 t^2 - x^2} \end{pmatrix}. \end{cases} \quad (\text{A.7})$$

The scalar line element is then given by

$$dl(\vec{r}) = \left\| \frac{d}{dx} \Psi_{\pm}(x) \right\| dx = \frac{c_s t}{\sqrt{c_s^2 t^2 - x^2}} dx. \quad (\text{A.8})$$

As both the detection arc and the circular absorber are symmetric with respect to the x-axis, it is sufficient to consider only two times the positive part  $\Psi_+$  of the parametrization. Therefore, inserting parametrization A.7 into equation A.4 leads to

$$\begin{aligned} p\left(\begin{pmatrix} 0 \\ 0 \end{pmatrix}, t\right) &= \frac{\Gamma}{4\pi} \frac{\partial}{\partial t} \oint_{|\vec{r}'|=c_s t} \frac{H_r(\vec{r}')}{c_s t} dl(\vec{r}') \\ &= \frac{\Gamma}{4\pi} \frac{\partial}{\partial t} 2 \int_{x_i}^{c_s t} \frac{1}{c_s t} \left( 1 - \frac{(x - x_0)^2 + (\sqrt{c_s^2 t^2 - x^2})^2}{r_0^2} \right) \frac{c_s t}{c_s^2 t^2 - x^2} dx \\ &= \frac{\Gamma}{2\pi} \frac{\partial}{\partial t} \int_{x_i}^{c_s t} \left( 1 - \frac{x^2 - 2xx_0 + x_0^2 + c_s^2 t^2 - x^2}{r_0^2} \right) \frac{1}{c_s^2 t^2 - x^2} dx \\ &= \frac{\Gamma}{2\pi} \frac{\partial}{\partial t} \left\{ \left( 1 - \frac{x_0^2 + c_s^2 t^2}{r_0^2} \right) \int_{x_i}^{c_s t} \frac{1}{\sqrt{c_s^2 t^2 - x^2}} dx + 2 \frac{x_0}{r_0^2} \int_{x_i}^{c_s t} \frac{x}{\sqrt{c_s^2 t^2 - x^2}} dx \right\}. \end{aligned} \quad (\text{A.9})$$

Taking the anti-derivative further gives

$$\begin{aligned} p\left(\begin{pmatrix} 0 \\ 0 \end{pmatrix}, t\right) &= \frac{\Gamma}{2\pi} \frac{\partial}{\partial t} \left\{ \left( 1 - \frac{x_0^2 + c_s^2 t^2}{r_0^2} \right) \left[ \arcsin\left(\frac{x}{c_s t}\right) \right]_{x_i}^{c_s t} + 2 \frac{x_0}{r_0^2} \left[ -\sqrt{c_s^2 t^2 - x^2} \right]_{x_i}^{c_s t} \right\} \\ &= \frac{\Gamma}{2\pi} \frac{\partial}{\partial t} \left\{ \left( 1 - \frac{x_0^2 + c_s^2 t^2}{r_0^2} \right) \left( \frac{\pi}{2} - \arcsin\left(\frac{x_i}{c_s t}\right) \right) + 2 \frac{x_0}{r_0^2} \sqrt{c_s^2 t^2 - x_i^2} \right\} \\ &= \frac{\Gamma}{2\pi} \frac{\partial}{\partial t} \left\{ \frac{r_0^2 - x_0^2}{r_0^2} \frac{\pi}{2} - \frac{c_s^2 \pi}{2r_0^2} t^2 - \frac{r_0^2 - x_0^2}{r_0^2} \arcsin\left(\frac{x_i}{c_s t}\right) \right. \\ &\quad \left. + \frac{c_s^2}{r_0^2} t^2 \arcsin\left(\frac{x_i}{c_s t}\right) + \frac{2x_0}{r_0^2} \sqrt{c_s^2 t^2 - x_i^2} \right\}. \end{aligned} \quad (\text{A.10})$$

Now, by taking the derivative with respect to  $t$  one gets

$$\begin{aligned}
p\left(\begin{pmatrix} 0 \\ 0 \end{pmatrix}, t\right) &= \frac{\Gamma}{2\pi} \left\{ -\frac{c_s^2 \pi}{r_0^2} t - \frac{r_0^2 - x_0^2}{r_0^2} \frac{1}{\sqrt{1 - \left(\frac{x_i}{c_s t}\right)^2}} \frac{\frac{\partial x_i}{\partial t} c_s t - c_s x_i}{c_s^2 t^2} \right. \\
&\quad + \frac{2c_s^2}{r_0^2} t \arcsin\left(\frac{x_i}{c_s t}\right) + \frac{c_s^2}{r_0^2} t^2 \frac{1}{\sqrt{1 - \left(\frac{x_i}{c_s t}\right)^2}} \frac{\frac{\partial x_i}{\partial t} c_s t - c_s x_i}{c_s^2 t^2} \\
&\quad \left. + \frac{2x_0}{r_0^2} \frac{1}{\sqrt{c_s^2 t^2 - x_i^2}} \left( c_s^2 t - x_i \frac{\partial x_i}{\partial t} \right) \right\}. \tag{A.11}
\end{aligned}$$

Notice that  $x_i$  depends on time  $t$ . Further simplification leads to

$$\begin{aligned}
p\left(\begin{pmatrix} 0 \\ 0 \end{pmatrix}, t\right) &= \frac{\Gamma}{2\pi} \left\{ -\frac{c_s^2 \pi}{r_0^2} t + \frac{2c_s^2}{r_0^2} t \arcsin\left(\frac{x_i}{c_s t}\right) + \left( \frac{c_s^2}{r_0^2} t^2 - \frac{r_0^2 - x_0^2}{r_0^2} \right) \frac{\frac{\partial x_i}{\partial t} - \frac{x_i}{t}}{\sqrt{c_s^2 t^2 - x_i^2}} \right. \\
&\quad \left. + \frac{2x_0}{r_0^2} \frac{1}{\sqrt{c_s^2 t^2 - x_i^2}} \left( c_s^2 t - x_i \frac{\partial x_i}{\partial t} \right) \right\}. \tag{A.12}
\end{aligned}$$

With A.5 one can transform

$$\frac{c_s^2}{r_0^2} t^2 - \frac{r_0^2 - x_0^2}{r_0^2} = \frac{c_s^2 t^2 - r_0^2 + x_0^2}{r_0^2} = \frac{2x_0}{r_0^2} x_i \tag{A.13}$$

in equation A.12. This results in

$$\begin{aligned}
p\left(\begin{pmatrix} 0 \\ 0 \end{pmatrix}, t\right) &= \frac{\Gamma}{2\pi} \left\{ -\frac{c_s^2 \pi}{r_0^2} t + \frac{2c_s^2}{r_0^2} t \arcsin\left(\frac{x_i}{c_s t}\right) \right. \\
&\quad \left. + \frac{2x_0}{r_0^2} \frac{1}{\sqrt{c_s^2 t^2 - x_i^2}} \left( x_i \frac{\partial x_i}{\partial t} - \frac{x_i^2}{t} + c_s^2 t - x_i \frac{\partial x_i}{\partial t} \right) \right\} \tag{A.14} \\
&= \frac{\Gamma}{2\pi} \left\{ -\frac{c_s^2 \pi}{r_0^2} t + \frac{2c_s^2}{r_0^2} t \arcsin\left(\frac{x_i}{c_s t}\right) + \frac{2x_0}{r_0^2} \frac{1}{\sqrt{c_s^2 t^2 - x_i^2}} \left( \frac{c_s^2 t^2 - x_i^2}{t} \right) \right\}.
\end{aligned}$$

Now, inserting A.5 for  $x_i$  gives

$$\begin{aligned}
p\left(\begin{pmatrix} 0 \\ 0 \end{pmatrix}, t\right) &= \frac{\Gamma}{2\pi} \left\{ -\frac{c_s^2 \pi}{r_0^2} t + \frac{2c_s^2}{r_0^2} t \arcsin \left( \frac{x_0^2 + c_s^2 t^2 - r_0^2}{2x_0 c_s t} \right) \right. \\
&\quad \left. + \frac{2x_0}{r_0^2} \frac{1}{\sqrt{c_s^2 t^2 - \frac{(x_0^2 + c_s^2 t^2 - r_0^2)^2}{4x_0^2}}} \left( c_s^2 t - \frac{(x_0^2 + c_s^2 t^2 - r_0^2)^2}{4x_0^2 t} \right) \right\} \\
&= \frac{\Gamma}{2\pi} \left\{ -\frac{c_s^2 \pi}{r_0^2} t + \frac{2c_s^2}{r_0^2} t \arcsin \left( \frac{x_0^2 + c_s^2 t^2 - r_0^2}{2x_0 c_s t} \right) \right. \\
&\quad \left. + \frac{2x_0}{r_0^2} \sqrt{c_s^2 t^2 - \frac{(x_0^2 + c_s^2 t^2 - r_0^2)^2}{4x_0^2}} \right\}, \tag{A.15}
\end{aligned}$$

which can be finally simplified to the expression for the optoacoustic pressure emitted by a circular parabolic absorber upon delta-pulse excitation

$$\begin{aligned}
p\left(\begin{pmatrix} 0 \\ 0 \end{pmatrix}, t\right) &= \frac{\Gamma}{2\pi} \left\{ -\frac{c_s^2 \pi}{r_0^2} t + \frac{2c_s^2}{r_0^2} t \arcsin \left( \frac{x_0^2 + c_s^2 t^2 - r_0^2}{2x_0 c_s t} \right) \right. \\
&\quad \left. + \frac{2x_0 c_s}{r_0^2} \sqrt{1 - \frac{(x_0^2 + c_s^2 t^2 - r_0^2)^2}{4x_0^2 c_s^2 t^2}} \right\}. \tag{A.16}
\end{aligned}$$

The characteristic shape of the pressure signal can be seen in figure A.1 (c).

### A.1.2 Uniform Absorption

In this section the analytic expression for the pressure wave emitted by an uniformly absorbing circular absorber is calculated (figure A.1 (b)). Again, the excitation pulse is assumed to be a delta-function and the absorber is confined to the two dimensions of the xy-plane. Therefore 2.72 can be simplified to a line integral in two-dimensions,

$$p(\vec{r}, t) = \frac{\Gamma}{4\pi} \frac{\partial}{\partial t} \oint_{|\vec{r} - \vec{r}'| = c_s t} \frac{H_r(\vec{r}')}{|\vec{r} - \vec{r}'|} dl(\vec{r}'). \tag{A.17}$$

The absorption pattern considered now is defined as

$$H_r(x, y) = \begin{cases} 1, & (x - x_0)^2 + y^2 \leq r_0^2, \\ 0, & (x - x_0)^2 + y^2 > r_0^2, \end{cases} \tag{A.18}$$

with  $r_0$  being the radius of the absorbing circle. Once more, without loss of generality, the detector is assumed to be at the origin,  $\vec{r} = (0, 0)^T$ , and the absorber is centered on the

x-axis at  $x_0$ . Then, by using the same parametrization A.7 as in the previous section one gets

$$p\left(\begin{pmatrix} 0 \\ 0 \end{pmatrix}, t\right) = \frac{\Gamma}{4\pi} \frac{\partial}{\partial t} 2 \int_{x_i}^{c_s t} \frac{1}{c_s t} \frac{c_s t}{\sqrt{c_s^2 t^2 - x^2}} dx \quad (\text{A.19})$$

$$\begin{aligned} &= \frac{\Gamma}{2\pi} \frac{\partial}{\partial t} \left[ \arcsin\left(\frac{x}{c_s t}\right) \right]_{x_i}^{c_s t} \\ &= \frac{\Gamma}{2\pi} \frac{\partial}{\partial t} \left( \frac{\pi}{2} - \arcsin\left(\frac{x_i}{c_s t}\right) \right) \\ &= -\frac{\Gamma}{2\pi} \frac{1}{\sqrt{1 - \left(\frac{x_i}{c_s t}\right)^2}} \frac{\frac{\partial x_i}{\partial t} c_s t - c_s x_i}{c_s^2 t^2} \\ &= -\frac{\Gamma}{2\pi} \frac{\frac{\partial x_i}{\partial t} - \frac{x_i}{t}}{\sqrt{c_s^2 t^2 - x_i^2}}. \end{aligned} \quad (\text{A.20})$$

Inserting A.5 into A.20 yields

$$p\left(\begin{pmatrix} 0 \\ 0 \end{pmatrix}, t\right) = -\frac{\Gamma}{2\pi} \frac{\frac{c_s^2 t}{x_0} - \frac{x_0^2 + c_s^2 t^2 - r_0^2}{2x_0 t}}{\sqrt{c_s^2 t^2 - \left(\frac{x_0^2 + c_s^2 t^2 - r_0^2}{2x_0}\right)^2}}, \quad (\text{A.21})$$

which can be finally simplified to

$$p\left(\begin{pmatrix} 0 \\ 0 \end{pmatrix}, t\right) = \frac{\Gamma}{2\pi} \frac{x_0^2 - c_s^2 t^2 - r_0^2}{2x_0 t \sqrt{c_s^2 t^2 - \frac{(x_0^2 + c_s^2 t^2 - r_0^2)^2}{4x_0^2}}}, \quad (\text{A.22})$$

the expression for the pressure wave emitted by a uniformly absorbing circular area and can be seen in figure A.1 (d).

## A.2 Analytical Pressure Formulas in 3D

### A.2.1 Parabolic Absorption

In this part, the analytical pressure wave emitted by a spherical absorber with parabolic absorption in three dimensions is calculated. In three dimensions, one has to solve the surface integral defined by equation 2.72

$$p(\vec{r}, t) = \frac{\Gamma}{4\pi} \frac{\partial}{\partial t} \iiint_{|\vec{r} - \vec{r}'| = c_s t} \frac{H_r(\vec{r}')}{|\vec{r} - \vec{r}'|} d\vec{r}' \quad (\text{A.23})$$

$$= \frac{\Gamma}{4\pi} \frac{\partial}{\partial t} \oint_{|\vec{r} - \vec{r}'| = c_s t} \frac{H_r(\vec{r}')}{|\vec{r} - \vec{r}'|} dS(\vec{r}'). \quad (\text{A.24})$$

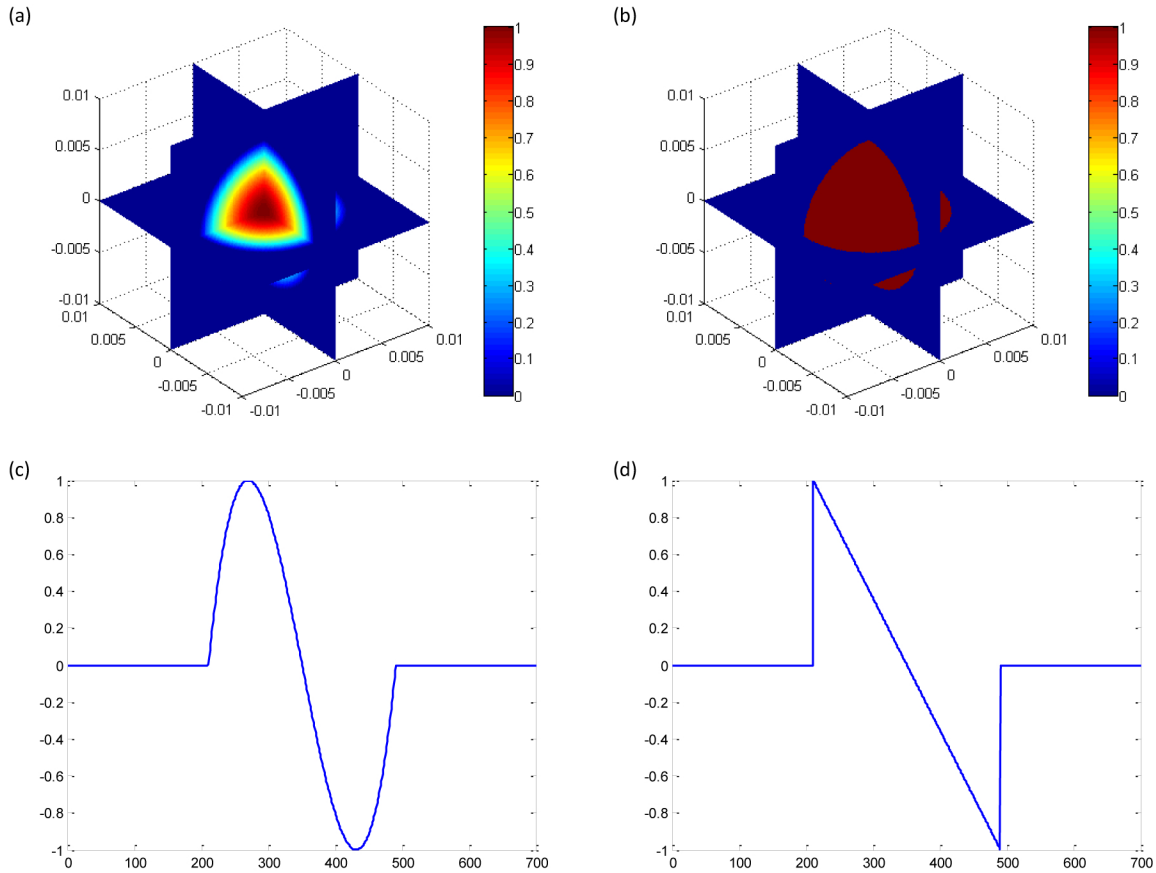


Figure A.2: (a) Volumetric, parabolic absorption pattern. (b) Uniformly absorbing sphere. (c) Analytical signal emitted by a truncated three-dimensional paraboloid. (d) Analytical signal emitted by a uniformly absorbing sphere.

with  $\vec{r} = (x, y, z)^T$ . Here, the integral to be solved is a surface integral over the sphere with radius  $c_s t$  centered at  $\vec{r}$ . The surface element is denoted by  $dS(\vec{r})$ . For simplicity, the detector position is assumed to be the origin,  $\vec{r} = (0, 0, 0)^T$ . Furthermore, without loss of generality it is assumed that the spherical absorber is centered on the x-axis at position  $x_0$ . The spherical absorption pattern is then given by

$$H_r(x, y, z) = \begin{cases} 1 - \frac{(x-x_0)^2 + y^2 + z^2}{r_0^2}, & (x-x_0)^2 + y^2 + z^2 \leq r_0^2, \\ 0, & (x-x_0)^2 + y^2 + z^2 > r_0^2, \end{cases} \quad (\text{A.25})$$

and can be seen in figure A.2 (a). Therefore, equation A.24 simplifies to

$$p\left(\begin{pmatrix} 0 \\ 0 \\ 0 \end{pmatrix}, t\right) = \frac{\Gamma}{4\pi} \frac{\partial}{\partial t} \left\{ \oint_{|\vec{r}'|=c_s t} \frac{H_r(\vec{r}')}{c_s t} dS(\vec{r}') \right\}. \quad (\text{A.26})$$

$x_i$  and  $y_i$  define the coordinates in the xy-plane where the detection surface with radius  $c_s t$  intersects the spherical absorber with radius  $r_0$ . They can be calculated as

$$x_i = \frac{x_0^2 + c_s^2 t^2 - r_0^2}{2x_0}, \quad (\text{A.27})$$

$$y_i = \sqrt{c_s^2 t^2 - x_i^2} = \sqrt{c_s^2 t^2 - \frac{(x_0^2 + c_s^2 t^2 - r_0^2)^2}{4x_0^2}}. \quad (\text{A.28})$$

Then, the surface over which the integral is calculated can be parametrized by

$$\Psi : \begin{cases} [0, y_i] \times [0, 2\pi[ & \longrightarrow & \mathbb{R}^3, \\ (r, \phi) & \longmapsto & \begin{pmatrix} \sqrt{c_s^2 t^2 - r^2} \\ r \cos(\phi) \\ r \sin(\phi) \end{pmatrix}, \end{cases} \quad (\text{A.29})$$

which leads to the surface element

$$dS(\vec{r}') = \|\Psi_r \times \Psi_\phi\| dr d\phi = r \sqrt{1 + \frac{r^2}{c_s^2 t^2 - r^2}} dr d\phi. \quad (\text{A.30})$$

Inserting parametrization A.29 into equation A.26 and evaluating the integrals leads to

$$\begin{aligned} p \left( \begin{pmatrix} 0 \\ 0 \\ 0 \end{pmatrix}, t \right) &= \frac{\Gamma}{4\pi} \frac{\partial}{\partial t} \left\{ \oint_{|\vec{r}'|=c_s t} \frac{H_r(\vec{r}')}{c_s t} dS(\vec{r}') \right\} \\ &= \frac{\Gamma}{4\pi} \frac{\partial}{\partial t} \left\{ \int_0^{2\pi} \int_0^{y_i} \frac{1}{c_s t} \left( 1 - \frac{[\sqrt{c_s^2 t^2 - r^2} - x_0]^2 + [r \cos(\phi)]^2 + [r \sin(\phi)]^2}{r_0^2} \right) \right. \\ &\quad \left. r \sqrt{1 + \frac{r^2}{c_s^2 t^2 - r^2}} dr d\phi \right\} \\ &= \frac{\Gamma}{4\pi} \frac{\partial}{\partial t} \left\{ 2\pi \int_0^{y_i} \frac{1}{c_s t} \left( 1 - \frac{[\sqrt{c_s^2 t^2 - r^2} - x_0]^2 + r^2}{r_0^2} \right) r \sqrt{1 + \frac{r^2}{c_s^2 t^2 - r^2}} dr \right\} \\ &= \frac{\Gamma}{2} \frac{\partial}{\partial t} \left\{ \int_0^{y_i} \frac{1}{c_s t} \left( 1 - \frac{c_s^2 t^2 + x_0^2}{r_0^2} + \frac{2x_0 \sqrt{c_s^2 t^2 - r^2}}{r_0^2} \right) r \sqrt{1 + \frac{r^2}{c_s^2 t^2 - r^2}} dr \right\} \\ &= \frac{\Gamma}{2} \frac{\partial}{\partial t} \left\{ \int_0^{y_i} \frac{1}{c_s t} \left( 1 - \frac{c_s^2 t^2 + x_0^2}{r_0^2} \right) r \sqrt{1 + \frac{r^2}{c_s^2 t^2 - r^2}} dr \right. \\ &\quad \left. + \int_0^{y_i} \frac{1}{c_s t} \frac{2x_0}{r_0^2} \sqrt{c_s^2 t^2 - r^2} r \sqrt{1 + \frac{r^2}{c_s^2 t^2 - r^2}} dr \right\}. \end{aligned} \quad (\text{A.31})$$

By taking the anti-derivative [104], equation A.31 further simplifies to

$$p \left( \begin{pmatrix} 0 \\ 0 \\ 0 \end{pmatrix}, t \right) = \frac{\Gamma}{2} \frac{\partial}{\partial t} \left\{ \frac{1}{c_s t} \left( 1 - \frac{c_s^2 t^2 + x_0^2}{r_0^2} \right) \left[ (r^2 - c_s^2 t^2) \sqrt{\frac{c_s^2 t^2}{c_s^2 t^2 - r^2}} \right]_0^{y_i} \right. \quad (\text{A.32})$$

$$\left. + \frac{1}{c_s t} \frac{2x_0}{r_0^2} \left[ \frac{c_s t}{2} r^2 \right]_0^{y_i} \right\} \quad (\text{A.33})$$

$$= \frac{\Gamma}{2} \frac{\partial}{\partial t} \left\{ \frac{1}{c_s t} \left( 1 - \frac{c_s^2 t^2 + x_0^2}{r_0^2} \right) \left( (y_i^2 - c_s^2 t^2) \sqrt{\frac{c_s^2 t^2}{c_s^2 t^2 - y_i^2}} + c_s^2 t^2 \right) \right. \quad (\text{A.34})$$

$$\left. + \frac{x_0}{r_0^2} y_i^2 \right\} \quad (\text{A.35})$$

$$= \frac{\Gamma}{2} \frac{\partial}{\partial t} \left\{ \left( \frac{1}{c_s t} - \frac{c_s t}{r_0^2} - \frac{x_0^2}{c_s t r_0^2} \right) \left( c_s^2 t^2 - c_s t \sqrt{c_s^2 t^2 - y_i^2} \right) + \frac{x_0}{r_0^2} y_i^2 \right\}. \quad (\text{A.36})$$

Evaluating expression A.36 at  $y_i = \sqrt{c_s^2 t^2 - \frac{(x_0^2 + c_s^2 t^2 - r_0^2)^2}{4x_0^2}}$  gives

$$p \left( \begin{pmatrix} 0 \\ 0 \\ 0 \end{pmatrix}, t \right) = \frac{\Gamma}{2} \frac{\partial}{\partial t} \left\{ \left( \frac{1}{c_s t} - \frac{c_s t}{r_0^2} - \frac{x_0^2}{c_s t r_0^2} \right) \left( c_s^2 t^2 - c_s t \frac{x_0^2 + c_s^2 t^2 - r_0^2}{2x_0} \right) \right. \quad (\text{A.37})$$

$$\left. + \frac{x_0}{r_0^2} \left( c_s^2 t^2 - \frac{(x_0^2 + c_s^2 t^2 - r_0^2)^2}{4x_0^2} \right) \right\}.$$

Finally, derivation of A.37 with respect to t yields

$$p \left( \begin{pmatrix} 0 \\ 0 \\ 0 \end{pmatrix}, t \right) = \frac{\Gamma}{2} \left[ c_s - \frac{c_s x_0^2}{r_0^2} + \left( \frac{3c_s^2 x_0}{r_0^2} - \frac{c_s^2}{x_0} \right) t + \frac{3c_s^2}{r_0^2} t^2 - \frac{c_s^4}{x_0 r_0^2} t^3 \right]. \quad (\text{A.38})$$

The characteristic shape of the signal can be seen in figure A.2 (c).

### A.2.2 Uniform Absorption

In the following, the analytical expression for an optoacoustic pressure wave emitted by a spherical uniform absorber (figure A.2 (b)) upon delta-pulse excitation is calculated. Thereby, equation A.26 is solved for the absorption pattern

$$H_r(x, y, z) = \begin{cases} 1, & (x - x_0)^2 + y^2 + z^2 \leq r_0^2, \\ 0, & (x - x_0)^2 + y^2 + z^2 > r_0^2. \end{cases} \quad (\text{A.39})$$

Function A.39 defines a homogeneously absorbing sphere with radius  $r_0$  and center on the x-axis at  $x_0$ . Analog to section A.2.1, inserting surface parametrization A.29 into equation

A.26 yields

$$p \left( \begin{pmatrix} 0 \\ 0 \\ 0 \end{pmatrix}, t \right) = \frac{\Gamma}{4\pi} \frac{\partial}{\partial t} \left\{ \oint_{|\vec{r}'|=c_s t} \frac{H_r(\vec{r}')}{c_s t} dS(\vec{r}') \right\} \quad (\text{A.40})$$

$$= \frac{\Gamma}{4\pi} \frac{\partial}{\partial t} \left\{ \int_0^{2\pi} \int_0^{y_i} \frac{r}{c_s t} \sqrt{1 + \frac{r^2}{c_s^2 t^2 - r^2}} dr d\phi \right\} \quad (\text{A.41})$$

$$= \frac{\Gamma}{4\pi} \frac{\partial}{\partial t} \left\{ \frac{2\pi}{c_s t} \left[ \sqrt{\frac{c_s^2 t^2}{c_s^2 t^2 - r^2}} (r^2 - c_s^2 t^2) \right]_0^{y_i} \right\} \quad (\text{A.42})$$

$$= \frac{\Gamma}{2} \frac{\partial}{\partial t} \left\{ \frac{1}{c_s t} \left( \sqrt{\frac{c_s^2 t^2}{c_s^2 t^2 - y_i^2}} (y_i^2 - c_s^2 t^2) + c_s^2 t^2 \right) \right\} \quad (\text{A.43})$$

$$= \frac{\Gamma}{2} \frac{\partial}{\partial t} \left\{ \frac{1}{c_s t} \left( -c_s t \sqrt{c_s^2 t^2 - y_i^2} + c_s^2 t^2 \right) \right\}. \quad (\text{A.44})$$

Considering A.28 one can substitute the square root in expression A.44 by  $x_i$ , resulting in

$$\begin{aligned} p \left( \begin{pmatrix} 0 \\ 0 \\ 0 \end{pmatrix}, t \right) &= \frac{\Gamma}{2} \frac{\partial}{\partial t} \left\{ \frac{1}{c_s t} (-c_s t x_i + c_s^2 t^2) \right\} \\ &= \frac{\Gamma}{2} \frac{\partial}{\partial t} \left\{ -\frac{x_0^2 + c_s^2 t^2 - r_0^2}{2x_0} + c_s t \right\} \\ &= \frac{\Gamma}{2} c_s \left( 1 - \frac{c_s}{x_0} t \right). \end{aligned} \quad (\text{A.45})$$

Equation A.45 gives an expression for the pressure emitted from a uniform spherical absorber upon delta-pulse excitation (figure A.2 (d)).

# Bibliography

- [1] Philipp Bozzini. Lichtleiter, eine Erfindung zur Anschauung innerer Theile und Krankheiten nebst der Abbildung. *Journal der practischen Heilkunde*, 24:107–124, 1806.
- [2] Wilhem Conrad Röntgen. Über eine neue Art von Strahlen. *Sitzungsberichte der Physikalisch-Medizinischen Gesellschaft zu Würzburg*, pages 132–140, 1895.
- [3] Thomas L. Szabo. *Diagnostic Ultrasound Imaging: Inside Out*. Elsevier Academic Press, Boston, Massachusetts, 2004.
- [4] Allan Cormack. 75 years of Radon Transform. *Journal of Computer Assisted Tomography*, 16:673, 1992.
- [5] E.C. Beckmann. CT scanning the early days. *The British Journal of Radiology*, 79:5–8, 2005.
- [6] Johann Radon. Über die bestimmung von Funktionen durch ihre Integralwerte längs gewisser Mannigfaltigkeiten. *Berichte über die Verhandlungen der Königlich-Sächsischen Gesellschaft der Wissenschaften zu Leipzig*, 69:262–277, 1917.
- [7] Paul C. Lauterbur. Image Formation by Induced Local Interactions: Examples Employing Nuclear Magnetic Resonance. *Nature*, 242:190 – 191, 1973.
- [8] Peter Mansfield and Peter K. Grannell. NMR 'diffraction' in solids? *Journal of Physics C: Solid State Physics*, 6:L422 – L426, 1973.
- [9] Scott A. Huettel, Allen W. Song, and Gregory McCarthy. *Functional Magnetic Resonance Imaging*. Sinauer Associates, Inc, Sunderland, Massachusetts, 2008.
- [10] Michel M. Ter-Pogossian, Michael E. Phelps, Edward J. Hoffman, and Nizar A. Mullani. A Positron-Emission Transaxial Tomograph for Nuclear Imaging (PETT). *Radiology*, 114:89 – 98, 1975.
- [11] William R. Hendee and E. Russell Ritenour. *Medical Imaging Physics*. Wiley-Liss, Inc, New York, New York, 2002.

- 
- [12] Ralph Weissleder and Umar Mahmood. Molecular Imaging . *Radiology*, 219:316 – 333, 2001.
- [13] Vasilis Ntziachristos. Fluorescence Molecular Imaging . *Annual Review of Biomedical Engineering*, 8:1 – 33, 2006.
- [14] Alexander Graham Bell. On the production and reproduction of sound by light. *The American Journal of Science*, 10:305–324, 1880.
- [15] Vasilis Ntziachristos. Going deeper than microscopy: the optical imaging frontier in biology. *Nature Methods*, 7:603 – 614, 2010.
- [16] Lihong V. Wang. *Photoacoustic Imaging and Spectroscopy*. CRC Press, Boca Raton, Florida, 2009.
- [17] Gerald J. Diebold, T. Sun, and M. I. Khan. Photoacoustic Monopole Radiation in One, Two, and Three Dimensions. *Physical Review Letters*, 67:3384 – 3387, 1991.
- [18] Lihong V. Wang and Hsin i Wu. *Biomedical Optics*. John Wiley & Sons, Hoboken, New Jersey, 2007.
- [19] Xosé-Luís Déan-Ben, Daniel Razansky, and Vasilis Ntziachristos. The effects of acoustic attenuation in optoacoustic signals. *Physics in Medicine and Biology*, 56:6129 – 6148, 2011.
- [20] Vasilis Ntziachristos and Daniel Razansky. Molecular Imaging by Means of Multi-spectral Optoacoustic Tomography (MSOT). *Chemical Reviews*, 110:2783 – 2794, 2010.
- [21] Adrian Taruttis, Stefan Morscher, Neal C. Burton, Daniel Razansky, and Vasilis Ntziachristos. Fast Multispectral Optoacoustic Tomography (MSOT) for Dynamic Imaging of Pharmacokinetics and Biodistribution in Multiple Organs. *PLOS ONE*, 7:30491, 2012.
- [22] Andreas Buehler, Eva Herzog, Daniel Razansky, and Vasilis Ntziachristos. Video rate optoacoustic tomography of mouse kidney perfusion. *Optics Letters*, 35:2475 – 2477, 2012.
- [23] Adrian Taruttis, Eva Herzog, Daniel Razansky, and Vasilis Ntziachristos. Real-time imaging of cardiovascular dynamics and circulating gold nanorods with multispectral optoacoustic tomography. *Optics Express*, 18:19592 – 19602, 2010.
- [24] Vasilis Ntziachristos, Jorge Ripoll, Lihong V. Wang, and Ralph Weissleder. Looking and listening to light: the evolution of whole-body photonic imaging. *Nature Biotechnology*, 23:313 – 320, 2005.

- [25] Xosé-Luís Déan-Ben and Daniel Razansky. Adding fifth dimension to optoacoustic imaging: volumetric time-resolved spectrally enriched tomography. *Light: Science & Applications*, 3:e137, 2014.
- [26] Robert A. Kruger, Pingyu Liu, Yuncai Richard Fang, and C. Robert Appledorn. Photoacoustic ultrasound (PAUS) – Reconstruction tomography. *Medical Physics*, 22:1605 – 1609, 1995.
- [27] Christoph G.A. Hoelen and Frits F. M. de Mul. Image reconstruction for photoacoustic scanning of tissue structures. *Applied Optics*, 39:5872 – 5883, 2000.
- [28] Minghua Xu and Lihong V. Wang. Universal back-projection algorithm for photoacoustic computed tomography. *Physical Review E*, 71:016706, 2005.
- [29] Yuan Xu, Dazi Feng, and Lihong V. Wang. Exact Frequency-Domain Reconstruction for Thermoacoustic Tomography – I: Planar Geometry. *IEEE Transactions on Medical Imaging*, 21:823 – 828, 2002.
- [30] Yuan Xu, Minghua Xu, and Lihong V. Wang. Exact Frequency-Domain Reconstruction for Thermoacoustic Tomography – II: Cylindrical Geometry. *IEEE Transactions on Medical Imaging*, 21:829 – 833, 2002.
- [31] Kornel P. Köstli, Martin Frenz, Hans Bebie, and Heinz P. Weber. Temporal backward projection of optoacoustic pressure transients using Fourier transform methods. *Physics in Medicine and Biology*, 46:1863 – 1872, 2001.
- [32] Leonid Kunyansky. Fast Reconstruction Algorithms for the Thermoacoustic Tomography in Certain Domains with Cylindrical or Spherical Symmetries. *Inverse Problems and Imaging*, 6:111 – 131, 2012.
- [33] Xosé-Luís Déan-Ben, Rui Ma, Amir Rosenthal, Vasilis Ntziachristos, and Daniel Razansky. Weighted model-based optoacoustic reconstruction in acoustic scattering media. *Physics in Medicine and Biology*, 58:5555 – 5566, 2013.
- [34] Dimple Modgil, Mark A. Anastasio, and Patrick J. La Rivière. Image reconstruction in photoacoustic tomography with variable speed of sound using a higher-order geometrical acoustics approximation. *Journal of Biomedical Optics*, 15:021308, 2010.
- [35] Shuhui Bu, Zhenbao Liu, Tsuyoshi Shiina, Kengo Kondo, Makoto Yamakawa, Kazuhiko Fukutani, Yasuhiro Someda, and Yasufumi Asao. Model-Based Reconstruction Integrated With Fluence Compensation for Photoacoustic Tomography. *IEEE Transactions on Medical Imaging*, 59:1354 – 1363, 2012.
- [36] Amir Rosenthal, Vasilis Ntziachristos, and Daniel Razansky. Model-based optoacoustic inversion with arbitrary-shape detectors. *Medical Physics*, 38:4285 – 4295, 2011.

- [37] Daniel Queirós, Xosé Luís Déan-Ben, Andreas Buehler, Daniel Razansky, Amir Rosenthal, and Vasilis Ntziachristos. Modeling the shape of cylindrically focused transducers in three-dimensional optoacoustic tomography. *Journal of Biomedical Optics*, 18:076014, 2013.
- [38] Minghua Xu and Lihong V. Wang. Analytic explanation of spatial resolution related to bandwidth and detector aperture size in thermoacoustic or photoacoustic reconstruction. *Physical Review E*, 67:056605, 2003.
- [39] Kun Wang, Sergey A. Ermilov, Richard Su, Hans-Peter Brecht, Alexander A. Oraevsky, and Mark A. Anastasio. An Imaging Model Incorporating Ultrasonic Transducer Properties for Three-Dimensional Optoacoustic Tomography. *IEEE Transactions on Medical Imaging*, 30:203 – 214, 2011.
- [40] Sheldon Axler, Paul Bourdon, and Wade Ramey. *Harmonic Function Theory*. Springer-Verlag, New York, New York, 2001.
- [41] Philip McCord Morse and Karl Uno Ingard. *Theoretical Acoustics*. McGraw-Hill, New York, New York, 1968.
- [42] Lawrence C. Evans. *Partial Differential Equations*. American Mathematical Society, Providence, Rhode Island, 2010.
- [43] Kazumi Watanabe. *Greens Functions for Laplace and Wave Equations*, volume 71. Springer International Publishing, 2014.
- [44] Arthur Erdlyi. *Tables of Integral Transforms*. McGraw-Hill, New York, New York, 1954.
- [45] Sergey A. Telenkov and Andreas Mandelis. Fourier-domain biophotoacoustic subsurface depth selective amplitude and phase imaging of turbid phantoms and biological tissue. *Journal of Biomedical Optics*, 11:044006, 2006.
- [46] Sergey A. Telenkov and Andreas Mandelis. Fourier-domain methodology for depth-selective photothermoacoustic imaging of tissue chromophores. *The European Physical Journal Special Topics*, 153:443 – 448, 2008.
- [47] Stephan Kellnberger, Nikolaos C. Deliolanis, Daniel Queirós, George Sergiadis, and Vasilis Ntziachristos. *In vivo* frequency domain optoacoustic tomography. *Optics Letters*, 37:3423 – 3425, 2012.
- [48] Dean G. Duffy. *Green's Functions with Applications*. Chapman & Hall/CRC, Boca Raton, Florida, 2001.
- [49] Sergey Telenkov, Andreas Mandelis, Bahman Lashkari, and Michael Forcht. Frequency-domain photothermoacoustics: Alternative imaging modality of biological tissues. *Journal of Applied Physics*, 105:102029, 2009.

- [50] Jonathan W. Valvano, Joe R. Cochran, and Kenneth R. Diller. Thermal Conductivity and Diffusivity of Biomaterials Measured with Self-Heated Thermistors. *International Journal of Thermophysics*, 6:301 – 311, 1984.
- [51] Ralph Weissleder and Vasilis Ntziachristos. Shedding light onto live molecular targets. *Nature Medicine*, 9:123 – 128, 2003.
- [52] Daniel Razansky, Andreas Buehler, and Vasilis Ntziachristos. Volumetric real-time multispectral optoacoustic tomography of biomarkers. *Nature Protocols*, 6:1121 – 1129, 2011.
- [53] American National Standards Institute. American National Standard for Safe Use of Lasers, 2007.
- [54] Jacques Curie and Pierre Curie. Développement par compression de l'électricité polaire dans les cristaux hémihédres à faces inclinées. *Bulletin de la Société minérologique de France*, 3:90 – 93, 1880.
- [55] Xuedin Wang, Brian Fowlkes, Jonathan Cannata, Changhong Hu, and Paul Carson. Photoacoustic Imaging with a Commercial Ultrasound System and a Custom Probe. *Ultrasound in Medicine and Biology*, 37:484 – 492, 2011.
- [56] Edward Zhang, Jan Laufer, and Paul Beard. Backward-mode multiwavelength photoacoustic scanner using a planar FabryPerot polymer film ultrasound sensor for high-resolution three-dimensional imaging of biological tissues. *Applied Optics*, 47:561 – 577, 2008.
- [57] Amir Rosenthal, Daniel Razansky, and Vasilis Ntziachristos. High-sensitivity compact ultrasonic detector based on a pi-phase-shifted fiber Bragg grating. *Optics Letters*, 36:1833 – 1835, 2011.
- [58] Tatyana Dmitrievna Khokhlova, Ivan Mikhailovich Pelivanov, and Aleksander Alekseevich Karabutov. Optoacoustic tomography utilizing focused transducers: The resolution study. *Applied Physics Letters*, 92:024105, 2008.
- [59] H.T. O'Neil. Theory of Focusing Radiators. *The Journal of the Acoustical Society of America*, 21:516 – 526, 1949.
- [60] John W. Hunt, Marcel Arditi, and F. Stuart Foster. Ultrasound Transducers for Pulse-Echo Medical Imaging. *IEEE Transactions on Biomedical Engineering*, 30:453 – 481, 1983.
- [61] Jørgen Arendt Jensen and Niels Bruun Svendsen. Calculation of Pressure Fields from Arbitrarily Shaped, Apodized, and Excited Ultrasound Transducers. *IEEE Transactions on Ultrasonics, Ferroelectrics and Frequency Control*, 39:262 – 267, 1992.

- [62] Drake A. Guenther and William F. Walker. A Method for Accurate *in silico* modeling of Ultrasound Transducer Arrays. *Ultrasonics*, 49:404 – 412, 2009.
- [63] Marcel Arditi, F. Stuart Foster, and John W. Hunt. Transient Fields of Concave Annular Arrays. *Ultrasonic Imaging*, 3:37 – 61, 1981.
- [64] Meng-Lin Li, Hao F. Zhang, and Konstantin Maslov. Improved *in vivo* photoacoustic microscopy based on a virtual-detector concept. *Optics Letters*, 31:474 – 476, 2006.
- [65] Amir Rosenthal, Vasilis Ntziachristos, and Daniel Razansky. Optoacoustic Methods for Frequency Calibration of Ultrasonic Sensors. *IEEE Transactions on Ultrasonics, Ferroelectrics and Frequency Control*, 58:316 – 326, 2011.
- [66] Gerhard Ludwig and Klaus Brendel. Calibration of Hydrophones Based on Reciprocity and Time Delay Spectrometry. *IEEE Transactions on Ultrasonics, Ferroelectrics and Frequency Control*, 35:168 – 174, 1988.
- [67] Robert A. Smith and David R. Bacon. A multiple-frequency hydrophone calibration technique. *The Journal of the Acoustical Society of America*, 87:2231 – 2243, 1990.
- [68] Miguel Ángel Araque Caballero, Amir Rosenthal, Andreas Buehler, Daniel Razansky, and Vasilis Ntziachristos. Optoacoustic Determination of Spatio-Temporal Responses of Ultrasound Sensors. *IEEE Transactions on Ultrasonics, Ferroelectrics and Frequency Control*, 60:1234 – 1244, 2013.
- [69] David Bæk and Jørgen Arendt Jensen. Modeling transducer impulse responses for predicting calibrated pressure pulses with the ultrasound simulation program Field II. *The Journal of the Acoustical Society of America*, 127:2825 – 2835, 2010.
- [70] Rui Ma, Sebastian Söntges, Shy Shoham, Vasilis Ntziachristos, and Daniel Razansky. Fast scanning coaxial optoacoustic microscopy. *Biomedical Optics Express*, 3:1724 – 1731, 2012.
- [71] Hao Zhang, Konstantin Maslov, George Stoica, and Lihong V. Wang. Functional photoacoustic microscopy for high-resolution and noninvasive *in vivo* imaging. *Nature Biotechnology*, 24:848 – 851, 2006.
- [72] Krista Jansen, Antonius F.W. van der Steen, Heleen M.M. van Beusekom, J. Wolter Oosterhuis, and Gijs van Soest. Intravascular photoacoustic imaging of human coronary atherosclerosis. *Optics Letters*, 36:597 – 599, 2011.
- [73] Doug Yeager, Andrei Karpiouk, Bo Wang, James Amirian, Konstantin Sokolov, Richard Smalling, and Stanislav Emelianov. Intravascular photoacoustic imaging of exogenously labeled atherosclerotic plaque through luminal blood. *Journal of Biomedical Optics*, 17:106016, 2012.

- [74] Chulhong Kim, Todd N. Erpelding, Ladislav Jankovic, Michael D. Pashley, and Lihong V. Wang. Deeply penetrating in vivo photoacoustic imaging using a clinical ultrasound array system. *Biomedical Optics Express*, 1:278 – 284, 2010.
- [75] Jun Xia, Muhammad R. Chatni, Konstantin Maslov, Zijian Guo, Kun Wang, Mark Anastasio, and Lihong V. Wang. Whole-body ring-shaped confocal photoacoustic computed tomography of small animals *in vivo*. *Journal of Biomedical Optics*, 17:050506, 2012.
- [76] John Gamelin, Anastasios Maurudis, Andres Aguirre, Fei Huang, Puyun Guo, Lihong V. Wang, and Quing Zhu. A real-time photoacoustic tomography system for small animals. *Optics Express*, 17:10489 – 10498, 2009.
- [77] Hans-Peter Brecht, Richard Su, Fronheiser Matthew, Sergey A. Ermilov, Andre Conjusteau, and Alexander A. Oraevsky. Whole-body three-dimensional optoacoustic tomography system for small animals. *Journal of Biomedical Optics*, 14:064007, 2009.
- [78] Xosé-Luís Déan-Ben, Ali Ozbek, and Daniel Razansky. Volumetric Real-Time Tracking of Peripheral Human Vasculature With GPU-Accelerated Three-Dimensional Optoacoustic Tomography. *IEEE Transactions on Medical Imaging*, 32:2050 – 2055, 2013.
- [79] Andreas Buehler, Xosé-Luís Déan-Ben, Jing Claussen, Vasilis Ntziachristos, and Daniel Razansky. Three-dimensional optoacoustic tomography at video rate. *Optics Express*, 20:22712 – 22719, 2012.
- [80] Liangzhong Xiang, Bo Wang, Lijun Ji, and Huabei Jiang. 4-D Photoacoustic Tomography. *Nature Scientific Reports*, 3:1113, 2013.
- [81] Amir Rosenthal, Vasilis Ntziachristos, and Daniel Razansky. Acoustic Inversion in Optoacoustic Tomography: A Review. *Current Medical Imaging Reviews*, 9:318–336, 2013.
- [82] Dragoslav S. Mitrinović and Jovan D. Kečkić. *The Cauchy Method of Residues: Theory and Applications*. Kluwer Academic Publishers Group, Alphen aan den Rijn, Netherlands, 1984.
- [83] Bradley E. Treeby and Ben T. Cox. k-Wave: MATLAB toolbox for the simulation and reconstruction of photoacoustic wave fields. *Journal of Biomedical Optics*, 15:021314, 2010.
- [84] Michael Jaeger, Simon Schüpbach, Andreas Gertsch, Michael Kitz, and Martin Frenz. Fourier reconstruction in optoacoustic imaging using truncated regularized inverse k-space interpolation. *Inverse Problems*, 23:S51 – S63, 2007.

- 
- [85] Amir Rosenthal, Daniel Razansky, and Vasilis Ntziachristos. Fast Semi-Analytical Model-Based Acoustic Inversion for Quantitative Optoacoustic Tomography. *IEEE Transactions on Medical Imaging*, 29:1275 – 1285, 2010.
- [86] Xosé-Luís Déan-Ben, Andreas Buehler, Vasilis Ntziachristos, and Daniel Razansky. Accurate model-based reconstruction algorithm for three-dimensional optoacoustic tomography. *IEEE Transactions on Medical Imaging*, 31:1922 – 1928, 2012.
- [87] Günther Paltauf, John A. Viator, Scott A. Prahl, and Steven L. Jacques. Iterative reconstruction algorithm for optoacoustic imaging. *The Journal of the Acoustical Society of America*, 112:1536 – 1544, 2002.
- [88] Andrei Nikolaevich Tikhonov and Vasilii IAKovlevich Arsenin. *Solutions of ill-posed problems*. John Wiley & Sons Inc, Hoboken, New Jersey, 1977.
- [89] Christopher C. Paige and Michael A. Saunders. LSQR: An Algorithm for Sparse Linear Equations and Sparse Least Squares. *ACM Transaction on Mathematical Software*, 8:43 – 71, 1982.
- [90] Mark A. Anastasio, Jin Zhang, Xiaochuan Pan, Yu Zou, Geng Ku, and Lihong V. Wang. Half-Time Image Reconstruction in Thermoacoustic Tomography. *IEEE Transactions on Medical Imaging*, 24:1536 – 1544, 2005.
- [91] Jithin Jose, Rene G. H. Willeminck, Wiendelt Steenbergen, Kees Slump, Ton G. van Leeuwen, and Srirang Manohar. Speed-of-sound compensated photoacoustic tomography for accurate imaging. *Medical Physics*, 39:7262 – 7271, 2012.
- [92] Chao Huang, Liming Nie, Lihong V. Wang, and Mark A. Anastasio. Full-Wave Iterative Image Reconstruction in Photoacoustic Tomography With Acoustically Inhomogeneous Media. *IEEE Transactions on Medical Imaging*, 32:1097 – 1110, 2013.
- [93] Jin Zhang, Mark A. Anastasio, Patrick J. La Rivière, and Lihong V. Wang. Effects of Different Imaging Models on Least-Squares Image Reconstruction Accuracy in Photoacoustic Tomography. *IEEE Transactions on Medical Imaging*, 28:1781 – 1790, 2009.
- [94] Pinhas Ephrat, Lynn Keenliside, Adam Seabrook, Frank S. Prato, and Jeffrey J. L. Carson. Three-dimensional photoacoustic imaging by sparse-array detection and iterative image reconstruction. *Journal of Biomedical Optics*, 13:054052, 2008.
- [95] Kun Wang, Robert W. Schoonover, Richard Su, Alexander Oraevsky, and Mark A. Anastasio. Discrete Imaging Models for Three-Dimensional Optoacoustic Tomography Using Radially Symmetric Expansion Functions. *IEEE Transactions on Medical Imaging*, 33:1180 – 1193, 2014.

- 
- [96] Qiaofeng Xu, Emil Y. Sidky, Xiaochuan Pan, Marco Stampanoni, Peter Modregger, and Mark A. Anastasio. Investigation of discrete imaging models and iterative image reconstruction in differential X-ray phase-contrast tomography. *Optics Express*, 20:10724 – 10749, 2012.
- [97] Merrill Skolnik. *Radar Handbook*. McGraw-Hill, New York, New York, 2008.
- [98] Achim Hein. *Verarbeitung von SAR-Daten unter besonderer Berücksichtigung interferometrischer Anwendungen*. PhD thesis, Universität-Gesamthochschule Siegen, 1998.
- [99] M. L. J. Landsman, G. Kwant, G. A. Mook, and W.G. Zijlstra. Light-absorbing properties, stability, and spectral stabilization of indocyanine green. *Optics Letters*, 40:575 – 583, 1976.
- [100] Daniel Razansky, Daniel Vinegoni, and Vasilis Ntziachristos. Multispectral photoacoustic imaging of fluorochromes in small animals. *Optics Letters*, 32:2891 – 2893, 2007.
- [101] Amir Rosenthal, Thomas Jetzfellner, Daniel Razansky, and Vasilis Ntziachristos. Efficient Framework for Model-Based Tomographic Image Reconstruction Using Wavelet Packets. *IEEE Transactions on Medical Imaging*, 31:1346 – 1357, 2012.
- [102] Stéphane Mallat. *A Wavelet Tour of Signal Processing, Third Edition: The Sparse Way*. Elsevier Academic Press, Burlington, Massachusetts, 3rd edition, 2008.
- [103] Michael Weeks. *Digital Signal Processing Using MATLAB<sup>®</sup> and Wavelets*. Infinity Science Press LLC, Hingham, Massachusetts, 2007.
- [104] Ilja N. Bronstein, Konstantin A. Semendjajew, Gerhard Musiol, and Heiner. Mühlig. *Taschenbuch der Mathematik*. Harri Deutsch, Frankfurt, 2001.



# Publication List

## Publications in Peer-Reviewed Journals

**Daniel Queirós**, Xosé Luís Déan-Ben, Andreas Buehler, Daniel Razansky, Amir Rosenthal, and Vasilis Ntziachristos

*Modeling the shape of cylindrically focused transducers in three-dimensional optoacoustic tomography*

Journal of Biomedical Optics; 18(7); 076014 (2013)

doi:10.1117/1.JBO.18.7.076014

Stephan Kellnberger, Nikolaos C. Deliolanis, **Daniel Queirós**, George Sergiadis, and Vasilis Ntziachristos

*In vivo frequency domain optoacoustic tomography*

Optics Letters; 37(16); 3423 - 3425 (2012)

doi:10.1364/OL.37.003423

## Conference Proceedings

**Daniel Queirós**, Xosé Luís Déan-Ben, Andreas Buehler, Daniel Razansky, Amir Rosenthal, and Vasilis Ntziachristos

*Incorporating geometric detector properties into three-dimensional optoacoustic tomography*

European Conference on Biomedical Optics (ECBO), 2013

**Daniel Queirós**, Xosé Luís Déan-Ben, Andreas Buehler, Daniel Razansky, Amir Rosenthal, and Vasilis Ntziachristos

*Modeling the shape of cylindrically focused transducers in three-dimensional optoacoustic tomography*

SPIE Photonics West, 2014

## Manuscripts Under Review

Nicolas Bézière, Neus Lozano, Antonio Nunes, Juan Salichs, **Daniel Queirós**, Kostas Kostarelos, and Vasilis Ntziachristos

*Rethinking Optoacoustic Contrast: PEGylated Liposomal ICG within the Tumor Micro-environment.*

Biomaterials

Juan Salichs, Vladimir Ermolayev, Antonio Nunes, **Daniel Queirós**, Neus Lozano, Kostas Kostarelos, and Vasilis Ntziachristos

*High Resolution Imaging of Heterogeneous Solid Tumors with Novel Rotational Mesoscopy Multispectral Optoacoustic Tomography System.*